

**Controllable and Scalable Thermal Sublimation Thinning  
of Black Phosphorus**

by

Weijun Luo

B. Sc, Fudan University, Shanghai, China, 2013

A THESIS SUBMITTED IN PARTIAL FULFILLMENT  
OF THE REQUIREMENTS FOR THE DEGREE OF

**MASTER OF APPLIED SCIENCE**

in

THE FACULTY OF GRADUATE AND POSTDOCTORAL  
STUDIES

(Materials Engineering)

The University of British Columbia

(Vancouver)

April 2017

© Weijun Luo, 2017

# Abstract

Two-dimensional lamellar black phosphorus (BP) has emerged as a promising semiconductor for next generation integrated circuits (IC) and photonics, especially in flexible and ultra-thin electronic and photonic devices. With layer numbers of  $>20$  to 1, the electronic energy band gap of BP covers the range from 0.3 (bulk) to 2 eV (single-layer), which can fill the gap between graphene and transition metal di-chalcogenides (TMDCS). It is necessary to prepare uniform, large scale and crystalline few-layer BP for industry applications.

We investigated thinning rates of BP at different temperatures so that the users can control the time of heating and have the ability to monitor the thickness of BP during heating processes. Identification of crystallographic orientation (CO) of BP by Raman Spectroscopy is applied, which enables the Raman intensity ratios between BP and substrates to be only thickness-dependent. This ratio can be used as a non-contact optical method to determine the actual thickness of BP during preparation, which is crucial to determine the end point of the thinning process.

In this thesis work, we first reported the layer-by-layer sublimation of BP below 600 K, which was observed by optical color changes; secondly, we investigated the thinning rates of BP at 500 K and 550 K to be  $\sim 0.2$  nm / min 500 K and  $\sim 1.5$  nm / min at 550 K; thirdly, we investigated the effective determination of CO of BP and underlying Si by polarized Raman Spectroscopy with excitation wavelength of 441.6 nm; fourthly, we investigated the thickness-dependent Raman peak intensity ratio  $\frac{Si}{A_g^2}$  at a fixed CO, which can be used as an indicator of the thickness of BP; lastly, we presented the successful and repeatable preparation of large crystalline 2

to 4 -layer BP.

This work is the first study available to use the sublimation thinning as a controllable method to prepare large, uniform and crystalline BP down to 2-4 atomic layers. This work is the first study available on developing an all-Raman method in identifying the CO of BP, determining the in-situ and ex-situ thickness and confirming the crystallinity and uniformity of prepared BP.

# Preface

All of the work was done in the Department of Materials Engineering at UBC during the past two years, including the designs of experiments such as in-situ Raman Spectroscopy, Raman imaging and Angle-resolved Polarized Raman spectroscopy (ARPRS). The Atomic Force Microscopy was performed in 4D LABS, Simon Fraser University, Burnaby, B.C., Canada.

The author prepared most of the original BP samples and developed sublimation method in preparing BP with different thickness; Mr. Jialun Liu and Prof. Wenjuan Zhu from the University of Illinois at Urbana-Champaign (U.S.A.) provided the sample used in Figure 2.3 and 2.4. The author conceived and conducted most of the Raman and AFM measurements, and did all the data analyses in this work; Mr. Rui Yang from Prof. Joshua Folk's group at the University of British Columbia (Canada) helped with the AFM measurements illustrated in Figure 2.4.

Mr. David Tuschel from Horiba Scientific in NJ, U.S.A inspired the author both in comprehension of Raman theory and experiment design.

One conference presentation was made at Material Research Society 2016 Fall meeting on this work in Chapter 2.

## **1. MRS 2016 Fall, NM2.2.08, Boston, M.A, U.S.A.**

Weijun Luo, Rui Yang, Jialun Liu, Wenjuan Zhu, Guangrui (Maggie) Xia. "Thermal Sublimation as a Scalable and Controllable Thinning Method for the Fabrication of Few-Layer Black Phosphorus."

In addition, one journal article has been submitted for review based on the work in Section 2; one journal article is in preparation for review based on the work in Chapter 3.

1. Luo, W., Yang, R., Liu, J., Zhu, W. and Xia, G., 2016. Thermal Sublimation: a Scalable and Controllable Thinning Method for the Fabrication of Few-Layer Black Phosphorus. arXiv preprint arXiv:1601.04103.

2. Luo, W., Song, Q., Zhou, G., Tuschel, D. and Xia, G., 2016. Study of Black Phosphorus Using Angle-Resolved Polarized Raman Spectroscopy with 442 nm Excitation. arXiv preprint arXiv:1610.03382.

# Table of Contents

<b>Abstract</b> . . . . .	<b>ii</b>
<b>Preface</b> . . . . .	<b>iv</b>
<b>Table of Contents</b> . . . . .	<b>vi</b>
<b>List of Tables</b> . . . . .	<b>ix</b>
<b>List of Figures</b> . . . . .	<b>x</b>
<b>Glossary</b> . . . . .	<b>xix</b>
<b>Acknowledgments</b> . . . . .	<b>xx</b>
<b>1 Introduction</b> . . . . .	<b>1</b>
1.1 Background And Motivations . . . . .	1
1.1.1 BP Structure: Layer-stacked 2D Semiconductor Material . . . . .	2
1.1.2 Layer-dependent Tunable Band Gap, High Carrier Mobility, Fast And High Photo-response . . . . .	4
1.1.3 Strong In-plane Anisotropies Of Black Phosphorus . . . . .	7
1.2 Current Challenges In BP Study . . . . .	13
1.2.1 Degradation Of BP In Air . . . . .	13
1.2.2 Fabrication Of Large-scale Few-layer Crystalline BP . . . . .	13
1.2.3 Debate On The CO Determination Of BP By ARPRS . . . . .	24
1.3 Basic Knowledge Of This Thesis Work . . . . .	28
1.3.1 Basic Knowledge of Raman Scattering . . . . .	28

1.3.2	Basic Knowledge Of Polarized Raman Spectroscopy . . .	30
1.3.3	Basic Knowledge Of Phonon Modes Of Black Phosphorus	34
1.3.4	Crystallographic Orientation Of Si (100) Wafer And Its Orientation Dependent Raman Response . . . . .	37
1.3.5	Thickness Determination By The N-dependent Raman In- tensity Ratio Of $\frac{I_{Si}}{I_{2DM}}$ . . . . .	38
1.3.6	Thermal Sublimation For Preparation Of Few-layer 2D Ma- terials . . . . .	39
1.3.7	Previous Studies On Thermal Decomposition And Subli- mation Of Black Phosphorus . . . . .	41
1.4	Problem Definition And Thesis Goal . . . . .	42
1.5	Scope Of The Thesis . . . . .	42
1.6	The Organization Of This Thesis . . . . .	43
<b>2</b>	<b>Thermal Sublimation of Black Phosphorus . . . . .</b>	<b>45</b>
2.1	General Procedure Of The Experimental Work Of This Chapter . .	45
2.1.1	Thermal Sublimation . . . . .	46
2.1.2	Raman Measurement . . . . .	46
2.1.3	Determination Of The Crystallographic Orientations (CO) Of BP And underlying Si (100) Substrate . . . . .	48
2.1.4	Atomic Force Microscopy (AFM) . . . . .	48
2.2	Results And Discussions . . . . .	49
2.2.1	Investigations Of Thermal Sublimation And Its Mechanism	49
2.2.2	Investigation of The Thinning Rates . . . . .	66
2.2.3	Preparation Of The few-layer BP . . . . .	81
2.2.4	Comparison Of BP Products With Previous Techniques . .	88
2.3	Conclusions . . . . .	88
<b>3</b>	<b>Determination of Crystallographic Orientations For BP Thickness Determination And Control By Raman Spectroscopy With 442 nm Excitation . . . . .</b>	<b>90</b>
3.1	Determination Of BP CO By ARPRS . . . . .	90
3.2	Experiment Methods . . . . .	91

3.2.1	Sample Preparation . . . . .	92
3.2.2	Angle-resolved Polarized Raman Spectroscopy (ARPRS) .	93
3.2.3	Atomic Force Microscopy (AFM) . . . . .	94
3.3	Results And Discussion . . . . .	94
3.3.1	ARPRS Study In The Determination Of Crystallographic Orientation (CO) Of BP . . . . .	94
3.3.2	Raman Peak Intensity Ratios: $\frac{I_{Si}}{I_{Ag}^2}$ As A Function Of BP Thickness . . . . .	120
3.3.3	Conclusion: . . . . .	129
<b>4</b>	<b>Conclusion and outlook . . . . .</b>	<b>130</b>
4.1	Conclusion . . . . .	130
4.2	Outlook . . . . .	131
	<b>Bibliography . . . . .</b>	<b>133</b>



# List of Tables

Table 1.1	Previous studies on liquid exfoliation of BP [1]. *aq.: deoxygenated water. . . . .	16
Table 1.2	The energy balance sheet for Raman process [2]. . . . .	28
Table 1.3	Raman intensity of BP $A_g$ and $B_{2g}$ modes under “parallel” configuration. . . . .	37
Table 3.1	Polar diagrams of peak intensity ratios of $A_g^1$ over $A_g^2$ of 11 BP samples on $SiO_2 / Si$ substrates acquired by Angle-resolved Polarized Raman Spectroscopy (ARPRS). . . . .	102
Table 3.2	Raman spectra: with maximum $A_g^1 / A_g^2$ Raman intensities. . .	106
Table 3.3	Polar diagrams of 16 BP samples on polyimide substrates acquired by Angle-resolved Polarized Raman Spectroscopy (ARPRS). 110	
Table 3.4	Raman spectra: with maximum $A_g^1 / A_g^2$ Raman intensities. . .	115
Table 3.5	Optical images, AFM thickness profiles of 11 BP Samples on $SiO_2/Si$ substrate. No.1-5 were samples prepared by sublimation thinning; No.6-12 were samples prepared by exfoliation. . .	117
Table 3.6	Optical images, AFM images and thickness profiles of 16 BP Samples on polyimide substrate. No.1-5, 8, 10 and 12 were samples prepared by sublimation thinning; No.6-7, 9, 11 and 13-16 were samples prepared by exfoliation. . . . .	120

# List of Figures

Figure 1.1	The atomistic ball-stick models of few-layer black phosphorus.	2
Figure 1.2	The first BP based transistor which was fabricated on a piece of 6.5-nm-thick mechanically exfoliated BP sample. Figure is reprinted from [3] with permission. . . . .	3
Figure 1.3	The band gap range of 2D and conventional bulk semiconductors. Figure is reprinted from [4] with permission. . . . .	5
Figure 1.4	(A): mobility and current on/off ratio of BP; (B): the photoresponsivity and response time of BP. Figure is reprinted from [4] with permission. . . . .	6
Figure 1.5	(A): Material parameters of single-layer BP; (B): the current characteristics of the n-type (solid) and p-type (dash) BP field-effect transistors at the x- (“zigzag”) and y-direction (“armchair”). $m_0$ is the free electron mass which has a value of $9.1 \times 10^{-31}$ kg. Figure is reprinted from [5] with permission. . .	8
Figure 1.6	(A): Light absorption of BP with different thickness (Figure is reprinted from [6] with permission) , here the “x” denotes for the “armchair” direction and the “y” denotes for the “zigzag” direction; (B): a black phosphorus vertical p-n junction (Figure is reprinted from [7] with permission); (C): the photoresponsivity of the BP p-n junction shown in (B), here $0^\circ$ represents the “armchair” direction and $90^\circ$ represents the “zigzag” direction. . . . .	10

Figure 1.7	The strain anisotropy of BP (Source: Ref [8]. Copyright 2016 American Chemical Society Reprinted with permission.). (A): Illustration of applying uniaxial tensile strain on the BP sample. (B): Uniaxial “AC” (“armchair”) and “ZZ” (“zigzag”) tensile strain-induced Raman shifts of the $A_g^1$ , $B_{2g}$ and $A_g^2$ modes. (C): Definitions of the P-P bond lengths of “R1”, “R2” and “R3”. (D): Strain-induced changes of the bond lengths. . . . .	12
Figure 1.8	Mechanical exfoliation of black phosphorus. (A): A 7.5-nm-thick BP sample based field-effect-transistors (Figure is reprinted from [3] with permission); (B): Raman spectra of single-layer and bilayer phosphorene and bulk black phosphorus films. (Figure is reprinted from [9] with permission). . . . .	14
Figure 1.9	(A): Illustration of liquid exfoliation method (Figure is reprinted from [10] with permission). (B): typical BP products prepared by liquid exfoliation method (Figure is reprinted from [11] with permission). . . . .	15
Figure 1.10	The few-layer BP prepared by plasma thinning. (Figure is reprinted from [12] with permission) . . . . .	17
Figure 1.11	The illustration of the layer-by-layer nano-patterning and thinning (by removing the oxidized byproduct through water rinsing) of BP. Figure is reprinted from [13] with permission. . .	18
Figure 1.12	The few-layer BP prepared by using chemical vapor deposition (CVD) method. (A): the morphology and thickness profile of the final product; (B): the comparison of the Raman spectra of the exfoliated BP, prepared amorphous BP and prepared crystalline BP. Figure is reprinted from [14] with permission. . .	19
Figure 1.13	The illustration of the few-layer BP prepared by using pulsed laser deposition (PLD) method. Figure is reprinted from [15] with permission . . . . .	21
Figure 1.14	(1) - (4) represent the Raman spectra of amorphous BP, red phosphorus, BP prepared by PLD (Pulsed Laser Deposition) deposition and exfoliated bulk BP. Figure is reprinted from [15] with permission. . . . .	23

Figure 1.15	The progress of ARPRS study using different excitation wavelengths in determining CO of BP: (1) [16]; (2) [17]; (3) [18]; (4) [19]; (5) this work. . . . .	25
Figure 1.16	ARPRS with different excitation wavelengths performed on a 20-nm-thick BP sample on SiO <sub>2</sub> / Si substrate. Figure is reprinted from [18] with permission. . . . .	26
Figure 1.17	ARPRS with different excitation wavelengths performed on BP samples with various thickness on SiO <sub>2</sub> / Si substrate. Figure is reprinted from [19] with permission. . . . .	27
Figure 1.18	The energy-level diagram showing the states involved in Raman spectra. Figure is reprinted from Wikipedia under the GNU Free Documentation License. . . . .	29
Figure 1.19	The energy-level diagram of the Stokes band of Raman scattering. Figure is reprinted from [2] with permission. . . . .	29
Figure 1.20	Figures (A) - (C) are reprinted from [20] with permission. (A): Illustration of the polarized Raman scattering light for the back scattering geometry. (B): Illustration of the polarization of the scattered light being “parallel” to that of the incident light. (C): Illustration of the polarization of the scattered light being “perpendicular” to that of the incident light. . . . .	31
Figure 1.21	Raman-active vibrational symmetries and Raman tensors for the crystal symmetry classes. Figure is reprinted from [21] with permission. . . . .	33
Figure 1.22	Illustration of the “ $\theta$ ” angle, the “zigzag” direction of the BP sample and the reading angle “ $\alpha$ ” of the rotation stage. The red arrows indicate the polarization of the incident laser. . . .	36
Figure 1.23	Illustration of Si (100) substrate. . . . .	37
Figure 1.24	The ARPRS results of the polarized Raman measurements of a Si (100) wafer measured under under the “parallel” and “cross” configuration. Image courtesy of David Tuschel, Horiba Scientific, USA. . . . .	38

Figure 1.25	(A): Sublimation thinning of a MoS <sub>2</sub> flake: mechanically exfoliated bilayer MoS <sub>2</sub> flake was thinned to single layer after annealed at 330 °C for 15 h. (Figure is reprinted from [22] with permission); (B) sublimation thinning of Bi <sub>2</sub> Se <sub>3</sub> : Bi <sub>2</sub> Se <sub>3</sub> plates prepared by deposition with an original thickness of 3.5 μm was heated at 510 ° for 10 minutes. (Figure is reprinted from [23] with permission); (C): sublimation thinning of WS <sub>2</sub> : mechanically exfoliated WS <sub>2</sub> flakes listed in the upper row were held at 600 ° for 45 minutes, and the Ar gas with a flow rate of 300 cc / min was purged in to protect the sample. At last, the figures in the lower row demonstrated that those flakes were thinned down to 8 to 45 nm from left to right. Figure is reprinted from [24] with permission. . . . .	40
Figure 1.26	(A): Observation of decomposition of BP at 400 °C by using transmission electron microscopy (TEM) (Figure is reprinted from [25] with permission); (B): the illustration of the decomposition mechanism of BP: detachments with phosphorus dimers (Figure is reprinted from [26] with permission). . . .	41
Figure 2.1	Illustration of the sublimation process of BP. . . . .	47
Figure 2.2	(A) - (D): Observation of the layer-layer-layer sublimation process of BP at 600 K. The different colors in the area 1 and area 2 indicated different thicknesses. . . . .	49
Figure 2.3	AFM and optical images of a trapezoid BP sample. (A) and (B): before heating; (C) and (D): after heating in nitrogen at 550 K for 195 mins. The dispersed white pits on the sample surface were attributed to the fast surface reactions with oxygen and moisture in the air [21] during sample transportation to the AFM and during the AFM measurements in the air. The red dashed lines indicated the edges of the samples and the numbers next to them are edge dimensions. . . . .	51

Figure 2.4	(A):the optical image of this BP flake before 500 K heating process, and the inset AFM line-scan profile indicated its thickness to be 36 nm; (B) - (C): Spatial Raman maps of $A_g^1$ and $A_g^2$ peak intensity acquired on a 36-nm-thick BP flake; (D): the optical image of this BP flake after 500 K heating process for 120 minutes, , and the inset AFM line-scan profile indicated its thickness to be 13 nm; (E) - (F): Raman images ( $A_g^1$ and $A_g^2$ modes) of this BP flake after 500 K heating process; . . . . .	52
Figure 2.5	(A): the optical image of this BP flake before 550 K heating process, and the inset AFM line-scan profile indicated its thickness to be 85 nm; (B) - (C): Spatial Raman maps of $A_g^1$ and $A_g^2$ peak intensity acquired on an 85-nm-thick BP flake; (D): the optical image of this BP flake after 550 K heating process for 25 minutes, and the inset AFM line-scan profile indicated its thickness to be 49 nm; (E) - (F): Raman images ( $A_g^1$ and $A_g^2$ modes) of this BP flake after 550 K heating process; . . . . .	53
Figure 2.6	Sublimation study of BP at 450 K ( $\sim 180$ °C). (A): the BP samples heated at 450 K for 1 minute; (B): the BP samples heated at 450 K for 61 minutes; (C): zoom in of the sample in the center of (A); (D): zoom in of the sample in the center of (B).	55
Figure 2.7	Sublimation study of BP at 500 K ( $\sim 230$ °C). (A): the BP samples heated at 500 K for 1 minute; (B): the BP samples heated at 500 K for 61 minutes; (C): zoom in of the sample in the center of (A); (D): zoom in of the sample in the center of (B).	56
Figure 2.8	Sublimation study of BP at 550 K ( $\sim 280$ °C). (A): the BP samples heated at 550 K for 1 minute; (B): the BP samples heated at 550 K for 61 minutes. . . . .	57
Figure 2.9	Sublimation study of BP at 600 K ( $\sim 330$ °C). (A): the BP samples heated at 600 K for 1 minute; (B): the BP samples heated at 600 K for 41 minutes; (C)-(K): the zoom-in optical images of the sample in the center at (A) heated at 600 K for 1, 21, 31 and 41 minutes, respectively. . . . .	58

Figure 2.10	Sublimation study of BP samples on another piece of Si wafer at 600 K ( $\sim 330$ °C). (A): the BP samples heated at 600 K for 1 minute; (B): the BP samples heated at 600 K for 46 minutes; (C)-(K): the zoom-in optical images of the sample in the center at (A) heated at 600 K for 1, 11, 20, 30, 40, 42, 43, 44 and 46 minutes, respectively. . . . .	59
Figure 2.11	Sublimation study of BP at 620 K ( $\sim 350$ °C). (A): the BP samples heated at 620 K for 1 minute; (B): the BP samples heated at 620 K for 9 minutes; (C)-(H): the zoom-in optical images of the marked sample in (A) heated at 620 K for 1, 2, 3, 4, 5, 6, 7, 8 and 9 minutes, respectively. . . . .	60
Figure 2.12	Sublimation study of BP at 670 K ( $\sim 400$ °C). (A): the BP samples heated at 670 K for 1 minute; (B): the BP samples heated at 670 K for 22 minutes; (C)-(G): the zoom-in optical images of the marked sample in (A) heated at 670 K for 1, 5, 10, 15 and 22 minutes, respectively. . . . .	61
Figure 2.13	(A): Optical image of the 36-nm-thick sample used in Section 2.2.1.3 (P 52); (B): 3D AFM images of the 36-nm-thick sample shown in (A); (C): Optical image of this sample after thinning down to 18-nm-thick; (D): 3D AFM images of the 18-nm-thick shown in (C). . . . .	63
Figure 2.14	(A): Optical image of a prepared 10-nm-thick sample on polyimide substrate; (B): 3D AFM images of the 10-nm-thick sample shown in (A); (C): Optical image of a prepared 20-nm-thick sample on polyimide substrate; (D): 3D AFM images of the 20-nm-thick sample shown in (C). . . . .	64
Figure 2.15	(A): Optical image of sample A; (B): the Raman spectrum with the maximum intensity of $A_g^1$ mode and the minimum intensity of $A_g^2$ mode; . . . . .	67
Figure 2.16	(A): Optical image of sample B; (B): the Raman spectrum with the maximum intensity of $A_g^1$ mode and the minimum intensity of $A_g^2$ mode; . . . . .	69

Figure 2.17	(A): Optical image of sample A to be heated at 500 K; (B) the illustration of the interrupted heating process (5 cycles) to be performed at sample A; (C): Optical image of sample B to be heated at 500 K. (D): the illustration of periodic heating process (6 cycles) to be performed on sample B. . . . .	70
Figure 2.18	(A): Thickness in different areas of sample A as a function of time, and (B): the thickness in different areas of sample B as a function of time. At each red dot, a Raman spectrum was collected (analysis of those collected Raman spectra would be discussed in Section 3.3.2 (P 118) of Chapter 3). . . . .	71
Figure 2.19	(A): Optical image of area 3 in Sample A, and the inset AFM profile indicated it was thinned down to 5-nm-thick; (B): Raman spectrum of the 5-nm-thick BP sample showing the 3 characteristic peaks of BP. . . . .	72
Figure 2.20	Thickness-color map: the colors were extracted from those sample of which the thicknesses had been measured by AFM; .	73
Figure 2.21	(A) & (B): Optical images of Sample C before and after continuous heating process at 500 K, the heating time was 221 minutes; (C) & (D): Optical images of Sample D before and after continuous heating process at 550 K, the heating time was 51 minutes. The inset profile in each picture is the line-scan AFM profile indicating the thickness of this sample. . . . .	75
Figure 2.22	Sample C was annealed at 500 K for 221 minutes. . . . .	76
Figure 2.23	In-situ Raman spectra of the sample C at 500 K. . . . .	76
Figure 2.24	Sample D was annealed at 550 K for 51 minutes. . . . .	77
Figure 2.25	In-situ Raman spectra of the sample D at 550 K. . . . .	77
Figure 2.26	Comparison of thinning rates of sample A and C. . . . .	78
Figure 2.27	Comparison of thinning rates of sample B and D. . . . .	79
Figure 2.28	(A): Optical image the BP sample thinned down to 2-nm-thick; (B): Raman spectrum collected at the circled area in (A); (C) & (D): Spatial Raman maps of sample shown in (A). . . . .	80



Figure 2.29	(A): Optical image the BP sample thinned down to 2-nm-thick, and the inset figures represent the spatial AFM image and thickness profile of circled area. (B) - (D): Optical contrast analysis of Fig 2.28 (A), which was splitted into R, G and B channels, and the G channel figure in (C) was selected for analysis. . . .	81
Figure 2.30	(A): Optical image a BP sample thinned down to 3 and 4 - layers, and the inset figure represents the original BP sample. (B); Raman spectra collected in circled area in (A); (C) - (E): Spatial Raman maps of the BP sample shown in (A); (F) - (H): Optical contrast analysis of (A), which was splitted into R, G and B channels, and the G channel figure in (C) was selected for analysis. . . . .	83
Figure 2.31	(A): Optical image of a BP sample thinned down to 4 layers, and the inset figure represents the original BP sample. (B); Raman spectra collected in circled area in (A). (C) - (E): Spatial Raman maps of the BP sample shown in (A). (F) - (H): Optical contrast analysis of (A), which was splitted into R, G and B channels, and the G channel figure in (C) was selected for analysis. . . . .	85
Figure 2.32	(A): Optical image of a BP sample thinned down to 4 and double layers, and the inset figure represents the original BP sample. (B); Raman spectra collected in circled area in (A). (C) - (E): Spatial Raman maps of the BP sample shown in (A). (F) - (H): Optical contrast analysis of (A), which was splitted into R, G and B channels, and the G channel figure in (C) was selected for analysis. . . . .	86
Figure 2.33	(A): Optical image of a BP sample thinned down to single layer. (B): Raman spectra of this sample collected at 3 regions.	87
Figure 3.1	(A): AFM profile of a blank Si wafer, which indicates its roughness to be $\sim 0.6$ nm; (B): AFM profile of a blank polyimide wafer, which indicates its roughness to be $\sim 1$ nm; . . . . .	92

Figure 3.2	Illustration of ARPRS experiment setup: the optical path of the Raman system under “parallel” configuration. . . . .	93
Figure 3.3	(A): Optical image of the BP sample on SiO <sub>2</sub> / Si substrate rotated at the position with maximum Raman intensity of A <sub>g</sub> <sup>1</sup> mode and (B): at the position with the maximum Raman intensity of A <sub>g</sub> <sup>2</sup> mode. The circled area indicates where the Raman spectra were collected; . . . . .	95
Figure 3.4	(A) & (C): Raman spectra of the BP sample on SiO <sub>2</sub> / Si substrate shown in Fig 3.3 (A), in which the A <sub>g</sub> <sup>1</sup> mode showed maximum Raman intensity; (B) & (D): Raman spectra of the BP sample shown in Fig 3.3 (B), in which the A <sub>g</sub> <sup>1</sup> mode showed maximum Raman intensity. Raman measurements shown in (A) & (B) were performed using the excitation wavelength of 442 nm while those in (C) & (D) were by 633 nm. . . . .	96
Figure 3.5	ARPRS results with 442 nm excitation: (A): the polar diagram of A <sub>g</sub> <sup>1</sup> mode; (B): the polar diagram of B <sub>2g</sub> mode; (C): the polar diagram of A <sub>g</sub> <sup>2</sup> mode. ARPRS results with 633 nm excitation: (D): the polar diagram of A <sub>g</sub> <sup>1</sup> mode; (E): the polar diagram of B <sub>2g</sub> mode; (F): the polar diagrams of A <sub>g</sub> <sup>2</sup> mode. The arrows in figures indicate the two axes of BP (zigzag and armchair). . .	98
Figure 3.6	“Sample A”. Raman intensities of A <sub>g</sub> <sup>1</sup> and A <sub>g</sub> <sup>2</sup> modes and underlying (100) Si wafer as functions of the rotation angle. . . .	123
Figure 3.7	“Sample B”. Raman intensities of BP A <sub>g</sub> <sup>1</sup> and A <sub>g</sub> <sup>2</sup> modes and underlying Si(100) as functions of the rotation angle. . . . .	124
Figure 3.8	Room temperature Raman intensity ratios of $\frac{Si}{A_g^2}$ as a function of thickness measured by AFM, here the blue line represents the sample A and the red line represents sample B. . . . .	126
Figure 3.9	High temperature Raman intensity ratios of $\frac{Si}{A_g^2}$ as a function of measured thickness, here the blue line represents sample A treated at 500 K and the red line represents sample B at 550 K. . . . .	127
Figure 3.10	High temperature Raman intensity ratios of $\frac{Si}{A_g^2}$ as a function of measured thickness, here the blue line represents sample A treated at 500 K and the red line represents sample B at 550 K. . . . .	128

# Glossary

<b>AFM</b>	Atomic Force Microscopy
<b>ARPRS</b>	Angle-resolved Polarized Raman Spectroscopy
<b>BP</b>	Black Phosphorus
<b>CO</b>	Crystallographic Orientation
<b>IR</b>	Infra-red
<b>IC</b>	integrated circuit
<b>TMDCS</b>	Transition Metal Dichalcogenides
<b>2D</b>	2-Dimensional
<b>3D</b>	3-Dimensional
<b>CVD</b>	Chemical Vapor Deposition
<b>PLD</b>	Plasma Laser Deposition
<b>TEM</b>	Transmission electron microscopy

# Acknowledgments

*”To explain all nature is too difficult a task for any one man or even for any one age. ’Tis much better to do a little with certainty and leave the rest for others that come after you.”*

— Isaac Newton

During my master’s study, I am very happy to have many great people standing on my side all the time.

I would like to express my gratitude to my supervisor, Dr. Guangrui Xia. It has been my honor to be her fourth M.A.Sc. student. Under her supervision, I learned how to conduct good research. Her guidance, patience, trust and time enabled my research to be productive and very enjoyable. I would like to thank Mr. David Tuschel from Horiba Scientific (U.S.A), for offering me generous advice on both Raman theory and experimental operations of Raman spectrometer. I would like to thank Texas Instruments (TI, U.S.A), for sponsoring me with the 2-year research fellowship during my M.A.Sc study. I would like to thank Professor Joshua Folk from UBC Physics & Astronomy and Professor Chad Sinclair from UBC Materials Engineering to sit on my thesis committee. I would like to thank Professor Xi Ling from the Department of Chemistry at Boston University (U.S.A) to give me much advice in research.

I would like to thank Dr. Yiheng Lin, my former colleague and friend, for his kind and patient instructions. I felt very thankful for countless constructive discussions in all kinds of topics with him. I would like to thank Dr. S. Arash

Sheikholeslam, Mr. Rui Yang, Dr. Zihe Ren, Ms. Zenan Jiang, Mr. Joshua Cantin for their kind help in my research and life. I feel surely thankful to my colleagues, Mr. Jiaxin Ke, Mr. Guangnan Zhou, Mr. Yunlong Zhao and Mr. Qian Song for helpful discussions.

I would give my sincere thanks to Professor Olav Slaymaker from UBC Geography, for his kind guidance in helping me to keep in faith and go through the hardest time in my master's study. I would thank to Gordon and Ute Carkner, sincerely for praying and sharing the love of god, for teaching me how to be a kind person. I would like to thank those whose names haven't been mentioned here, I know many people helped me more or less in my life. I will contribute my best to the society.

Last, but the most importantly, I would like to thank my family, especially my parents, thank you for your strong and all-round support in my whole life. Love you!

# Chapter 1

## Introduction

*“I don’t know how to do this on a small scale in a practical way, but I do know that computing machines are very large; they fill rooms. Why cant we make them very small, make them of little wires, little elements, and by little, I mean little?”*

— Richard Feynman

### 1.1 Background And Motivations

Since the physical limitation of the dimensionality of bulk Si impedes the shrinkage of transistors, and hurdles the promotion of device performance according to Moore’s law. According to the 2016 International Technology Road map for Semiconductors (ITRS) [27], the adoption of low-dimensional new materials becomes a critical issue.

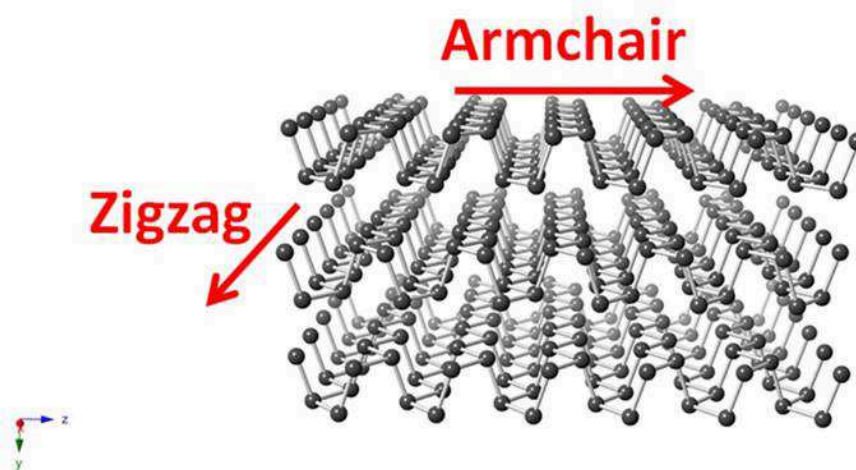
Two-dimensional (2D) materials, such as graphene, black phosphorus, molybdenum disulfide ( $\text{MoS}_2$ ) and other members of the transition metal dichalcogenides (TMDCS) family, represents the potential solutions of materials beyond conventional silicon for the further development of scaling-down-dimensions in “More than Moores Law” [28][29].

2D BP was first isolated from bulk BP in 2013 [3] by the mechanical exfoliation method [30], and it has been shown to have many unique and useful properties

in flexible and ultra-thin electronics [31][32][33][34] and photonics [35][36][37][38][39][40].

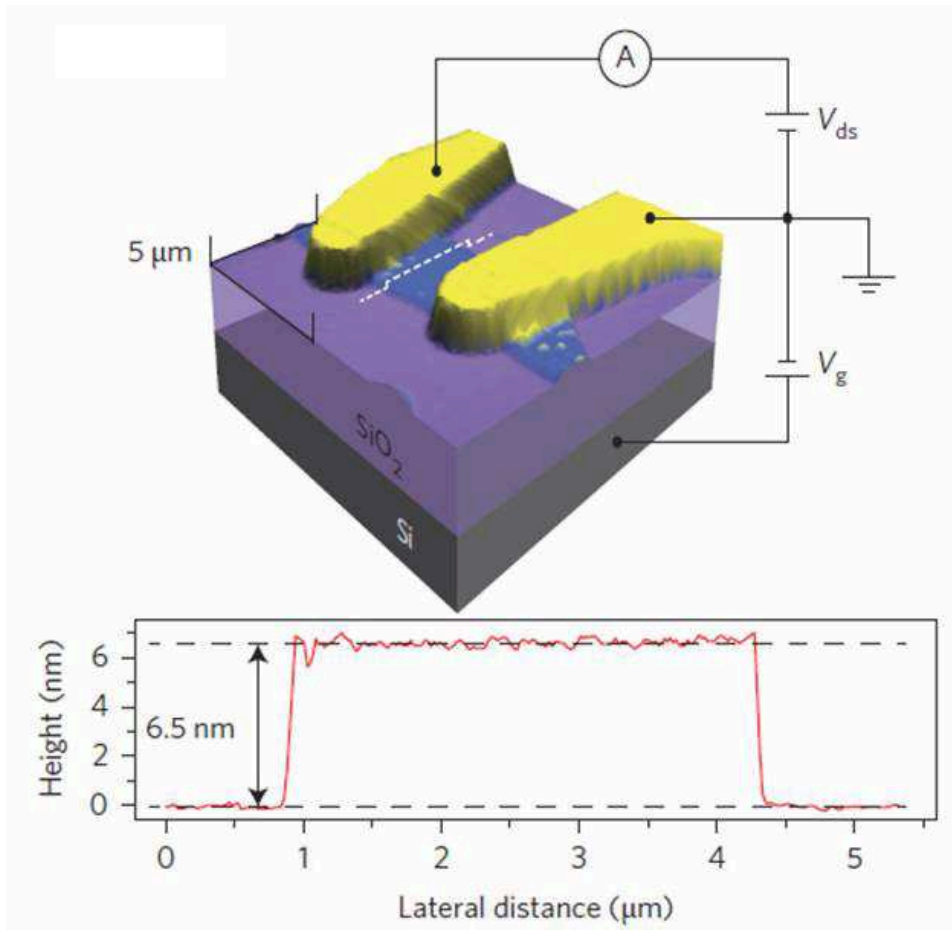
### 1.1.1 BP Structure: Layer-stacked 2D Semiconductor Material

Semiconducting orthorhombic black phosphorus (BP), like graphene, is a layer-stacked 2-dimensional (2D) nanomaterial with  $sp^3$ -hybridized phosphorus atoms covalently bonded to a puckered structure via weak van der Waals forces between layers [41]. The atomic structure of BP is shown in Fig 1.1. Bulk BP was first synthesized in 1914 by applying high hydrostatic pressure of 1.2 GPa at an elevated temperature of 200 °C on white phosphorus [42].



**Figure 1.1:** The atomistic ball-stick models of few-layer black phosphorus.

In 2013, Li et al. [3] first reported the successful mechanical exfoliation of few-layer black phosphorus and preparation of a BP based field-effect transistor (See Fig 1.2). After that work, the atomically thin BP, which is also termed as “few-layer phosphorene”, attracted great attentions in studying it as a new 2D semiconductor material.

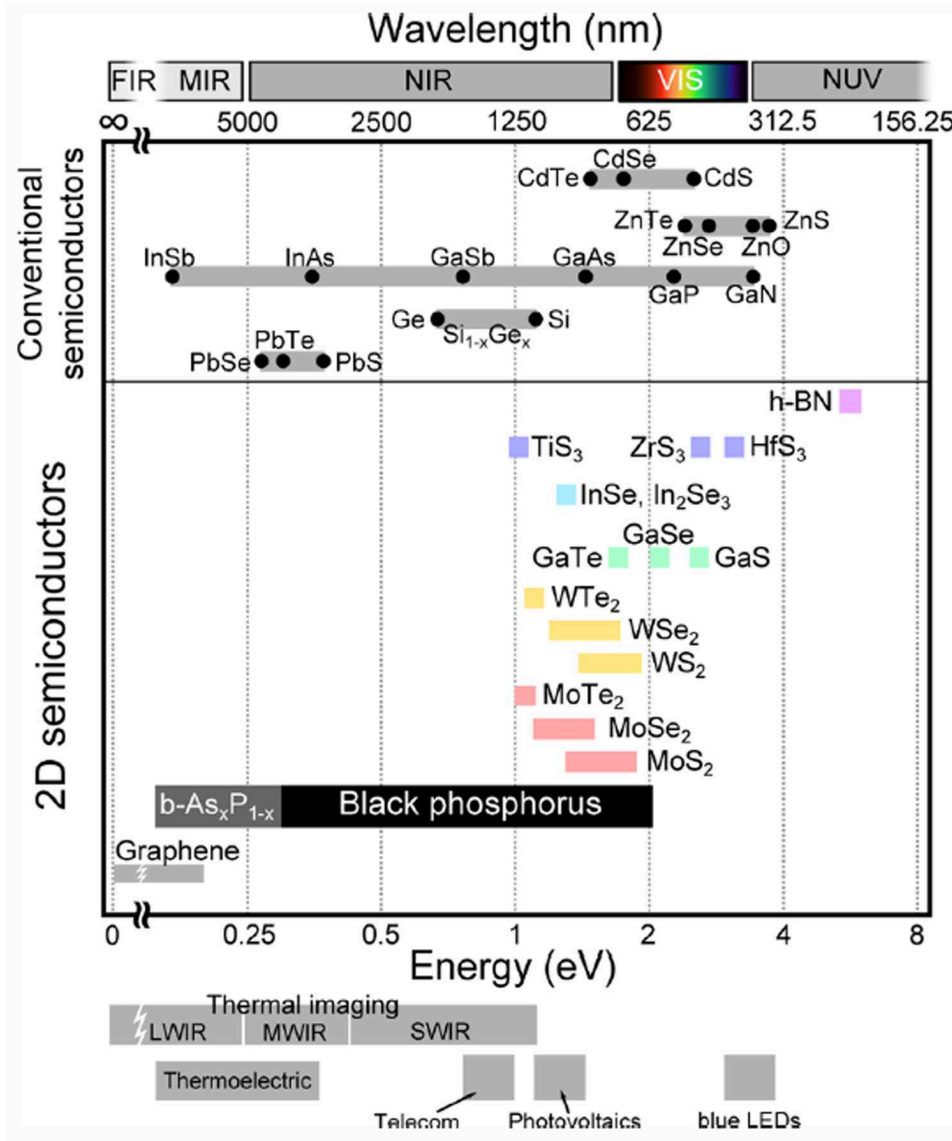


**Figure 1.2:** The first BP based transistor which was fabricated on a piece of 6.5-nm-thick mechanically exfoliated BP sample. Figure is reprinted from [3] with permission.

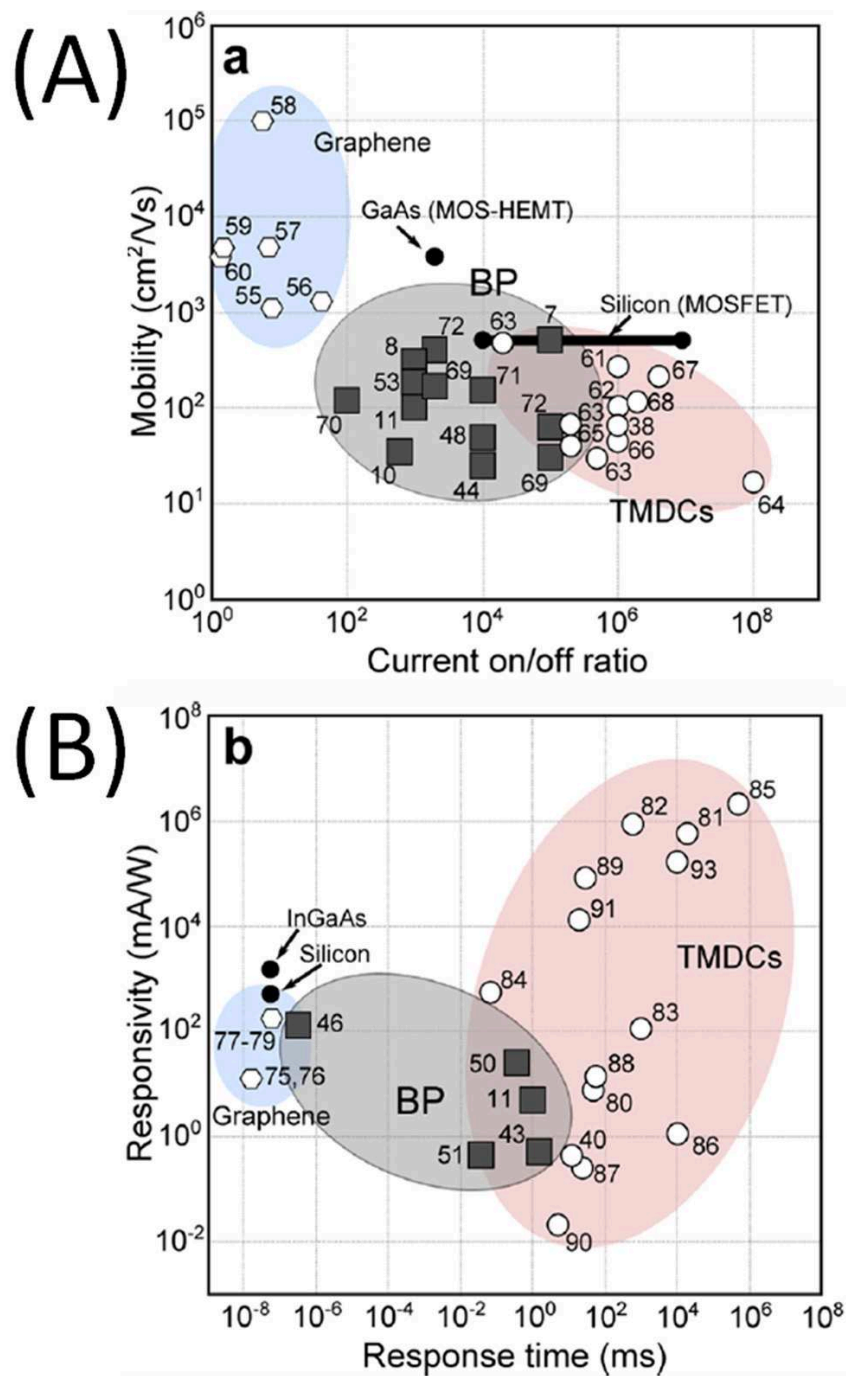


### **1.1.2 Layer-dependent Tunable Band Gap, High Carrier Mobility, Fast And High Photo-response**

BP always has a direct band gap at the  $\Gamma$  point of the Brillouin zone regardless of layer numbers, which is different from the single-layer-only direct bandgap of semiconducting transition metal dichalcogenides (TMDCS) such as MoS<sub>2</sub>, WS<sub>2</sub> and WSe<sub>2</sub> [43][44][45], and the zero band gap of graphene. In Fig 1.3, the band gap range [46] of BP is compared with other major 2D and bulk semiconductors. The energy band gap of single layer BP of 2.05 eV has been measured by scanning tunneling spectroscopy (STS) [47]. With the increasing number of layers, the band gap decreases and finally reaches 0.3 eV for bulk BP (thickness > 10 nm) [3][48][49], which covers the gap between graphene and TMDCS for 2D materials. In the range of 0.3 - 1 eV, BP is the only 2D semiconductor material that is suitable for thermal imaging, thermoelectrics [50][51], infra-red detection [52], telecom [35] and photovoltaics [35][53] applications. In addition, Fig 1.4 (A) compares 2 major figures of merits for materials for transistor applications: carrier mobility and “current on/off ratio”. It can be seen that BP not only has a carrier mobility close to silicon but also has a reasonable current on/off ratio; in Fig 1.4 (B), it shows that the photo-response of BP has high responsivity of photo-current like graphene while also has a fast response time like TMDCS. Overall, those properties enable BP to be a promising candidate for applications in field-effect transistors [3][54][55][56][57][58] and photo-detectors [59][60].



**Figure 1.3:** The band gap range of 2D and conventional bulk semiconductors. Figure is reprinted from [4] with permission.



**Figure 1.4:** (A): mobility and current on/off ratio of BP; (B): the photo-responsivity and response time of BP. Figure is reprinted from [4] with permission.

### 1.1.3 Strong In-plane Anisotropies Of Black Phosphorus

#### 1.1.3.1 Anisotropic Transport Property

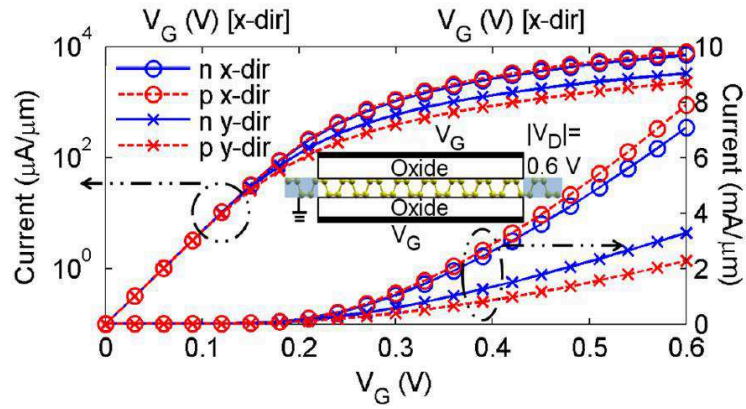
Because of the puckered honeycomb orthorhombic structure, many basic physical properties of BP show strong in-plane anisotropies. For instance, by applying the same biasing voltage, the “armchair” direction provides higher drive current than the “zigzag” direction, since the effective carrier masses in the “armchair” direction are significantly lighter than those in the “zigzag” direction [5]. The definition of “armchair” direction can be seen in Fig 1.1, which is the “z axis” perpendicular to the ridge direction, and the “zigzag” one is the “x axis” parallel with the ridge direction.

Fig 1.5 (A) illustrates that, in the “armchair” direction (the “x” direction), due to similar carrier masses of electron ( $0.17 m_0$ ) and holes ( $0.16 m_0$ ), the  $I_{ON}$  (see “blue” and “red” circles in the upper part of the diagram) of n- and p-type device are almost the same; but in the “zigzag” direction (the “y” direction), because of the heavier effective masses of holes, the p-type device has notably lower  $I_{ON}$  than that of the n-type device.

(A)

Lattice ( $\text{\AA}$ )	$a = 4.5694$	$b = 3.3255$	$c = 15$
Atom positions ( $\text{\AA}$ )	$(0.0860 a, b/2, 2.1360)$	$(0.4140 a, 0, 2.1360)$	
	$(0.5860 a, 0, 0)$	$(0.9140 a, b/2, 0)$	
Electron $m^*$ ( $m_0$ )	0.17 (x)	1.20 (y)	
Hole $m^*$ ( $m_0$ )	0.16 (x)	6.49 (y)	

(B)

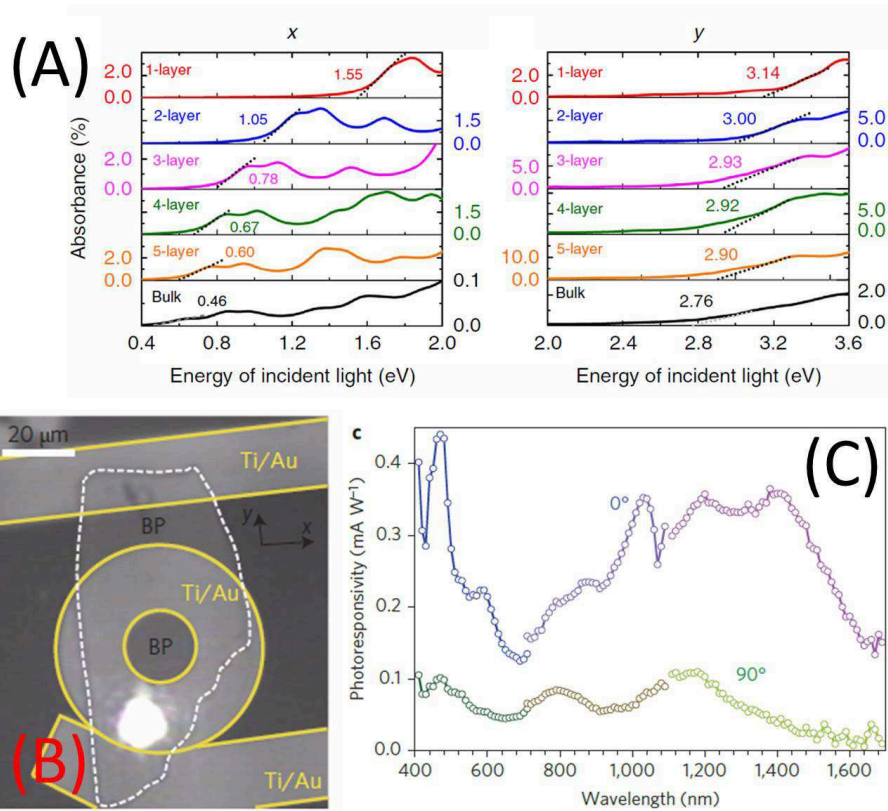


**Figure 1.5:** (A): Material parameters of single-layer BP; (B): the current characteristics of the n-type (solid) and p-type (dash) BP field-effect transistors at the x- (“zigzag”) and y-direction (“armchair”).  $m_0$  is the free electron mass which has a value of  $9.1 \times 10^{-31}$  kg. Figure is reprinted from [5] with permission.

Despite of this high-degree anisotropy of the transport property of BP, the relatively high carrier mobility (see Fig 1.3 (A)), and the large on / off ratio makes encapsulated few-layer BP promising for complementary metal-oxide semiconductor (CMOS) devices [61], especially in ultra-thin and wearable electronics.

### **1.1.3.2 Anisotropic Optical Property**

BP is a linear dichroism crystal [6][59]. In other words, it shows a strong anisotropy of the light absorption. For example, in Fig 1.6 (A), Qiao et al. [6] studied the light absorption of the “x” (“armchair”) and “y” (“zigzag”) direction of BP with different thickness, and indicated that absorption edges were from 1.55 eV (monolayer BP) to 0.46 eV (bulk BP) for the “x” direction; while those for the “y” direction were from 3.14 eV (monolayer BP) to 2.76 eV (bulk BP). Moreover, in 2015, Yuan et al. [7] first investigated the different broadband photo-responses at the “zigzag” and “armchair” directions by preparing and measuring a black phosphorus vertical p-n junction (see in Fig 1.6 (B)), and their results (see in Fig 1.6 (C)) indicated that the photoresponsivity of the “armchair” direction was notably 3.5 times greater than that of the “zigzag” direction.



**Figure 1.6:** (A): Light absorption of BP with different thickness (Figure is reprinted from [6] with permission), here the “x” denotes for the “arm-chair” direction and the “y” denotes for the “zigzag” direction; (B): a black phosphorus vertical p-n junction (Figure is reprinted from [7] with permission); (C): the photoresponsivity of the BP p-n junction shown in (B), here 0° represents the “armchair” direction and 90° represents the “zigzag” direction.

### 1.1.3.3 Anisotropic Thermal Conductivity

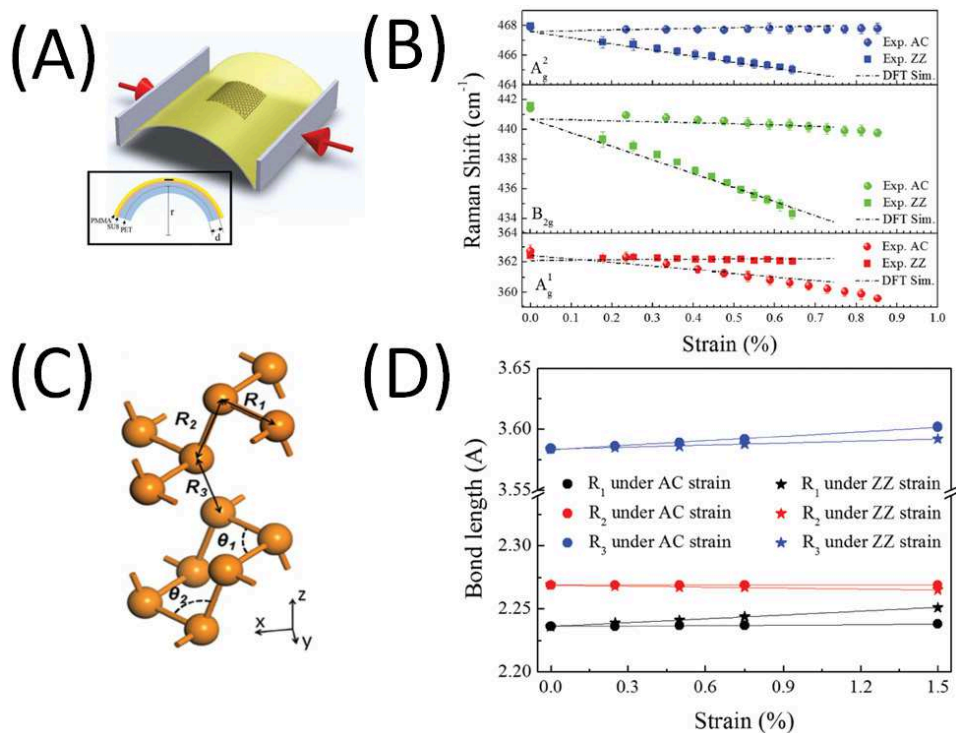
Moreover, the thermal conductivity of BP also shows a strong in-plane anisotropy. For instance, Luo et al. [62] investigated the “zigzag” and “armchair” thermal conductivities of different thickness of BP, which showed that, for BP thicker than 15 nm, the “armchair” thermal conductivity has a value of  $\sim 20 \text{ Wm}^{-1}\text{K}^{-1}$  while the “zigzag” one is  $\sim 40 \text{ Wm}^{-1}\text{K}^{-1}$ . However, for BP thinner than 15 nm, the “armchair” and “zigzag” thermal conductivities decrease to  $\sim 10 \text{ Wm}^{-1}\text{K}^{-1}$  and  $\sim 20 \text{ Wm}^{-1}\text{K}^{-1}$ , respectively.

### 1.1.3.4 Anisotropic Strain-induced Raman Response

Recently, Li et al. [8] investigated the anisotropic Raman shifts of the vibrational modes of BP by applying a uniaxial strain along either the “zigzag” direction or the armchair direction. In Fig 1.7 (A), it illustrates the uniaxial strain is applied to the specific “zigzag” or “armchair” direction of the BP sample through bending the flexible polyethylene terephthalate (PET) substrate after determining the CO. In Fig 1.7 (B), their experiment results of the strain-induced Raman spectra indicated that, when the uniaxial tensile strain is applied along the “AC” (“armchair”) direction, the Raman peak positions of in-plane vibrational  $A_g^2$  and  $B_{2g}$  modes can be shifted by  $-3$  and  $-11 \text{ cm}^{-1}/\%$ , while the out-of-plane vibrational  $A_g^1$  mode almost remains at its original peak position. On the other side, when the uniaxial tensile strain is applied along the “ZZ” (“zigzag”) direction, the  $A_g^1$  mode can be shifted by  $-3 \text{ cm}^{-1}/\%$  while  $A_g^2$  and  $B_{2g}$  modes don’t undergo obvious shifts of the peak positions. This anisotropy of strain-induced Raman shifts of the 3 Raman modes of BP can be explained by the bond lengths of the P atoms. In Fig 1.7 (C), the “R1” and “R2” represent the in-plane atomic bonding while the “R3” represents the atomic bonding of the interlayer. In Fig 1.7 (D), it shows that, except for “R2”, the bond lengths of “R1” and “R3” differ under uniaxial “ZZ” (“zigzag”) strain and “AC” (“armchair”) strain, and obviously the bond length of “R1 (the in-plane atomic bond) is affected by the uniaxial tensile strain “ZZ” (“zigzag”), corresponding to the relative large red shifts of the in-plane  $B_{2g}$  and  $A_g^2$  modes shown in Fig 1.7 (B), but for the bond length of “R3”, the “AC” (“armchair”) strain affects more



than the “ZZ” strain does, and considering the “AC” and “ZZ” strain affect it much less than the in-plane “R1, the relative weak red-shifts of the  $A_g^2$  mode under “ZZ” strain shown in Fig 1.7 (B) can be explained.



**Figure 1.7:** The strain anisotropy of BP (Source: Ref [8]. Copyright 2016 American Chemical Society Reprinted with permission.). (A): Illustration of applying uniaxial tensile strain on the BP sample. (B): Uniaxial “AC” (“armchair”) and “ZZ” (“zigzag”) tensile strain-induced Raman shifts of the  $A_g^1$ ,  $B_{2g}$  and  $A_g^2$  modes. (C): Definitions of the P-P bond lengths of “R1”, “R2” and “R3”. (D): Strain-induced changes of the bond lengths.

## 1.2 Current Challenges In BP Study

### 1.2.1 Degradation Of BP In Air

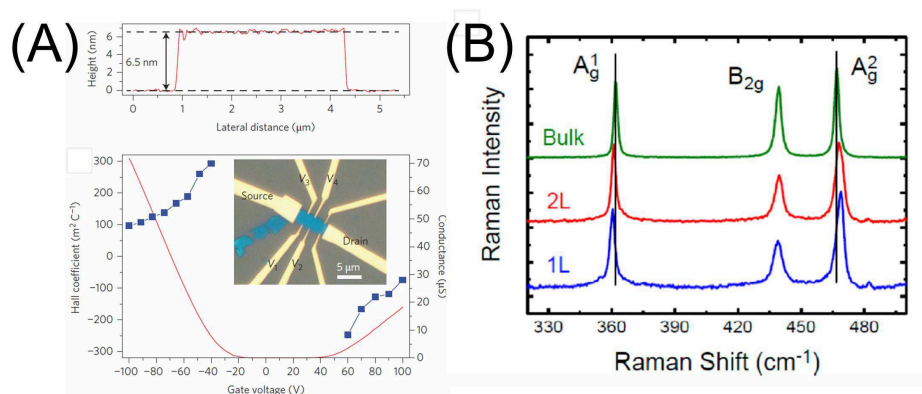
So far, there remain 3 major challenges for BP research: the air-stabilization and the controllable fabrication of atomically thin BP layers [4]. The oxidation conditions of BP have been widely studied before: Favron et al. [63] first indicated that light, oxygen and water were three factors cause the oxidation of BP; Luo et al. [64] reported that with 5% oxygen/Ar or 2.3% H<sub>2</sub>O/Ar, the oxidation rate was  $< 5\text{\AA}$  for 5h from XPS results; Wang et al. [65] reported BP could remain stable in pure water without the presence of oxygen molecules from nuclear magnetic resonance (NMR) spectroscopy results; Li et al. [66] reported that heating could remove the metastable oxygen adsorbed on the surface of BP. In order to solve this problem, the passivation of BP was successfully achieved via both chemical modification method like covalent aryl diazonium functionalization [67] and physical encapsulation methods such as atomic layer deposited dielectric passivation [68] or h-BN passivation [64].

### 1.2.2 Fabrication Of Large-scale Few-layer Crystalline BP

Let us look at the current fabrication methods in preparing few-layer black phosphorus thin films. The top-down and bottom-up methods are two approaches towards few-layer BP. Current top-down methods towards ultra-thin BP such as mechanical exfoliation by Scotch<sup>TM</sup> tapes [3][59], shear exfoliation [69][70][71] in liquids, plasma thinning [12][72][73], anodic oxidation and water rinsing [13] still couldn't be used for scalable and controllable production of large uniform crystalline few-layer BP thin films. In addition, the quality (uniformity, scalability and crystallinity) of few-layer BP made by pulsed laser deposition [14][15] and chemical vapor deposition [14] (CVD) have not been sufficient for industry applications. Hence, developing a scalable and controllable massive fabrication method of few-layer BP thin films with good uniformity and crystallinity will greatly promote the wide application of BP. The details of the preparation methods of BP mentioned above were discussed below.

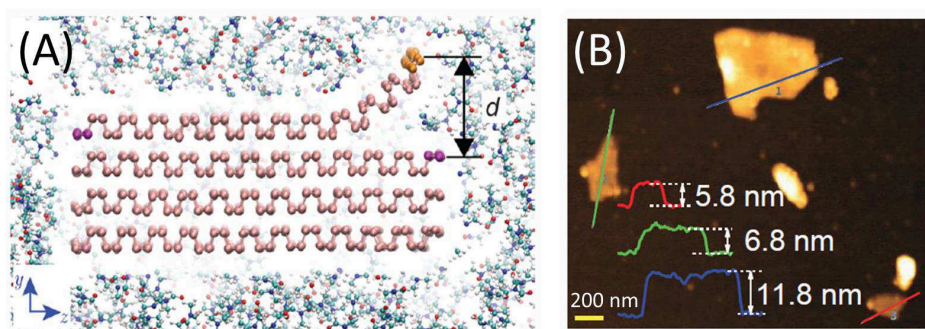
## Mechanical Exfoliation

Mechanical exfoliation of 2D materials such as graphene by Scotch<sup>TM</sup> tapes, was first demonstrated by Novoselov et al. [30], which is the most conventional method in preparing few-layer BP samples. In Fig 1.8 (A), the first BP-based field-effect transistor was fabricated on an 6.5-nm-thick exfoliated black phosphorus flake with an area around  $50 \mu\text{m}^2$ ; and Fig 1.8 (B) shows the comparison among the exfoliated single-layer, bilayer and bulk BP. However, the poor scalability and uniformity of prepared samples via the Scotch<sup>TM</sup> tapes based exfoliation method made it unsuitable for industrial applications.



**Figure 1.8:** Mechanical exfoliation of black phosphorus. (A): A 7.5-nm-thick BP sample based field-effect-transistors (Figure is reprinted from [3] with permission); (B): Raman spectra of single-layer and bilayer phosphorene and bulk black phosphorus films. (Figure is reprinted from [9] with permission).

## Sonication Of BP In Liquid Solutions



**Figure 1.9:** (A): Illustration of liquid exfoliation method (Figure is reprinted from [10] with permission). (B): typical BP products prepared by liquid exfoliation method (Figure is reprinted from [11] with permission).

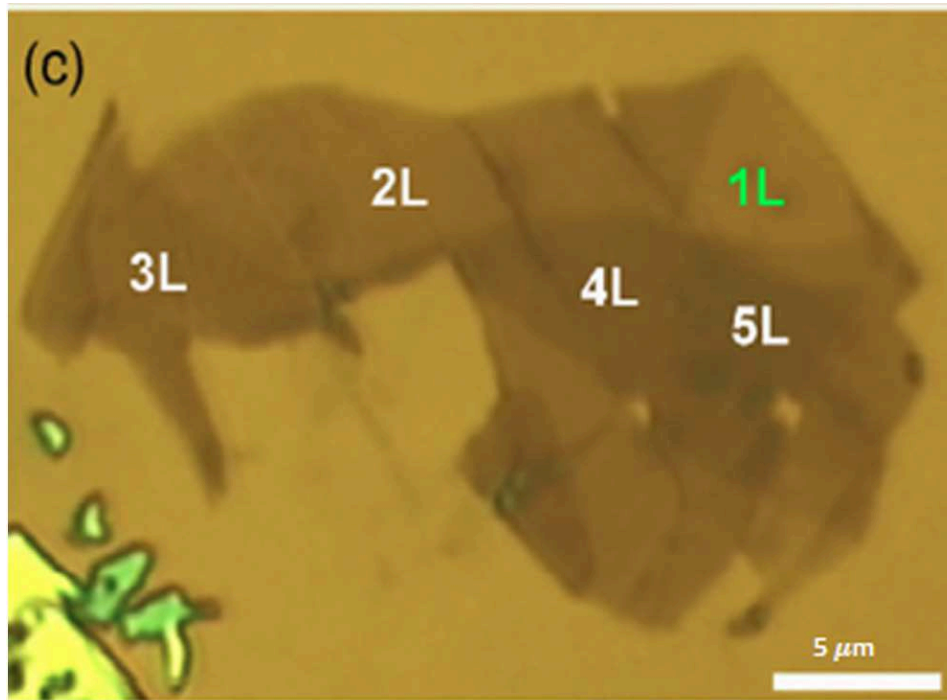
Sonication of BP in liquid solutions [69][11][74][75] is another mechanical exfoliation method using liquid solutions for the isolation of BP. The exfoliation mechanism can be illustrated as seen in Fig 1.9 (A): the solvent molecules act as wedges and peel a piece of monolayer BP from bulk BP. Fig 1.9 (B) shows the typical BP products prepared by liquid exfoliation method which have their areas less than  $1 \mu\text{m}^2$ . In addition, previous studies on liquid exfoliation of BP were summarized in Table 1.1, which indicates this method is incapable of preparing single-layer BP which has a thickness of 0.53 nm [49][63]. Though the liquid exfoliation method could be used for massive and economic production of few-layer crystalline BP, the lack of uniformity and scalability of final products still hurdles its future prospect for applications.

**Table 1.1:** Previous studies on liquid exfoliation of BP [1]. \*aq.: deoxy-generated water.

Solutions	Thickness of prepared BP (nm)	Reference number
<i>Organic solvents</i>		
DMSO	15 - 20	[11]
NMP	1 - 5	[69]
NMP	< 10	[74]
NMP	17.6	[76]
Saturated NaOH NMP solution	2.8 - 5.3	[75]
CHP	9.4 ± 1.3	[70]
<i>Aqueous</i>		
Distilled water	2	[77]
*aq. with 1% w/v Triton X-100 solution	< 20	[78],[79]
*aq. with 2% (wt/vol) SDS	4.5	[76]
<i>Ionic liquids</i>		
[BMIM][TfO]	8.5 - 12.8	[80]
[HOEMIM][TfO]	3.6 - 8.9	[80]

## Plasma Thinning

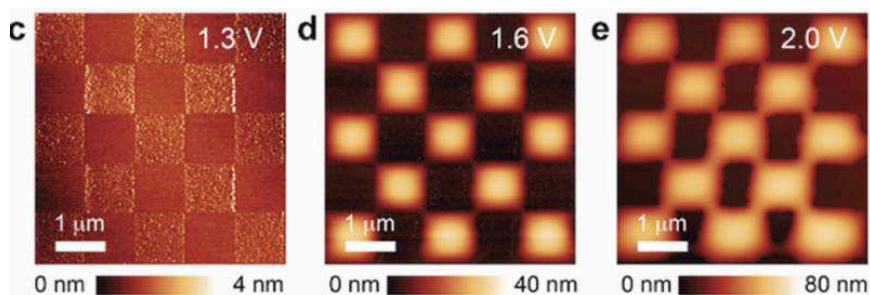
In 2014, Lu et al. [12] reported the successful preparation of monolayer BP film. In Fig 1.10, it shows the BP products prepared by the plasma thinning method: the total area of the products were less than  $300 \mu\text{m}^2$  and the stacked flakes indicated the non-uniformity of BP products. Some other works on plasma thinning of black phosphorus were also reported [81]. The fabrication process can be described as:  $\text{Ar}^+$  plasma was used to etch away the surface phosphorus atoms such that a thick flake could be thinned down. However, the size of the plasma beam and defects introduced by  $\text{Ar}^+$  plasma bombardment cause the non-uniformity and low crystallinity of products.



**Figure 1.10:** The few-layer BP prepared by plasma thinning. (Figure is reprinted from [12] with permission)

## Local Anodic Oxidation And Water Rinsing

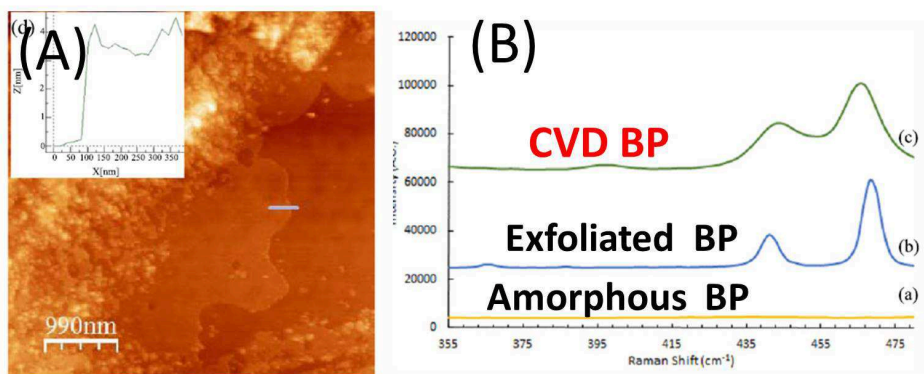
Recently, Liu et al. [13] reported the layer-by-layer thinning of black phosphorus via anodic oxidation and water rinsing method. In Fig 1.11, it shows that the simultaneous thinning of BP layers in each patterned area which has an area of  $1 \mu\text{m}^2$ . However, they didn't thin the sample down to a few layers. The fabrication process can be described as follows: By scanning a BP sample with an AFM tip, the oxidation of the patterned area was realized by applying DC (direct current) bias voltages (the "anodic oxidation") through a tip in the ambient environment; the generated P-O product absorbed water from the ambient environment, and then the liquid-phase patterning byproduct could be easily removed by water rinsing. This method could provide precise control of thinning rates while the uniformity and crystallinity of BP sample are retained. Though this method has its advantages in thickness controllability of bulk BP (thickness more than 10 nm [49]), which are suitable for sub-micro and nano -scale fabrication of prototype devices, the limitations of its scalability, high consumption of expensive AFM tips and introduction of oxygen impurities make it unable to be used for massive and economic production of few-layer crystalline BP thin film.



**Figure 1.11:** The illustration of the layer-by-layer nano-patterning and thinning (by removing the oxidized byproduct through water rinsing) of BP. Figure is reprinted from [13] with permission.

## Chemical Vapor Deposition (CVD)

In 2016, few-layer BP prepared by the chemical vapor deposition (CVD) method was reported by Smith et al. [14]. In Fig 1.12 (A), it shows that the BP products has an area of less than  $1 \mu\text{m}^2$  and the thickness of the sample is not uniform. The fabrication process can be described as follows: an amorphous red phosphorus film was first grown on a clean surface in vacuum environment and then the Sn/SnI<sub>4</sub> mixture was used as catalyst to turn the amorphous red phosphorus into black phosphorus under different temperatures and pressures. It is important to note that, the red phosphorus is made of an amorphous network of phosphorus atoms linked with covalent bonds [82], and BP has a puckered honeycomb structure composed of covalently bonded phosphorus atoms. However, in Fig 1.12 (B), the Raman spectra indicated the qualities of the final BP such as the uniformity and crystallinity still were not as good as the exfoliated BP.

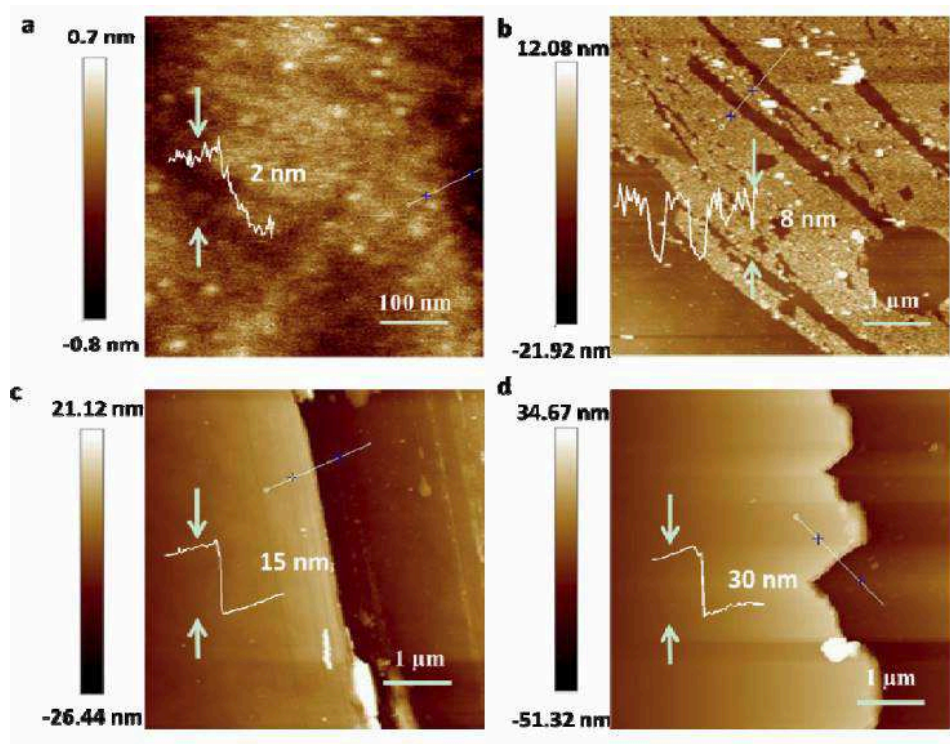


**Figure 1.12:** The few-layer BP prepared by using chemical vapor deposition (CVD) method. (A): the morphology and thickness profile of the final product; (B): the comparison of the Raman spectra of the exfoliated BP, prepared amorphous BP and prepared crystalline BP. Figure is reprinted from [14] with permission.



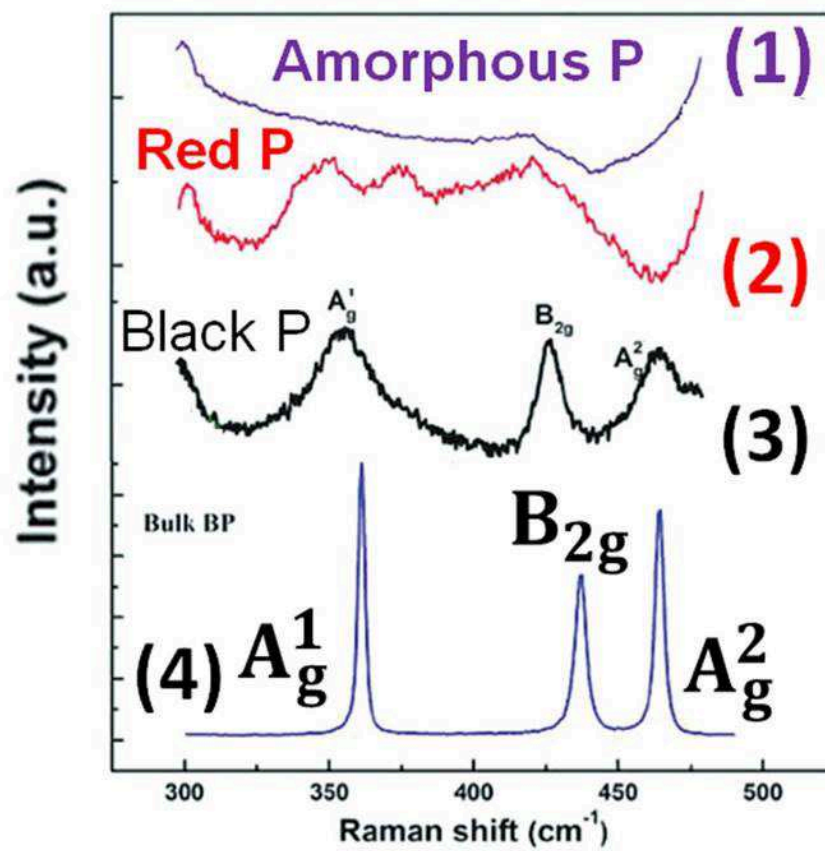
### **Pulsed Laser Deposition (PLD)**

A pulsed laser deposition (PLD) method for preparing few-layer BP was also reported [15]. In Fig 1.13, it shows that the BP product has an area of less than  $30 \mu\text{m}^2$  and the surface of it is non-uniform. The fabrication process can be described as follows: the amorphous few-layer BP film was prepared by ablating a bulk BP crystal as a target material by a KrF pulsed laser ( $\lambda = 248 \text{ nm}$ ) in vacuum environment. It is important to note that black phosphorus has three crystalline phases which are orthorhombic [83], rhombohedral [83], and simple cubic [84], and one amorphous form [85]. Since the final products were in the form amorphous BP in that work, which indicated that this method was incapable of preparing crystalline few-layer BP film.



**Figure 1.13:** The illustration of the few-layer BP prepared by using pulsed laser deposition (PLD) method. Figure is reprinted from [15] with permission

Fig 1.14 shows a comparison of the Raman spectra of BP prepared by mechanical exfoliation, and the black phosphorus, red phosphorus and amorphous phosphorus films prepared by PLD deposition [15]. First of all, the Raman spectrum of the mechanically exfoliated BP showed three strong characteristic peaks at about 360, 438 and 468  $\text{cm}^{-1}$ , respectively; secondly, the Raman spectra of the BP film grown also showed 3 weaker and broader characteristic peaks, and all peak positions red-shifted; thirdly, the Raman spectra of the red phosphorus prepared showed three weak characteristic peaks at around 350, 380 and 440  $\text{cm}^{-1}$ , respectively; fourthly, the Raman spectra of the amorphous phosphorus (see the purple profile) showed no characteristic peaks, and signals shown in profile (1) were from the Si substrate, as amorphous P has no characteristic peaks. The significant difference between the Raman spectra of crystalline BP and amorphous phosphorus of the same chemical composition is primarily because of the presence or absence of spatial order and long-range translational symmetry, respectively [86]. Therefore, Raman spectroscopy can be used for identifying the crystallinity of prepared BP in this work.



**Figure 1.14:** (1) - (4) represent the Raman spectra of amorphous BP, red phosphorus, BP prepared by PLD (Pulsed Laser Deposition) deposition and exfoliated bulk BP. Figure is reprinted from [15] with permission.

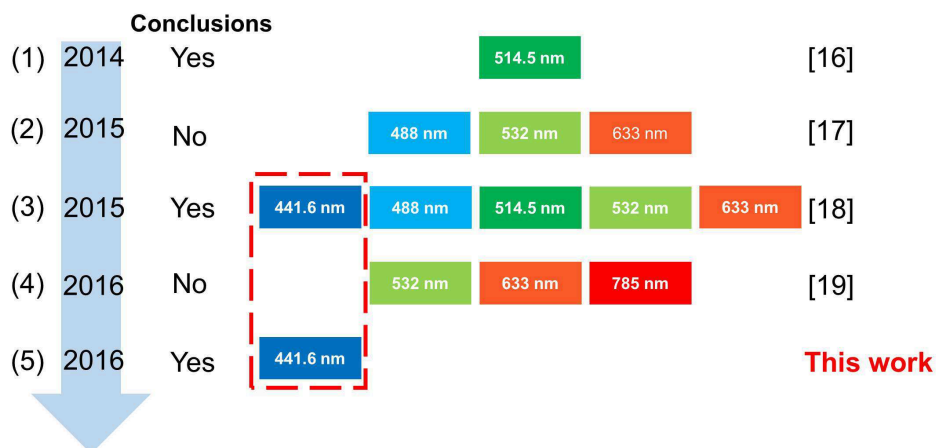
### 1.2.3 Debate On The CO Determination Of BP By ARPRS

Besides the fabrication method, the fast and non-destructive determination of the BP crystallographic orientations still remained unsolved. To date, BP CO could be determined by angle-resolved conductance of BP sheet [59][62][16], diffraction pattern by high-resolution transmission electron microscope [19][46], optical absorption [59][19] and ARPRS. Among them, only ARPRS is a fast, convenient and non-destructive method. However, because the ARPRS response of BP is quite complicated, which depends on the excitation wavelength and thickness [16][17][18][19], there is a debate on whether or not the CO of BP could be simply determined by ARPRS.

Fig 1.15 summarized the 4 previous works, which studied ARPRS of BP before this work. In 2014, Wu et al. [16] first investigated the ARPRS of BP by using the excitation wavelength of 514.5 nm, and summarized that the CO could be determined according to the polar diagrams of the  $A_g^1$  and  $A_g^2$  modes of BP under “parallel” configuration: a relatively larger local maximum peak intensity of  $A_g^2$  mode indicates the “armchair” direction, and a relatively smaller local maximum peak intensity of  $A_g^2$  mode shows at the “zigzag” direction. In 2015, Ribeiro et al. [17] reported the opposite results: when using the excitation wavelength of 532 nm under “parallel” configuration, a relatively larger local maximum peak intensity of  $A_g^2$  mode showed “zigzag” direction and a relatively smaller local maximum peak intensity indicated the “armchair” direction. In addition, they also first indicated that the ARPRS results of BP varied by the excitation wavelength.

In 2015, Kim. et al. [18] investigated the ARPRS of 4 BP samples (5, 65, 70 and 90 -nm-thick) by using the excitation wavelength from 442 to 633 nm under the “parallel” configuration (see Fig 1.16). They first indicated that the CO of BP could be determined by ARPRS with the laser line of 442 nm according to: 1. both  $A_g^1$  and  $A_g^2$  modes show clear bow-tie shapes, and the maximum / minimum intensities of  $A_g^1$  and  $A_g^2$  modes are orthogonal to each other; and 2. the maximum peak intensity of  $A_g^2$  indicates the “armchair” direction, and the maximum peak intensity of  $A_g^1$  mode shows at the “zigzag” direction. However, for longer wave-

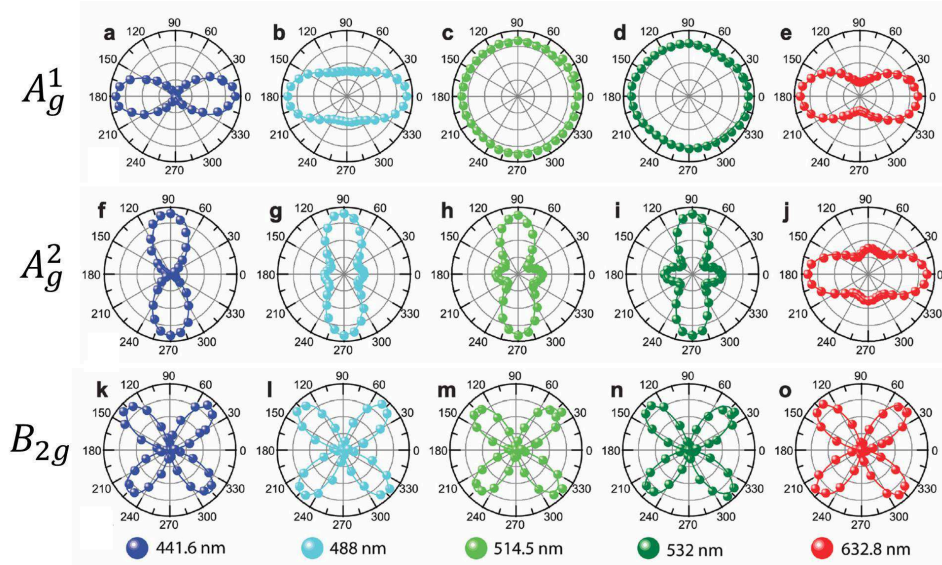
## Can ARPRS be used for CO determination?



**Figure 1.15:** The progress of ARPRS study using different excitation wavelengths in determining CO of BP: (1) [16]; (2) [17]; (3) [18]; (4) [19]; (5) this work.

lengths, the shape of  $A_g^1$  mode showed an oval shape (488 nm), a circular shape (514.5 nm & 532 nm) and a peanut shape; for  $A_g^2$  mode, the polar diagrams (488 - 633 nm) showed two different local maximum Raman intensities at orthogonal directions instead of the bow-tie shape (442 nm), and the relatively larger / smaller local maximum Raman intensity can appear at the angle either perpendicular (488 - 532 nm) or parallel (633 nm) to the angle of the maximum  $A_g^1$  Raman intensity. Therefore, this complexity of ARPRS using wavelength longer than 442 nm makes it hard to identify the CO of BP.

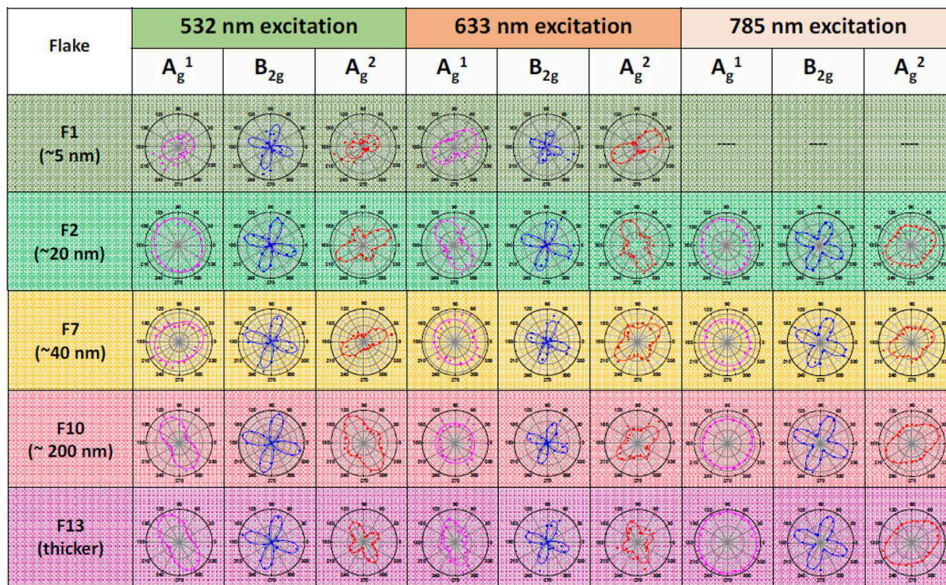
Moreover, in 2016, Ling et al. [19] investigated the ARPRS of 13 BP samples (10 to 200-nm-thick) by using excitation wavelengths of 532, 633 and 785 nm (see Fig 1.17). They indicated that the polar diagrams of  $A_g^1$  and  $A_g^2$  of BP were not only wavelength-dependent but also thickness-dependent. For instance, in Fig 1.17, under the 633 nm laser, the  $A_g^1$  mode has a peanut shape (F1,  $\sim 5$  nm), an oval shape (F7,  $\sim 40$  nm) and a circular shape (F 10,  $\sim 200$  nm) for different thickness. What's more, the relative larger / smaller local maximum Raman intensity of  $A_g^2$  mode also appeared at the angle either perpendicular (F7,  $\sim 40$  nm) or par-



**Figure 1.16:** ARPRS with different excitation wavelengths performed on a 20-nm-thick BP sample on SiO<sub>2</sub> / Si substrate. Figure is reprinted from [18] with permission.

allel (F1,  $\sim 5$  nm) to the angle of the maximum  $A_g^1$  Raman intensity. They also indicated that without the explicit consideration of excitation wavelength and flake thickness, ARPRS could not be used to determine the CO as commonly used previously. However, they didn't investigate the thickness-dependent ARPRS results with the excitation wavelength of 442 nm.

Considering the strong thickness dependence of the ARPRS results of BP and the limited data in Kim et al's work [18], it is necessary to perform more ARPRS studies on BP with wider thickness range to confirm the effectiveness of the 442 nm laser in CO determination, and provide some theoretical explanations.



**Figure 1.17:** ARPRS with different excitation wavelengths performed on BP samples with various thickness on SiO<sub>2</sub> / Si substrate. Figure is reprinted from [19] with permission.



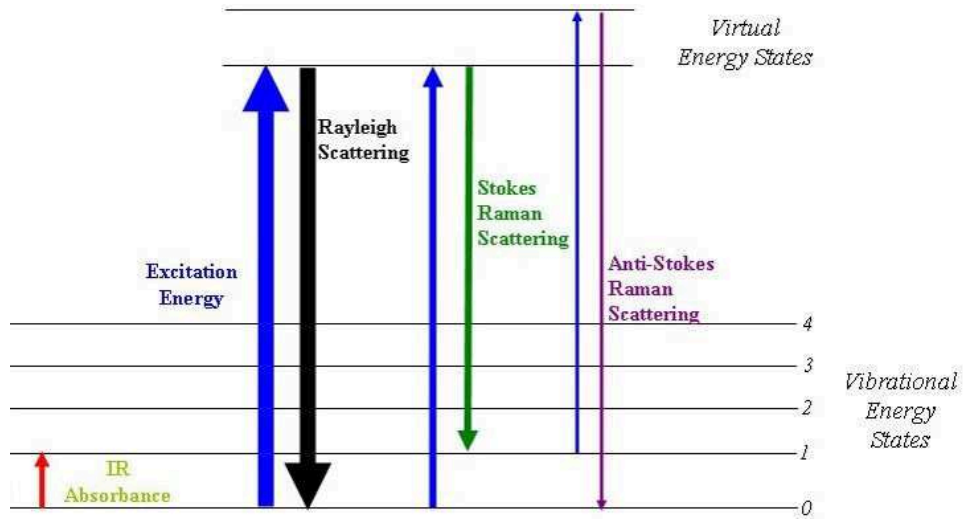
**Table 1.2:** The energy balance sheet for Raman process [2].

Initial state energy		Final state energy		Scattered frequency $\omega_s$ determined by energy conservation
Photons	molecule	Photons	molecule	
$n_1\hbar\omega_1$	$E_i$	$(n-1)\hbar\omega_1 + \hbar\omega_s$	$E_f = E_i + \hbar\omega_{fi}$	$\omega_s = \omega_1 - \omega_{fi}$

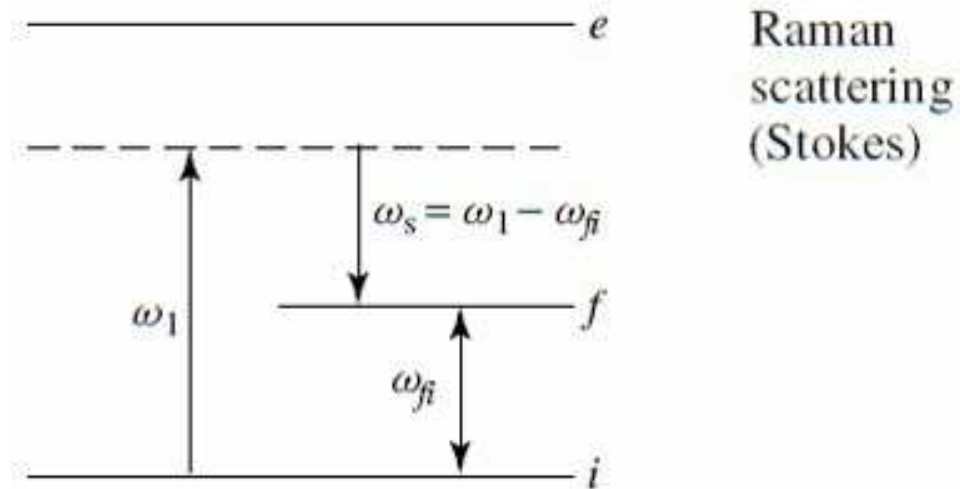
## 1.3 Basic Knowledge Of This Thesis Work

### 1.3.1 Basic Knowledge of Raman Scattering

Raman Spectroscopy is a very useful tool in studying 2D materials, and will be used extensively in this work. The Raman effect is an inelastic light scattering phenomenon first discovered by C. V. Raman [87]. Raman spectroscopy is increasingly becoming standard analytical techniques in academic and industrial studies. The whole process can be described as follows: with a laser light of specific wavelength comes into materials; then, most of the laser light is transmitted without any changes, some scattering happens because of the interactions between photons and atoms / molecules, which can be in either ground or excited rotational-vibrational states. As Fig 1.18 shows, the scattering without a change of frequency is called Rayleigh scattering, and that with change of frequency is called Raman scattering. The change of frequency gives information about the rotational and vibrational modes of the system. What's more, the final frequencies can be either  $\omega_1 - \omega_i$  or  $\omega_1 + \omega_i$  according to whether the original states are in ground or excited levels, which can be termed as the Stokes or anti-Stokes bands. In Table 2.1, the energy balance sheet of the Stokes band of Raman scattering following the conservation of energy is listed. Stokes Raman scattering is normally much stronger because most atoms / molecules of the systems are usually in ground states [88]. Therefore, in most cases, only the Stokes Raman scattering part will be illustrated in a typical Raman spectrum.



**Figure 1.18:** The energy-level diagram showing the states involved in Raman spectra. Figure is reprinted from Wikipedia under the GNU Free Documentation License.



**Figure 1.19:** The energy-level diagram of the Stokes band of Raman scattering. Figure is reprinted from [2] with permission.

As is shown in Fig 1.19, the normal Raman scattering process starts and ends at two explicit stationary states  $i$  and  $f$ . However the transition state  $m$  during the process doesn't have a well-defined value of energy, thus the absorption part has no energy conservation and is called virtual absorption. The intermediate state  $m$  is a virtual state [2]. Thus the energy-level diagram is just for simple illustration of electron-photon and electron-phonon interactions, and is not able to explain the complicated photon energies and energy states of the atom / molecule that are implicated in the scattering process. Raman Spectroscopy measures the phonon energies, which depend on many materials properties and conditions such as the bonding strength, crystallinity, temperature, strain, phase, etc. For a material with known chemical concentrations and a good crystallinity at room temperature and free of strain, its Raman spectra can be used to identify the allotrope of this material and corresponding phase.

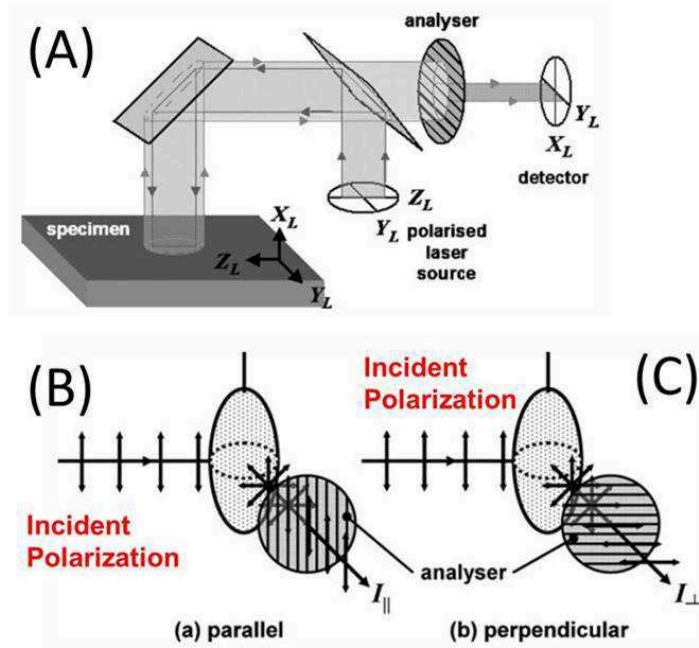
### 1.3.2 Basic Knowledge Of Polarized Raman Spectroscopy

In this thesis, the Raman system was configured with the backscattering geometry. Fig 1.20 (A) illustrate that: the incident light is linear polarized and the scattered light is circular-polarized after Raman scattering. By adding an analyzer with an angle parallel or perpendicular to the incident light polarization before the detector, only the scattered light with a polarization which is parallel (B) or perpendicular (C) to that of the incident light can be collected.

After discussing the Raman geometry and polarization, let us look at the intensity of the Raman-scattered light. In general, the Raman intensity of a specific Raman mode  $I$  can be described by the form [2]:

$$I \propto |\mathbf{e}_i \cdot \boldsymbol{\alpha}' \cdot \mathbf{e}_s|^2; \quad (1.1)$$

$\boldsymbol{\alpha}'$  is the Raman tensor of a given mode. In an X-Y-Z Cartesian coordinate system, the Raman tensor can be written as:



**Figure 1.20:** Figures (A) - (C) are reprinted from [20] with permission. (A): Illustration of the polarized Raman scattering light for the back scattering geometry. (B): Illustration of the polarization of the scattered light being “parallel” to that of the incident light. (C): Illustration of the polarization of the scattered light being “perpendicular” to that of the incident light.

$$[\alpha'] = \begin{pmatrix} \alpha'_{xx} & \alpha'_{xy} & \alpha'_{xz} \\ \alpha'_{yx} & \alpha'_{yy} & \alpha'_{yz} \\ \alpha'_{zx} & \alpha'_{zy} & \alpha'_{zz} \end{pmatrix} \quad (1.2)$$

For a single crystal, for each of the 32 crystal classes (symmetry point groups), the form of Raman tensors is summarized in Fig 1.21 [21]. What’s more, the unit vectors  $\mathbf{e}_i$  and  $\mathbf{e}_s$  are the light polarization vectors of the incident and scattered light, respectively. Therefore, with proper selected Raman geometries and polarization, the polarized Raman Spectroscopy can be used to study the Raman crystallography. Due to the scattered Raman intensity depends on the CO of the crystal under a specific configuration of the analyzer, ARPRS was developed to measure the Raman

System	Class	Raman tensors		
Monoclinic		$\begin{pmatrix} a & d \\ b & c \end{pmatrix}$	$\begin{pmatrix} e & f \\ f & f \end{pmatrix}$	
	2	$\mathcal{C}_2$	A(Y)      B(X, Z)	
	m	$\mathcal{C}_s$	A'(X, Z)    A''(Y)	
	2/m	$\mathcal{C}_{2h}$	A <sub>g</sub> B <sub>g</sub>	
Orthorhombic		$\begin{pmatrix} a & & \\ & d & \\ & & c \end{pmatrix}$	$\begin{pmatrix} & e \\ & & f \end{pmatrix}$	
	222	$\mathcal{D}_2$	A      B <sub>1</sub> (Z)      B <sub>2</sub> (Y)      B <sub>3</sub> (X)	
	mm2	$\mathcal{C}_{2v}$	A <sub>1</sub> (Z)    A <sub>2</sub> B <sub>1</sub> (X)      B <sub>2</sub> (Y)	
	mmm	$\mathcal{D}_{2h}$	A <sub>g</sub> B <sub>1g</sub> B <sub>2g</sub> B <sub>3g</sub>	
Trigonal		$\begin{pmatrix} a & & \\ & a & \\ & & b \end{pmatrix}$	$\begin{pmatrix} c & d & e \\ d & -c & f \\ c & f & \end{pmatrix}$	
	$\frac{3}{2}$	$\mathcal{C}_3$	A(Z)      E(X)      E(Y)	
	$\frac{3}{2}$	$\mathcal{C}_6$	A <sub>g</sub> E <sub>g</sub> E <sub>g</sub>	
			$\begin{pmatrix} a & & \\ & a & \\ & & b \end{pmatrix}$	$\begin{pmatrix} c & & \\ -c & d & \\ d & & \end{pmatrix}$
	32	$\mathcal{D}_3$	A <sub>1</sub> E(X)      E(Y)	
	3m	$\mathcal{C}_{3v}$	A <sub>1</sub> (Z)    E(Y)      E(-X)	
	$\bar{3}m$	$\mathcal{D}_{3d}$	A <sub>1g</sub> E <sub>g</sub> E <sub>g</sub>	

System	Class	Raman tensors	
Cubic		$\begin{pmatrix} a & & \\ & a & \\ & & a \end{pmatrix}$	$\begin{pmatrix} b & & \\ & b & \\ & & -2b \end{pmatrix}$
	23	$\mathcal{T}$	$\begin{pmatrix} -\sqrt{3}b & & \\ & \sqrt{3}b & \\ & & 0 \end{pmatrix}$
	m3	$\mathcal{T}_h$	$\begin{pmatrix} d & & \\ & d & \\ & & d \end{pmatrix}$
	432	$\mathcal{O}_h$	$\begin{pmatrix} d & & \\ & d & \\ & & d \end{pmatrix}$
	43m	$\mathcal{T}_d$	$\begin{pmatrix} d & & \\ & d & \\ & & d \end{pmatrix}$
m3m	$\mathcal{O}_h$	A <sub>1g</sub> E <sub>g</sub> E <sub>g</sub> F <sub>2g</sub> F <sub>2g</sub> F <sub>2g</sub>	A <sub>1g</sub> E <sub>g</sub> E <sub>g</sub> F <sub>2g</sub> F <sub>2g</sub> F <sub>2g</sub>

response of crystal at different orientations in order to determine its CO.

Tetragonal		$\begin{pmatrix} a & & & \\ & \ddot{a} & & \\ & & b & \\ & & & \end{pmatrix} \begin{pmatrix} c & d \\ d & -c \end{pmatrix} \begin{pmatrix} & e \\ e & f \end{pmatrix} \begin{pmatrix} & -f \\ -f & e \end{pmatrix}$
$\frac{4}{4}$	$\mathcal{C}_4$	A(Z)      B      E(X)      E(Y)
$\frac{4}{4}$	$\mathcal{C}_2$	A      B(Z)      E(X)      E(-Y)
4/m	$\mathcal{C}_{4h}$	A <sub>g</sub> B <sub>g</sub> E <sub>g</sub> E <sub>g</sub>
		$\begin{pmatrix} a & & & \\ & \ddot{a} & & \\ & & b & \\ & & & \end{pmatrix} \begin{pmatrix} c & \\ & -c \end{pmatrix} \begin{pmatrix} & d \\ d & \end{pmatrix} \begin{pmatrix} & e \\ e & \end{pmatrix} \begin{pmatrix} & e \\ e & \end{pmatrix}$
4mm	$\mathcal{C}_{4v}$	A <sub>1</sub> (Z)      B <sub>1</sub> B <sub>2</sub> E(X)      E(Y)
422	$\mathcal{C}_2$	A <sub>1</sub> B <sub>1</sub> B <sub>2</sub> E(X)      E(X)
42m	$\mathcal{C}_{2d}$	A <sub>1</sub> B <sub>1</sub> B <sub>2</sub> (Z)      E(Y)      E(X)
4/mmm	$\mathcal{C}_{4h}$	A <sub>1g</sub> B <sub>1g</sub> B <sub>2g</sub> E <sub>g</sub> E <sub>g</sub>
Hexagonal		$\begin{pmatrix} a & & & \\ & \ddot{a} & & \\ & & b & \\ & & & \end{pmatrix} \begin{pmatrix} c & \\ & d \end{pmatrix} \begin{pmatrix} & -d \\ -d & c \end{pmatrix} \begin{pmatrix} & e & f \\ e & f & -e \end{pmatrix} \begin{pmatrix} & f & -e \\ -e & -f & \end{pmatrix}$
$\frac{6}{6}$	$\mathcal{C}_6$	A(Z)      E <sub>1</sub> (X)      E <sub>1</sub> (Y)      E <sub>2</sub> E <sub>2</sub>
$\frac{6}{6}$	$\mathcal{C}_3$	A'      E''      E''      E'(X)      E'(Y)
6/m	$\mathcal{C}_{6h}$	A <sub>g</sub> E <sub>1g</sub> E <sub>1g</sub> E <sub>2g</sub> E <sub>2g</sub>
		$\begin{pmatrix} a & & & \\ & \ddot{a} & & \\ & & b & \\ & & & \end{pmatrix} \begin{pmatrix} c & \\ & c \end{pmatrix} \begin{pmatrix} & -c \\ -c & \end{pmatrix} \begin{pmatrix} & d \\ d & \end{pmatrix} \begin{pmatrix} & d \\ d & -d \end{pmatrix}$
622	$\mathcal{C}_6$	A <sub>1</sub> E <sub>1</sub> (X)      E <sub>1</sub> (Y)      E <sub>2</sub> E <sub>2</sub>
6mm	$\mathcal{C}_{6v}$	A <sub>1</sub> (Z)      E <sub>1</sub> (Y)      E <sub>1</sub> (-X)      E <sub>2</sub> E <sub>2</sub>
6m2	$\mathcal{C}_{3h}$	A <sub>1</sub> E''      E''      E'(X)      E'(Y)
6/mmm	$\mathcal{C}_{6h}$	A <sub>1g</sub> E <sub>1g</sub> E <sub>1g</sub> E <sub>2g</sub> E <sub>2g</sub>

**Figure 1.21:** Raman-active vibrational symmetries and Raman tensors for the crystal symmetry classes. Figure is reprinted from [21] with permission.

### 1.3.3 Basic Knowledge Of Phonon Modes Of Black Phosphorus

Black phosphorus has an orthorhombic ( $D_{2h}$ , Cmca, #64) structure, and its phonon modes can be expressed as [16]:

$$\Gamma = 2A_g + B_{1g} + B_{2g} + 2B_{3g} + A_{1u} + 2B_{1u} + 2B_{2u} + B_{3u} \quad (1.3)$$

The first 4 terms at the right side of Eq. 3.3 are the Raman active modes. From group theory [21], the Raman tensor for  $A_g$  modes of BP in the backscattering geometry is [89]:

$$\tilde{R}(A_g) = \begin{pmatrix} a & & \\ & b & \\ & & c \end{pmatrix} \quad (1.4)$$

$$\tilde{R}(B_{1g}) = \begin{pmatrix} & d & \\ d & & \\ & & \end{pmatrix} \quad (1.5)$$

$$\tilde{R}(B_{2g}) = \begin{pmatrix} & & e \\ & e & \\ & & \end{pmatrix} \quad (1.6)$$

$$\tilde{R}(B_{3g}) = \begin{pmatrix} & & & \\ & & f & \\ & & & \\ & f & & \end{pmatrix} \quad (1.7)$$

Here a, b, c, d and f are Raman tensor elements [19][89], in which:

$$a = |a|e^{i\phi a} = \frac{\partial \varepsilon_{xx}}{\partial q^{A_g}} = \frac{\partial \varepsilon'_{xx}}{\partial q^{A_g}} + \frac{\partial \varepsilon''_{xx}}{\partial q^{A_g}} \quad (1.8)$$

$$b = |b|e^{i\phi b} = \frac{\partial \varepsilon_{yy}}{\partial q^{A_g}} = \frac{\partial \varepsilon'_{yy}}{\partial q^{A_g}} + \frac{\partial \varepsilon''_{yy}}{\partial q^{A_g}} \quad (1.9)$$

$$c = |c|e^{i\phi c} = \frac{\partial \varepsilon_{zz}}{\partial q^{A_g}} = \frac{\partial \varepsilon'_{zz}}{\partial q^{A_g}} + \frac{\partial \varepsilon''_{zz}}{\partial q^{A_g}} \quad (1.10)$$

$$f = |f|e^{i\phi f} = \frac{\partial \epsilon_{xz}}{\partial q^{B_{2g}}} = \frac{\partial \epsilon'_{xz}}{\partial q^{B_{2g}}} + \frac{\partial \epsilon''_{xz}}{\partial q^{B_{2g}}} \quad (1.11)$$

Here the  $\epsilon'_{ii}$  and  $\epsilon''_{ii}$  (i=x, y, z) are the real and imaginary parts of the dielectric constant along different crystalline orientations (armchair and zigzag directions), and  $q^{A_g}$  and  $q^{B_{2g}}$  are the normal coordinates of the Raman modes. The complex values of the Raman tensor elements are due to the light absorption of BP. Due to the back-scattering configuration, the direction of incident laser is perpendicular to the stacked layer plane of the sample, so that  $B_{1g}$  and  $B_{3g}$  modes are forbidden and  $A_g$  and  $B_{2g}$  modes can be observed during Raman measurements.

After that, according to the interpretation of crystallography of BP shown in Fig 1.21, the Raman tensors can be then expressed as:

$$\tilde{R}(A_g) = \begin{pmatrix} a\sin^2\theta + c\cos^2\theta & 0 & \frac{1}{2}(a-c)\sin 2\theta \\ 0 & b & 0 \\ \frac{1}{2}(a-c)\sin 2\theta & 0 & a\cos^2\theta + c\sin^2\theta \end{pmatrix} \quad (1.12)$$

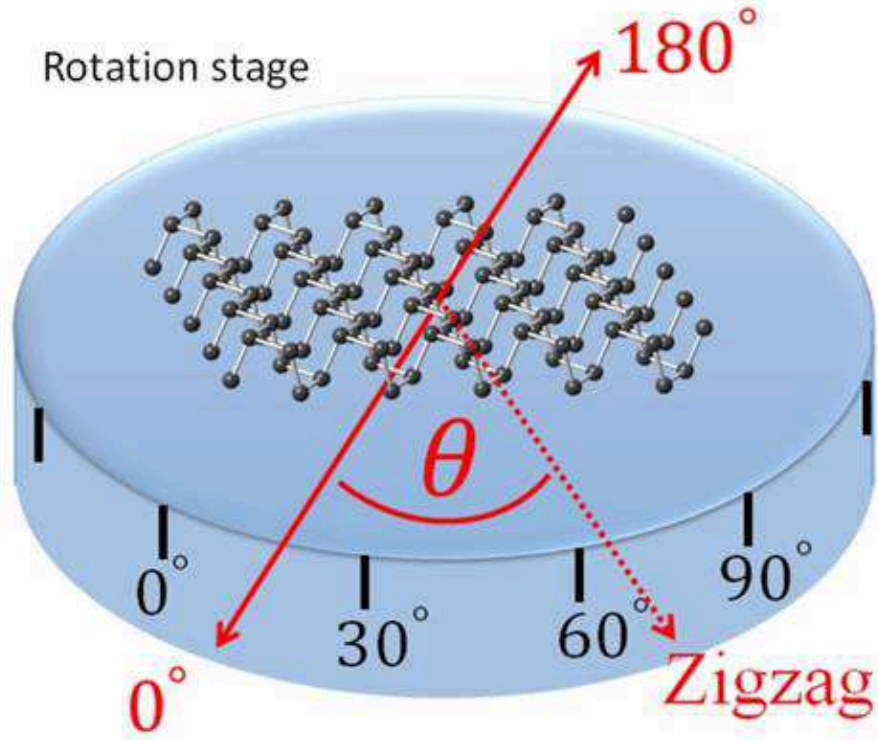
$$\tilde{R}(B_{2g}) = \begin{pmatrix} -e\sin 2\theta & 0 & e\cos 2\theta \\ 0 & b & 0 \\ e\cos 2\theta & 0 & e\sin 2\theta \end{pmatrix} \quad (1.13)$$

In addition,  $\mathbf{e}_i$  and  $\mathbf{e}_s$  in Eq. 3.1 can be written as:

$$\mathbf{e}_i = \mathbf{e}_s = (\sin\theta, 0, \cos\theta);$$

As demonstrated in Fig 1.22, the  $\theta$  here is defined as the angle between the zigzag direction and the polarization  $\mathbf{e}_i$  of the incident light (here the polarization of the incident light is defined at  $0^\circ$  and  $180^\circ$ ). Moreover, in Table 3.1, the generalized form of Raman intensities of  $A_g$  and  $B_{2g}$  modes under “parallel” configuration are shown in Table 3.1. Here the term “Parallel” direction means: the scattered light is parallel to the incident laser because of the polarization by the inserted analyzer [90]. When  $\theta = 0^\circ$  or  $180^\circ$ , in other words, the incident light is parallel to zigzag direction of BP,  $I_{A_g, 0^\circ/180^\circ}^{\parallel} = a^2$  and  $I_{B_{2g}}^{\parallel} = 0$ ; When  $\theta = 90^\circ$  or  $270^\circ$ , namely the in-





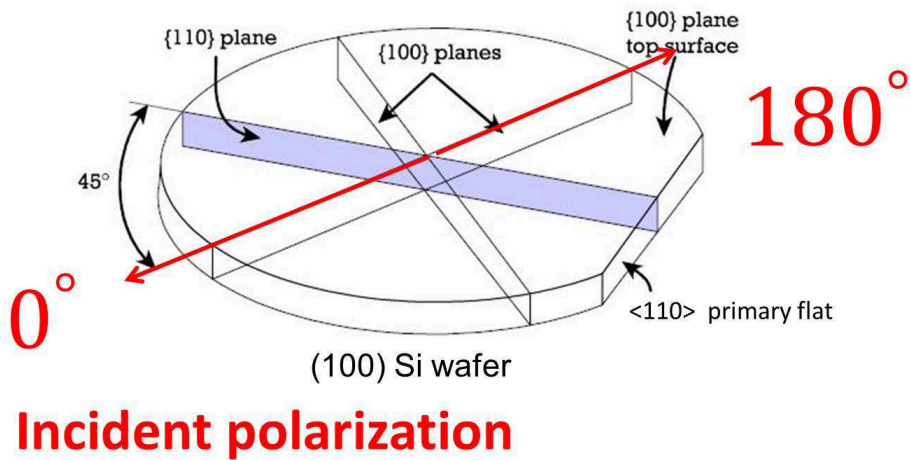
**Figure 1.22:** Illustration of the “ $\theta$ ” angle, the “zigzag” direction of the BP sample and the reading angle “ $\alpha$ ” of the rotation stage. The red arrows indicate the polarization of the incident laser.

incident light is parallel to the armchair direction of BP,  $I_{A_g, 90^\circ/270^\circ}^{\parallel} = c^2$  and  $I_{B_{2g}}^{\parallel} = 0$ . Therefore, Raman intensities of  $A_g$  and  $B_{2g}$  modes under “parallel” configuration have periodicities of  $180^\circ$  and  $90^\circ$ , respectively. In addition, when incident laser is parallel to either zigzag or armchair direction,  $B_{2g}$  mode is always forbidden.

Therefore, with a specific excitation wavelength and for all thickness range, if  $\frac{I_{A_g, 0^\circ/180^\circ}^{\parallel}}{I_{A_g, 90^\circ/270^\circ}^{\parallel}} \gg 1$  or  $\ll 1$ , then ARPRS can provide unambiguous determination of the CO of BP.

**Table 1.3:** Raman intensity of BP  $A_g$  and  $B_{2g}$  modes under “parallel” configuration.

$A_g$ mode	$B_{2g}$ mode
$(a\cos^2\theta + c\sin^2\theta)^2$	$e^2\sin^22\theta$

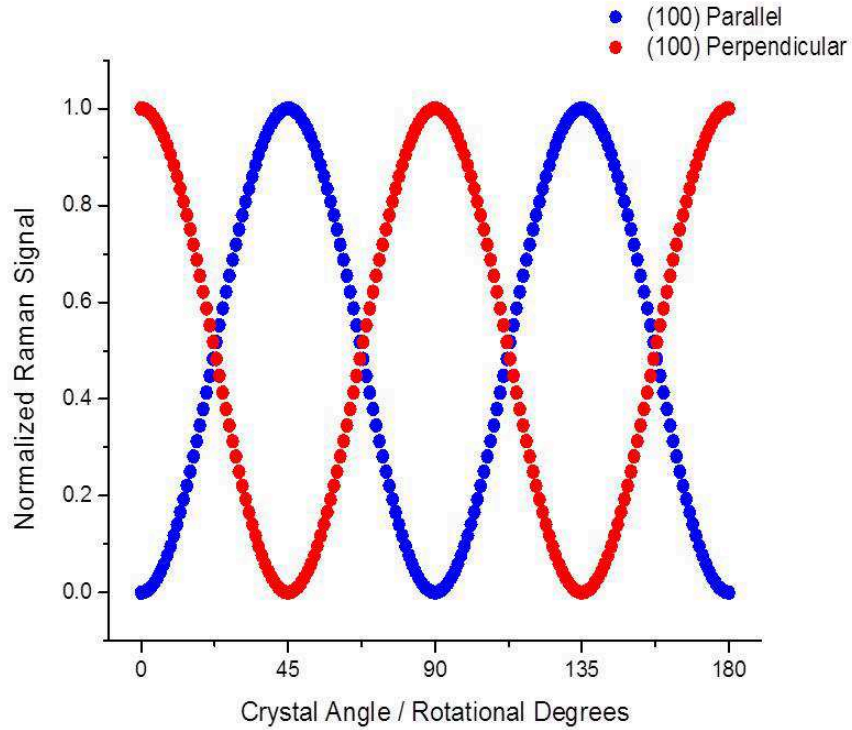


**Figure 1.23:** Illustration of Si (100) substrate.

### 1.3.4 Crystallographic Orientation Of Si (100) Wafer And Its Orientation Dependent Raman Response

Like BP, the Raman intensity of Si (100) substrate also changes periodically with its CO and the laser polarization [91][92]. For instance, under parallel configuration, when the incident polarization is parallel to Si  $\{100\}$  planes (see Fig 1.23), the Si Raman mode has a maximum / minimum Raman intensity [92].

For example, Fig 1.24 illustrates the ARPRS results on a Si (100) wafer under the “parallel” and “cross” configuration. Under both configurations, the Raman intensity of the Si (100) wafer shows a sinusoidal function of the rotation angle “ $\alpha$ ” (the reading from the rotation stage) with a periodicity of  $90^\circ$ .



**Figure 1.24:** The ARPRS results of the polarized Raman measurements of a Si (100) wafer measured under the “parallel” and “cross” configuration. Image courtesy of David Tuschel, Horiba Scientific, USA.

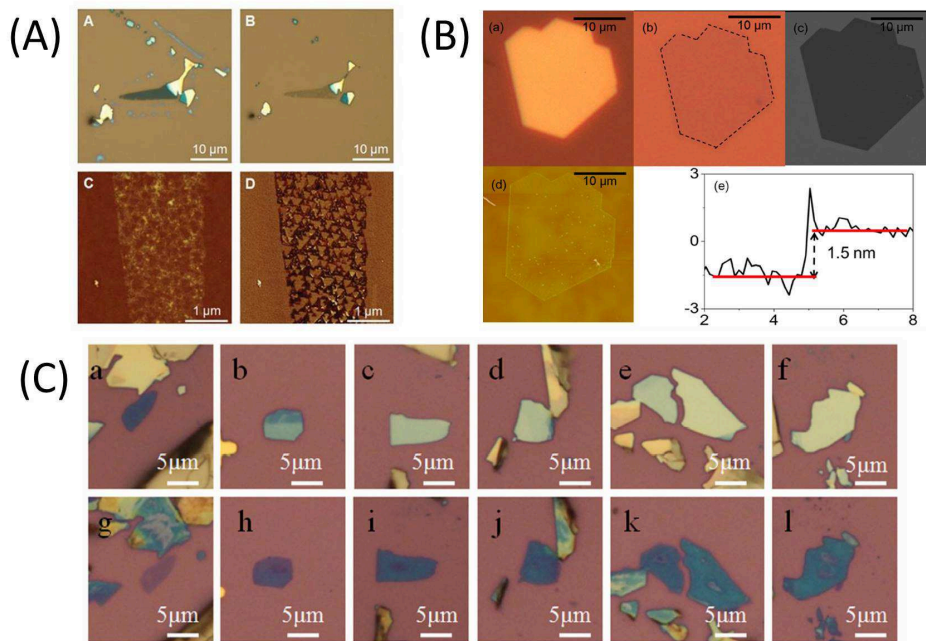
### 1.3.5 Thickness Determination By The N-dependent Raman Intensity Ratio Of $\frac{I_{Si}}{I_{2DM}}$

It is important to note that, Raman spectroscopy can also serve as a fast and non-destructive method in identifying thickness ( or the layer number N ) of 2D material flakes [93]. SiO<sub>2</sub> / Si (Si (100) wafer with an oxide layer) has been widely used as the substrates of 2D materials. For instance, Li et al. [94] reported the determination of the layer number of graphene up to 100 layers according to the Raman peak intensity ratio of  $\frac{I(G)}{I(Si)}$ ; similarly, the layer number of MoS<sub>2</sub> can also be determined by  $\frac{I(E_{2g}^1)}{I(Si)}$  and  $\frac{I(A_{1g})}{I(Si)}$  [95].

So far, for black phosphorus,  $\frac{I_{A_g^1}}{I_{Si}}$  [46] and  $\frac{I_{Si}}{I_{A_g^2}}$  [12] as functions of layer numbers N have been reported. However, because of the orientation-dependent Raman response of BP, the CO of the BP sample needs to be known first for this method to work. In this work, the investigations of the one-to-one relationship between the thickness (the layer number N) and the Raman intensity ratios of  $\frac{I_{Si}}{I_{A_g^2}}$  were presented.

### 1.3.6 Thermal Sublimation For Preparation Of Few-layer 2D Materials

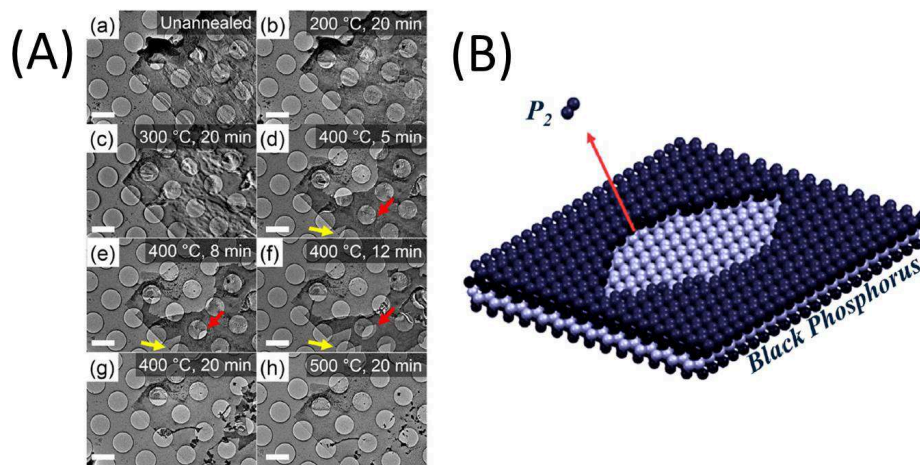
So far, very few studies on the successful fabrication of few-layer 2D materials via thermal thinning were reported. In Fig 1.25 (A), the exfoliated 2 to 4 -layer MoS<sub>2</sub> flakes were reported [22][96] to be reduced to single-layer via thermal thinning method at 330 °C; in Fig 1.25 (B), Huang et al. [23] reported that single and bilayer Sb<sub>2</sub>Te<sub>3</sub> and Bi<sub>2</sub>Se<sub>3</sub> flakes with lateral dimensions exceeding 10 μm could be prepared from thick flakes by performing thermal thinning at 490 °C and 510 °C respectively; in Fig 1.25 (C), the thermal thinning study of WSe<sub>2</sub> from a recent work [24] was shown, which demonstrated that the surface defects of a pristine sample could degenerate the quality of final products. Therefore, thermal thinning has been studied as an effective method for reducing bulk 2D materials into a few layers. However, so far no studies have been reported using sublimation as a top-down thinning method to prepare few-layer black phosphorus.



**Figure 1.25:** (A): Sublimation thinning of a MoS<sub>2</sub> flake: mechanically exfoliated bilayer MoS<sub>2</sub> flake was thinned to single layer after annealed at 330 °C for 15 h. (Figure is reprinted from [22] with permission); (B) sublimation thinning of Bi<sub>2</sub>Se<sub>3</sub>: Bi<sub>2</sub>Se<sub>3</sub> plates prepared by deposition with an original thickness of 3.5 μm was heated at 510 °C for 10 minutes. (Figure is reprinted from [23] with permission); (C): sublimation thinning of WS<sub>2</sub>: mechanically exfoliated WS<sub>2</sub> flakes listed in the upper row were held at 600 °C for 45 minutes, and the Ar gas with a flow rate of 300 cc / min was purged in to protect the sample. At last, the figures in the lower row demonstrated that those flakes were thinned down to 8 to 45 nm from left to right. Figure is reprinted from [24] with permission.

### 1.3.7 Previous Studies On Thermal Decomposition And Sublimation Of Black Phosphorus

According to our best knowledge, only 2 studies reported thermal decomposition and sublimation of black phosphorus. In 2015, by using in-situ transmission electron microscopy (TEM), Liu et al. [25] first observed sublimation of BP at 400 °C (See Fig 1.26 (A)) starting at flake edges and defects, and then forming eye-shaped cracks along  $\langle 001 \rangle$  directions. Su et al. [97] also observed the decomposition and sublimation of BP at 350°C. In 2016, another work [26] indicated that the sublimation of BP took place at 375°C and the process involved detachments of pairs of P atoms (See Fig 1.26 (B)) by using low energy electron diffraction (LEED).



**Figure 1.26:** (A): Observation of decomposition of BP at 400 °C by using transmission electron microscopy (TEM) (Figure is reprinted from [25] with permission); (B): the illustration of the decomposition mechanism of BP: detachments with phosphorus dimers (Figure is reprinted from [26] with permission).

## **1.4 Problem Definition And Thesis Goal**

First, so far none of the 6 available fabrication methods for few-layer BP thin film fabrication could satisfy all the 5 critical requirements: scalability, uniformity, crystallinity, thickness controllability and economic fabrication.

It is a must to develop a new fabrication method which would meet those essential requirements. To date, thermal thinning has been extensively used for thinning down thick 2D material flake to a few layers, and so far no works have been reported on successful thinning of BP. Therefore, two major objectives have been proposed in this work on thermal thinning of BP:

1. The thermal thinning method should be capable of reducing thick BP flakes to a few layers with good crystallinity, uniformity and scalability.

2. The final thickness of BP products should be tunable, in other words, the thermal thinning process should be controllable.

Second, up to now, ARPRS has not been confirmed as an effective method in BP CO determination because of the complicated thickness and wavelength - dependent ( wavelength  $> 442$  nm) ARPRS response. In the other side, limited data from previous report were also insufficient to confirm ARPRS with 442 nm excitation to be effective for CO determination. Therefore, the third major objective has been proposed in this work on BP CO determination by ARPRS with 442 nm excitation:

3. Investigations should be conducted on more samples to confirm there is no thickness-dependency of ARPRS results.

## **1.5 Scope Of The Thesis**

In this thesis, optical microscopy, atomic force microscopy (AFM) and Raman spectroscopy were used to study layer-by-layer thermal sublimation of black

phosphorus. AFM and Raman mapping measurements indicated the repeatable and successful preparation of few-layer black phosphorus. Through the interrupted and continuous heating study of BP, the thinning rates of BP at 500 K and 550 K were measured.

The effectiveness of ARPRS with 442 nm excitation in fast and non-destructive determination of BP CO was confirmed by investigating the ARPRS results of 27 BP samples on 2 different substrates. After that, an in-situ Raman method in monitoring thickness was realized by using the thickness ( the layer number N ) -dependent Raman peak intensity ratio of I(Si) over I(A<sub>g</sub><sup>2</sup>):  $\frac{I_{Si}}{I_{A_g^2}}$ .

In general, the scope of this thesis work can be demonstrated that:

1. Thermal thinning method can used for controllably preparing large scale, uniform and crystalline few-layer BP.
2. Raman spectroscopy could be used as a versatile tool to determine the crystallographic orientation, thickness, uniformity and crystallinity of BP.

## 1.6 The Organization Of This Thesis

After this chapter of introduction, in Chapter 2, the thermal sublimation of BP was studied in this work. This is the first work to use the thermal sublimation thinning to controllably prepare large, crystalline few-layer BP. The experiments of sublimation thinning of BP were presented: BP flakes were heated at high temperatures and color changes of samples were recorded; AFM measured the changes of thickness; spatial Raman mapping measurements were directed on samples before and after several thinning processes, and the results indicated the integrity, uniformity and crystallinity of BP sample remained. After that, by performing interrupted and continuous heating, the sublimation rates of BP were measured to be 0.2 nm /min at 500 K and 1.5 nm / min at 550 K from AFM results. At last, by using AFM, optical contrast and Raman mapping, the successful and repeatable preparation of



large and crystalline few-layer black phosphorus via the simple sublimation thinning method were demonstrated.

In Chapter 3, the experiments of Raman study on BP samples with thicknesses ranging from 10 to 200 nm on SiO<sub>2</sub> / Si and polyimide substrates were presented: the orientation-dependent Raman responses of 11 BP flakes on Si substrates were studied by angle-resolved polarized Raman spectroscopy (ARPRS). The results revealed that, with the excitation wavelength of **442** nm and under **parallel** configuration, the maximum and minimum Raman peak intensities of A<sub>g</sub><sup>1</sup> and A<sub>g</sub><sup>2</sup> modes are orthogonal; in addition, when the maximum Raman intensity of A<sub>g</sub><sup>2</sup> mode appears, it will be always 10 - 100 times greater than its minimum Raman intensity at ± 90° orthogonal to its current position. Such unambiguous Raman responses didn't appear in previous ARPRS studies using other excitation wavelengths. Therefore, ARPRS with the excitation wavelength of **442** nm and under **parallel** configuration were confirmed to unambiguously determine the CO of BP. After that, it was demonstrated that, with a BP flake rotated to generate maximum A<sub>g</sub><sup>1</sup> Raman intensity, a one-to-one relationship between the Raman intensity ratio of  $\frac{I_{Si}}{I_{A_g^2}}$  and BP thickness could be established. What's more, the  $\frac{I_{Si}}{I_{A_g^2}}$  increases with decreasing thickness monotonically. Therefore, first developed in this work, this all-Raman method provided the CO identification as well as the capability of in-situ determining the thickness of BP.

In summary, Chapter 4 summarizes the results of this work and suggests that the sublimation thinning method is a promising method of preparing few-layer BP and the Raman spectroscopy is a powerful tool in determining the CO, thickness and crystallinity of BP prepared by thermal thinning method. Potential directions for future work are also proposed.

## Chapter 2

# Thermal Sublimation of Black Phosphorus

*“Everything should be made as simple as possible, but not simpler.”*

— Albert Einstein

### 2.1 General Procedure Of The Experimental Work Of This Chapter

In this section, uniform layer-by-layer sublimation of the black phosphorus at  $\leq 600$  K ( $\sim 330$  °C) were reported.

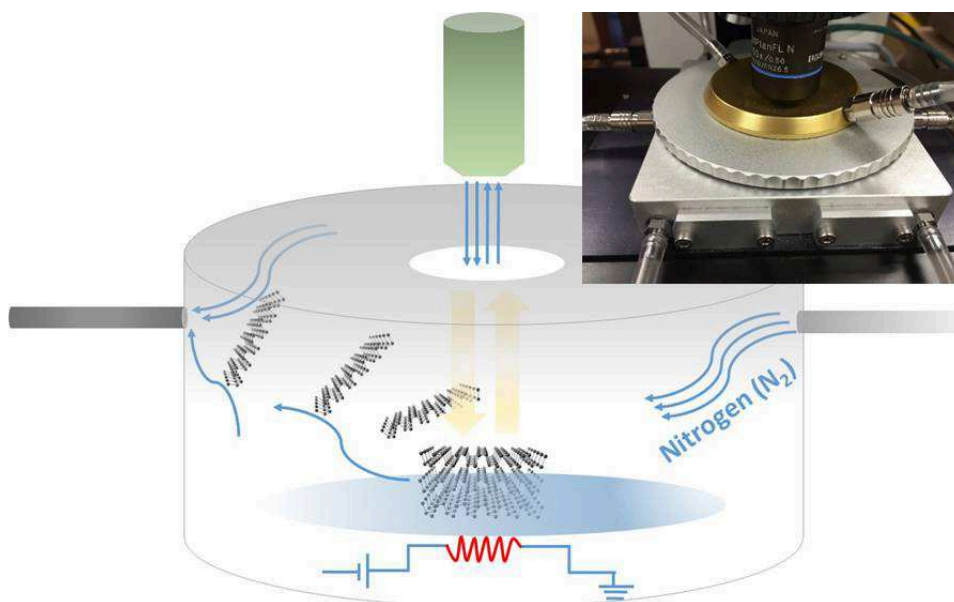
Raman imaging confirmed the uniformity and crystallinity of the BP samples after processing. The sublimation rates of BP were demonstrated to be 0.18 nm / min at 500 K ( $\sim 230$  °C) and 1.5 nm / min at 550 K ( $\sim 280$  °C). Moreover, the successful and repeatable preparation of large and few-layer crystalline BP indicated the thermal sublimation could be used as a simple method for controllably preparing crystalline few-layer BP.

### 2.1.1 Thermal Sublimation

The BP flakes were mechanically exfoliated from bulk BP crystals (99.998 %, Smart Elements, Vienna, Austria) in a glove box using Nitto SPV 224 R tape and transferred to a Si (100) wafer (4 inch, 0.56 mm thick) with a 300-nm-thick thermally-grown SiO<sub>2</sub> layer) or a polyimide substrate. Ultrasonication in acetone and rinsing process in deionized water were performed to pre-clean this wafer/polyimide. The wafer was then cut into small pieces ( $\sim 4 \text{ mm} \times 4 \text{ mm}$ ) by a glass cutter. After that, a small piece of wafer was loaded into a Linkam TS1200 heating stage. The heating stage was then mounted on the motorized XY stage of a Horiba Scientific LabRAM HR800 con-focal Raman microscope. After closing the lid, the valves on both sides of the heating stage (see Fig 2.1) were opened to purge the high purity nitrogen gas (Praxair, industrial grade, purity: 99.995%) flowing continuously through the heating stage. This step was in order to exhaust the air in the heating stage and build up an inert environment for following heating process. After purging N<sub>2</sub> gas for 30 minutes, a programmed isothermal joule heating process was performed on the wafer placed on a sapphire plate in the chamber of the heating stage with nitrogen gas flowing through the chamber. The ramping-up and cooling-down rates were both programmed at 100 K / min. The continuous N<sub>2</sub> flow would be kept until the sample was taken out for AFM measurements.

### 2.1.2 Raman Measurement

In section 2.4.1 to 2.4.3, all Raman measurements were performed with a Horiba LabRam HR800 Raman system in a backscattering configuration with 441.6 nm excitation. The Raman system has two modes: video and Raman. the video mode was used to record the optical images. The background light source for the video mode was provided by an integrated EUROMEX<sup>TM</sup> ILLUMINATOR EK-5 light, and the degree of light for all optical observations in this thesis was fixed at “5”. The Raman spectra were collected through an Olympus 50X (NA = 0.55) objective lens and recorded with the grating of 2400 lines mm<sup>-1</sup> which has a spectral resolution of 0.27 cm<sup>-1</sup>. When performing Raman measurement at 500 K / 550 K, the laser power was reduced to be less than 0.2 mW/ $\mu\text{m}^2$  by adding a filter in



**Figure 2.1:** Illustration of the sublimation process of BP.

order to minimize the laser heating effect. The acquisition time and accumulation times were optimized to be 6 sec and 2 times, respectively, in order to get a signal-to-noise ratio of 100 approximately as well as to avoid long time laser damage to BP samples.

Furthermore, in this section, all two-dimensional Raman mapping images were acquired using the following configurations: the increments of X and Y direction were 1.6 and 1.5  $\mu\text{m}$  /step, respectively. It is worth mentioning that, the laser spot size was  $\sim 2 \mu\text{m}^2$ . In addition, during Raman mapping measurements, all BP flakes were still kept in the heating stage protected in the inert environment of high purity nitrogen gas.

In section 2.4.3, all Raman measurements were performed with a Horiba LabRam HR800 Raman system in a backscattering configuration with 632.8 nm excitation. The Raman spectra were collected through an Olympus 50X (NA = 0.55) objective lens and recorded with the grating of 600 lines  $\text{mm}^{-1}$  which has

a spectral resolution of  $0.63 \text{ cm}^{-1}$ . The acquisition time and accumulation times were optimized with 3 sec and 2 times, respectively. Moreover, in this section, all two-dimensional Raman mapping images were acquired using the following configurations: the increments of X and Y direction were 1.2 and 1.1  $\mu\text{m}$  /step, respectively. During the Raman mapping measurements, all BP flakes were placed in the heating stage with high purity nitrogen gas purging in to avoid oxidation.

### **2.1.3 Determination Of The Crystallographic Orientations (CO) Of BP And underlying Si (100) Substrate**

The 441.6 nm laser beam was polarized, and an analyzer was placed in the parallel configuration before the entrance of spectrometer in the same manner as previous studies [18][19][98]. BP samples were placed on a rotation stage and rotated  $180^\circ$  about the microscope optical axis in 12 steps (  $15^\circ$  / step ). Considering the periodicity of  $A_g^1$  and  $A_g^2$  modes were  $180^\circ$ , and the maximum Raman intensity of  $A_g^1$  and  $A_g^2$  modes were orthogonal, the maximum Raman intensity of  $A_g^1$  or  $A_g^2$  mode could be easily measured with rotating only  $90^\circ$  ( 6 steps ). In this work, the sample was rotated at an angle with the maximum Raman intensity of  $A_g^1$  mode. What's more, since the rotation angle acquired from the previous 6-step operation might still differ from the real angle with the maximum Raman intensity of  $A_g^1$  mode, half-interval search method was used for further refinement of rotation angle. Similar operations were directed for underlying Si (100) wafer to find the maximum and minimum Si Raman intensity. In addition, during every step, the laser spot was focused at the same point on the sample to ensure the consistency of results.

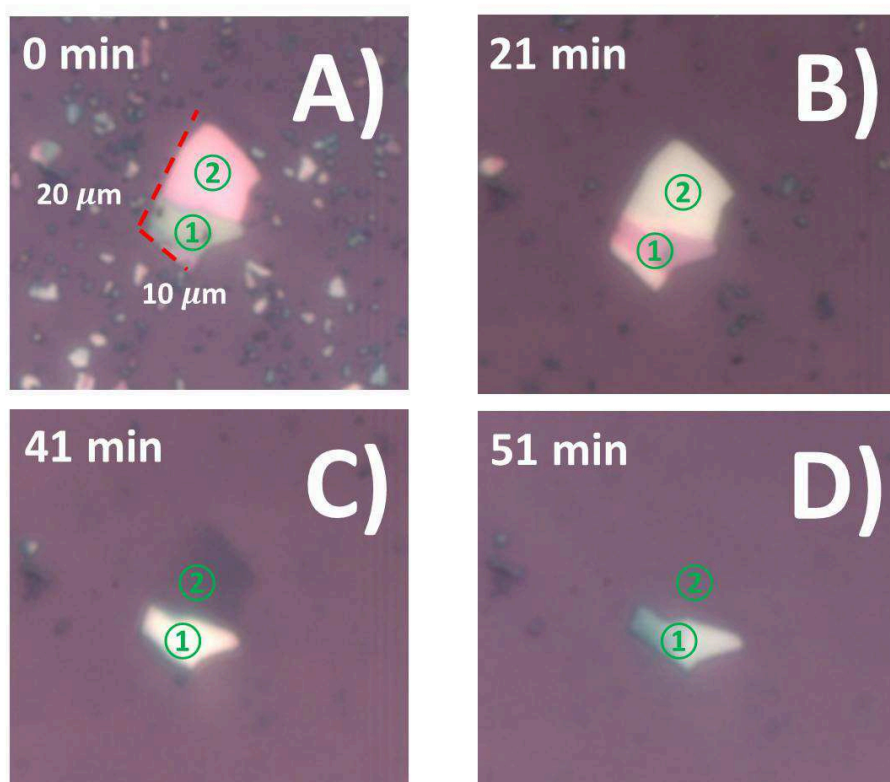
### **2.1.4 Atomic Force Microscopy (AFM)**

AFM measurements were performed in contact mode by an Asylum Research Molecular Force Probe 3D atomic force microscope and a Bruker Atomic Force Microscopy System. Samples were stored in an enclosed container with desiccants before transferring to AFM measurements in order to minimize the oxidation.

## 2.2 Results And Discussions

### 2.2.1 Investigations Of Thermal Sublimation And Its Mechanism

#### 2.2.1.1 Sublimation of BP At 600 K: Uniform Color Changes With No Observable Cracks



**Figure 2.2:** (A) - (D): Observation of the layer-layer-layer sublimation process of BP at 600 K. The different colors in the area 1 and area 2 indicated different thicknesses.

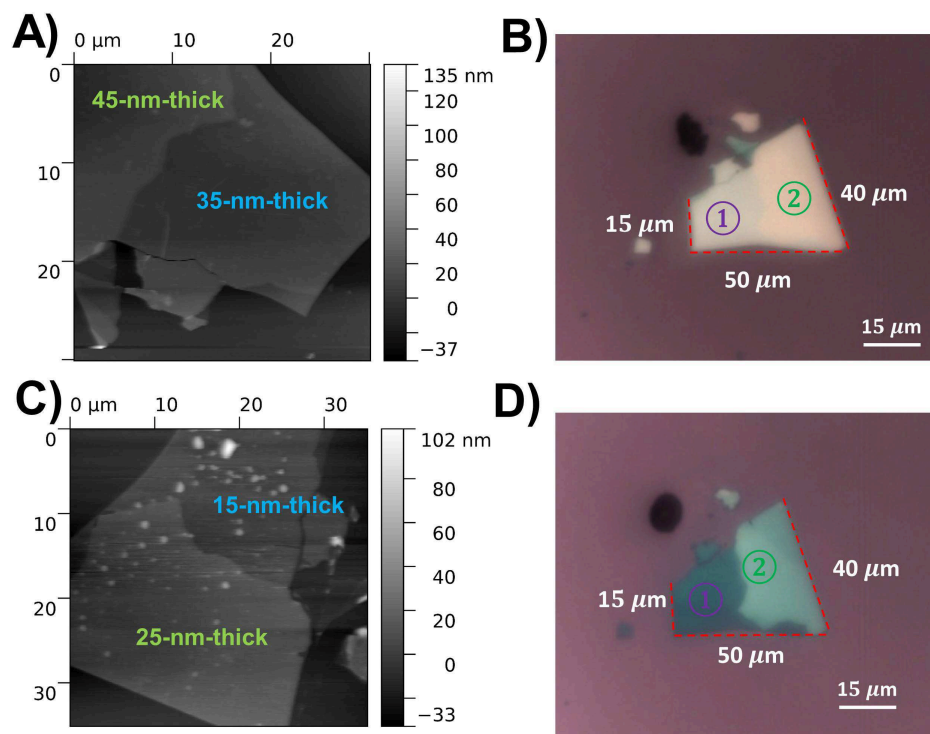
First, uniform color changes with no area shrinkages observed during the isothermal joule heating under the protection of high purity nitrogen gas was re-

ported. Fig 2.2 (A)–(D) show the optical images of a BP sample on SiO<sub>2</sub> / Si substrate at four different times during 600 K heating from 0 to 51 minutes.

Obvious changes of color, which are directly related to the thickness, were observed during the isothermal heating. Fig 2.2 (A) - (D) showed optical images of BP Sample A at four different times during 600 K heating from 0 to 51 mins. 0 min indicated the time point where the temperature just reached the isothermal holding temperature. In Fig 2.2 (A), the pink zone (area 2) was thinner than the green zone (area 1). Fig 2.2 (B) showed area 1 turned to red and area 2 to peach after heating for 21 minutes. In Fig 2.2 (C), area 2 turned to gray at 41 minutes, which was the characteristic color of few-layer BP as reported previously [46][12]. In Fig 2.2 (D), at 51 minutes, area 2 was fully disappeared. In addition, no micron-scale area shrinkages were observed during the whole heating process. The colors of each region were uniformly changed, which suggested that the sublimation process was uniform and happened layer by layer.

#### **2.2.1.2 Sublimation Of BP At 500 K: AFM Study**

To capture the thickness changes, a large trapezoid thick BP flake, with an area over 1,200  $\mu\text{m}^2$ , was heated at 500 K for 195 minutes. AFM measurements were performed immediately before and after the heating to acquire the thickness and morphology and to avoid sample degradation in the air. In Fig 2.3 (A) and (B), the morphology and thickness results of the original sample before heating, showed two regions with different colors (light green for Zone 1 and peach for Zone 2) and thickness (35 and 45 nm for Zone 1 and 2 respectively). Fig 2.3 (C) and (D) showed the thickness of the sample after heating was reduced to 15 and 25 nm for Zone 1 and 2 respectively. Therefore, both Zone 1 and Zone 2 were thermally reduced by the same thickness of 20 nm, and the step height between them remained unchanged after the heating process. This can be explained by that the sublimation of Zone 1 took place along the edges which is the step. Therefore, the thickness measurements by AFM confirmed that the BP flake underwent an layer-by-layer uniform sublimation, and the sublimation rate didn't depend on the original thick-



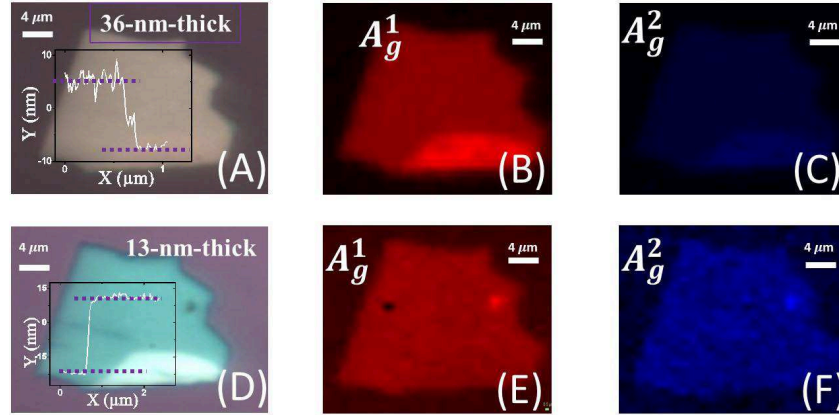
**Figure 2.3:** AFM and optical images of a trapezoid BP sample. (A) and (B): before heating; (C) and (D): after heating in nitrogen at 550 K for 195 mins. The dispersed white pits on the sample surface were attributed to the fast surface reactions with oxygen and moisture in the air [21] during sample transportation to the AFM and during the AFM measurements in the air. The red dashed lines indicated the edges of the samples and the numbers next to them are edge dimensions.

ness. No obvious cracks were found on the sample in all the above experiments.

### 2.2.1.3 Sublimation Of BP At 500 K And 550 K: AFM And 2D Raman Mapping

Additionally, in Fig 2.4 and 2.5, high temperature heating on 2 BP flakes were performed at 500 and 550 K, respectively. Spatial Raman maps and thickness measurements by atomic force microscopy (AFM) of both BP flakes were taken



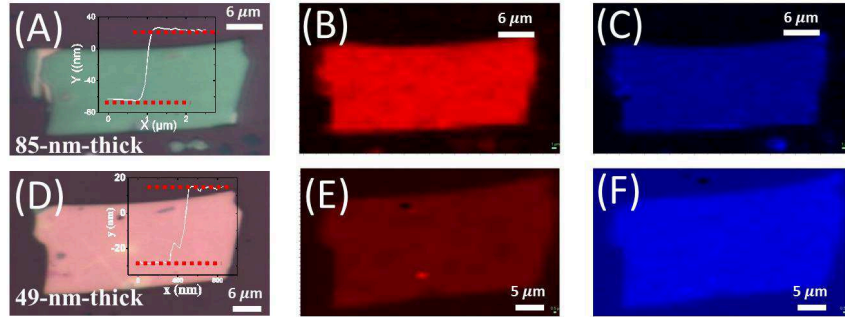


**Figure 2.4:** (A):the optical image of this BP flake before 500 K heating process, and the inset AFM line-scan profile indicated its thickness to be 36 nm; (B) - (C): Spatial Raman maps of  $A_g^1$  and  $A_g^2$  peak intensity acquired on a 36-nm-thick BP flake; (D): the optical image of this BP flake after 500 K heating process for 120 minutes, , and the inset AFM line-scan profile indicated its thickness to be 13 nm; (E) - (F): Raman images ( $A_g^1$  and  $A_g^2$  modes) of this BP flake after 500 K heating process;

before and after high temperature heating. Fig 2.4 (A) and (D) showed a 36-nm-thick BP flake was reduced to 13-nm-thick after heating at 500 K for 120 minutes.

In comparison with Raman maps of  $A_g^1$  and  $A_g^2$  modes of the pristine BP flake shown in the Fig 2.4 (B) and (C), those shown in Fig 2.4 (E) and (F) indicated that, these Raman peak intensities were uniform across the sample, showing that the BP sample kept its integrity and uniformity after the heating process, which confirmed the layer-by-layer sublimation of BP.

Similarly, the comparison between Fig 2.5 (A)-(C) and Fig 2.5 (D)-(F) of another flake also indicated that the layer-by-layer sublimation of heating process operated at 550 K for 25 minutes. Moreover, since the conditions of the background light for all images taken in this work were consistent (see methods in Section 2.1.1 in P 46), the color changes with different thickness can be attributed to the light wave interference effect between the incident, transmitted and reflected light.



**Figure 2.5:** (A): the optical image of this BP flake before 550 K heating process, and the inset AFM line-scan profile indicated its thickness to be 85 nm; (B) - (C): Spatial Raman maps of  $A_g^1$  and  $A_g^2$  peak intensity acquired on an 85-nm-thick BP flake; (D): the optical image of this BP flake after 550 K heating process for 25 minutes, and the inset AFM line-scan profile indicated its thickness to be 49 nm; (E) - (F): Raman images ( $A_g^1$  and  $A_g^2$  modes) of this BP flake after 550 K heating process;

#### 2.2.1.4 Thermal Thinning Of BP At More Temperatures

In contrary, previous studies [25][97][26] all reported that the sublimation and decomposition of BP were above 350 °C (623 K), which was more than 50 °C higher than the temperatures studied here. In Liu. et al's [25] work, they performed transmission electron microscopy (TEM) observation after heating for less than 20 minutes and in another work [26], real-time observations at different high temperatures by low energy electron microscopy (LEEM) on a heating ramp with less than 20 seconds were performed. Both of the two previous works didn't investigate the relative long term thermal stability of BP at the temperatures they studied.

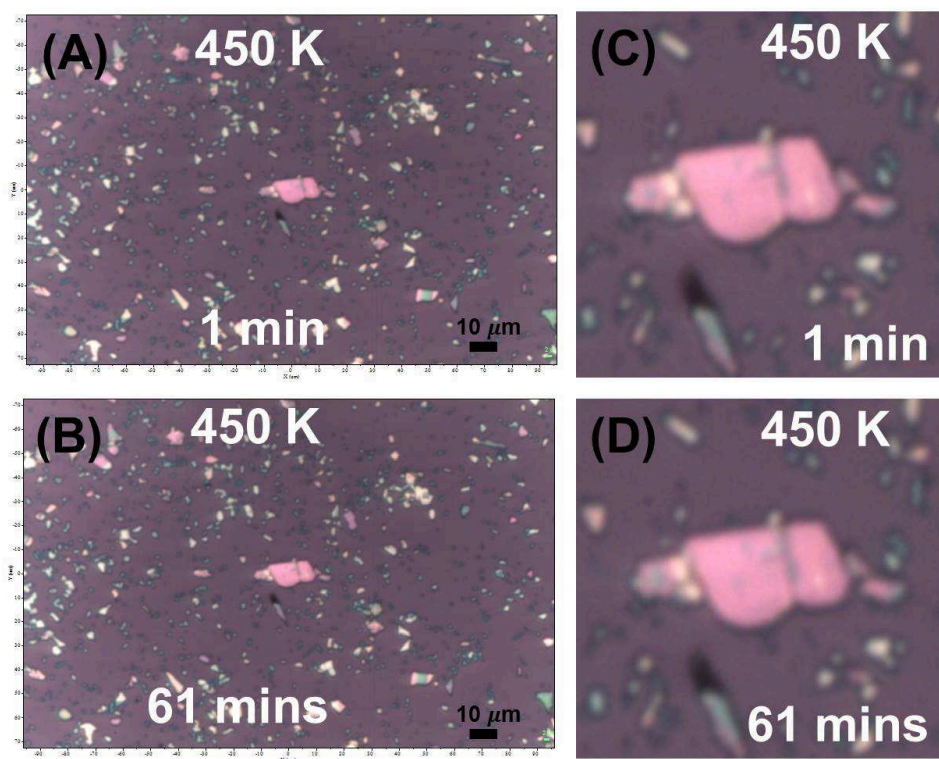
In addition, some other experimental details of those two reports were different from this study as well: 1. in Liu. et al's [25] report, they prepared their samples by liquid exfoliation method and the substrate was copper TEM grids, and in Fortin. et al's work [26], they prepared samples also by mechanical exfoliation method and used Si (100) substrates without oxide layer; 2. the energies of TEM

and LEEM electron beams for imaging used in those 2 works were 200 KeV and 30-35 eV, respectively. According to Vierimaa. et al's report [99], if the energy of electron beam is larger than 80 KeV, it would immediately rapidly lead to a considerable amount of damage to BP sample. Therefore, our work cannot be compared directly with those 2 studies directly without considering these experimental details.

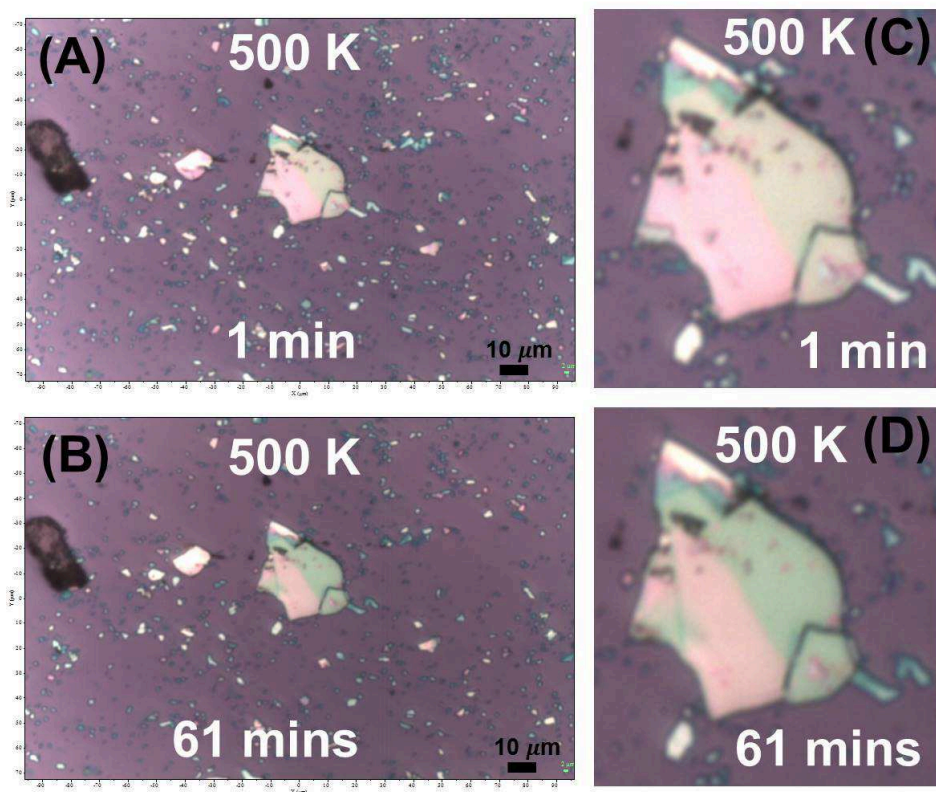
So far, no comprehensive investigations have been conducted on the thermal stability of BP below 375 °C (650 K) under stable heating and without the introduction of electron beams. To address, 6 independent investigations were conducted to observe the sublimation process of BP heated for 1 hour at 450 K ( $\sim 180$  °C), 500 K ( $\sim 230$  °C), 550 K ( $\sim 270$  °C), 600 K ( $\sim 330$  °C), 620 K ( $\sim 350$  °C), and 670 K ( $\sim 400$  °C), respectively.

First, Fig 2.6 (A) - (D) illustrated the comparison of BP flakes before and after heating for 1 hour at 450 K. There was a large BP flake with an area over than  $200 \mu\text{m}^2$  in the center of (A), with many small BP flakes dispersed around it. Significantly, in (B) and (D), which showed that after heating for 1 h, no observable changes took place. Therefore, it could be concluded that the exfoliated BP flakes remained stable during one-hour heating under 450 K ( $\sim 180$  °C).

Secondly, Fig 2.7 (A) - (D) illustrate the comparison of BP flakes before and after heating for 1 hour at 500 K. Obviously, after heating for 1 hour, the comparison between (A) and (B) shows that many small flakes disappeared, which was different from Fig 2.6. In addition, for the large BP flake in the center of (A), the color changes in (D) indicated the attenuation of thickness also took place. Moreover, no observable changes of area of the flake were observed. Then it could be concluded that, the sublimation of the exfoliated BP flakes took places at 500 K ( $\sim 230$  °C).



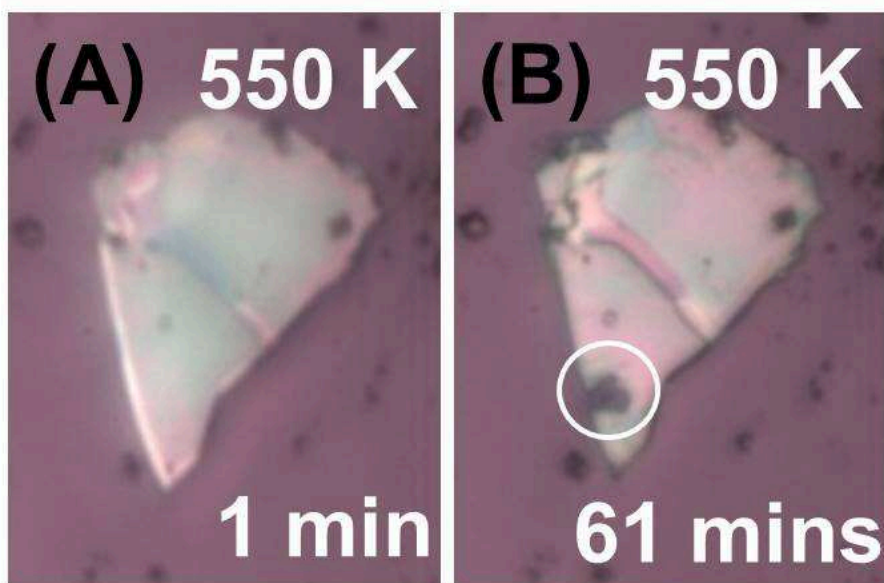
**Figure 2.6:** Sublimation study of BP at 450 K ( $\sim 180$  °C). (A): the BP samples heated at 450 K for 1 minute; (B): the BP samples heated at 450 K for 61 minutes; (C): zoom in of the sample in the center of (A); (D): zoom in of the sample in the center of (B).



**Figure 2.7:** Sublimation study of BP at 500 K ( $\sim 230$  °C). (A): the BP samples heated at 500 K for 1 minute; (B): the BP samples heated at 500 K for 61 minutes; (C): zoom in of the sample in the center of (A); (D): zoom in of the sample in the center of (B).

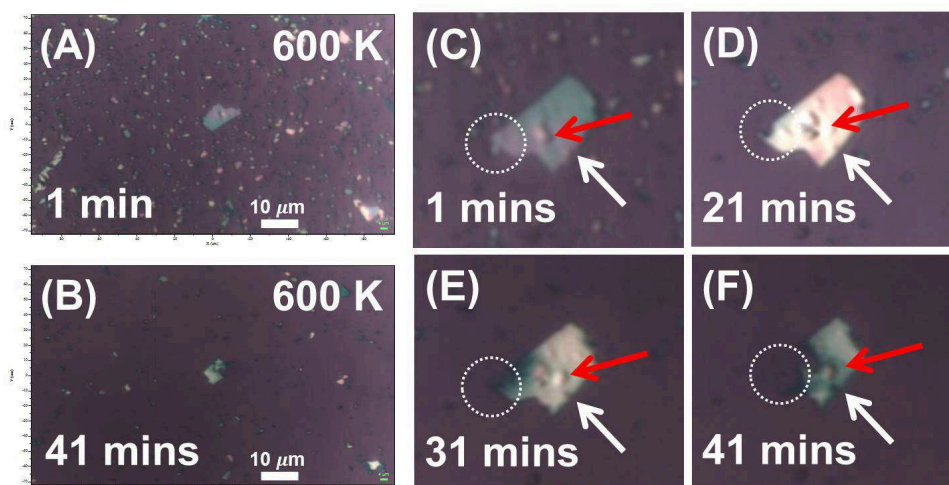
In our study, besides uniform thinning without the generation of observable defects, the propagation of micron-scale cracks and non-uniform thinning was also observed, which showed a strong dependence on the initial sample quality. A few examples are shown below.

Thirdly, the thermal stability of the exfoliated BP flakes at 550 K ( $\sim 280^\circ\text{C}$ ) was studied: in Fig 2.8, in comparison with the original sample shown in (A), the sample in (B) after heating for 1 hour showed non-uniform colors, indicating different thickness, and that was in agreement with (A). In addition, in (B), an eye-shape crack generated in the circled area. The original sub-micro scale defects, surface contaminants and cracks might have existed in the original sample, and those resulted in the eye-shape crack under high temperature.



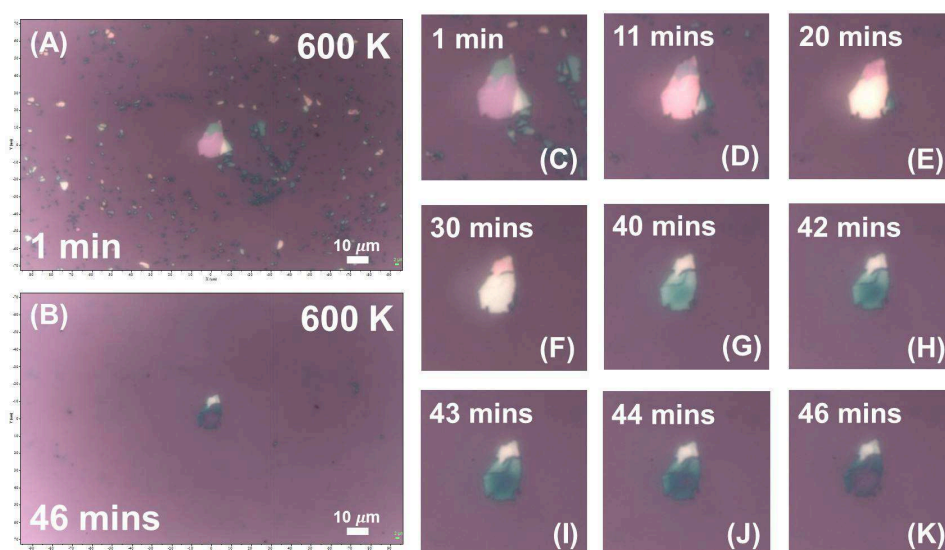
**Figure 2.8:** Sublimation study of BP at 550 K ( $\sim 280^\circ\text{C}$ ). (A): the BP samples heated at 550 K for 1 minute; (B): the BP samples heated at 550 K for 61 minutes.

Fourthly, Fig 2.9 (A) - (B) show the comparison of BP flakes before and after heating for 46 minutes at 600 K ( $\sim 330\text{ }^\circ\text{C}$ ). Obviously, the comparison between (A) and (B) demonstrated that after heating for 46 minutes, most of the small flakes disappeared, which was similar to Fig 2.7. Moreover, for the large BP flake in the center of (A), the optical images taken at different time intervals revealed the dynamic sublimation process of this BP flake: apparently, this flake started with different original thicknesses (see the non-uniform colors) and many visible defects introduced during mechanical exfoliation (see the rough surface and cracks along the edges). With increasing time, in the circled area, more severe sublimation took place than the other area, and eventually in (F), the eye-shape crack propagated. The arrows in (C) - (F) indicated the formation of cracks. Therefore, surface contaminants and non-uniform starting thickness resulted in the generation of cracks and fractures of BP flakes during sublimation process.



**Figure 2.9:** Sublimation study of BP at 600 K ( $\sim 330\text{ }^\circ\text{C}$ ). (A): the BP samples heated at 600 K for 1 minute; (B): the BP samples heated at 600 K for 41 minutes; (C)-(K): the zoom-in optical images of the sample in the center at (A) heated at 600 K for 1, 21, 31 and 41 minutes, respectively.

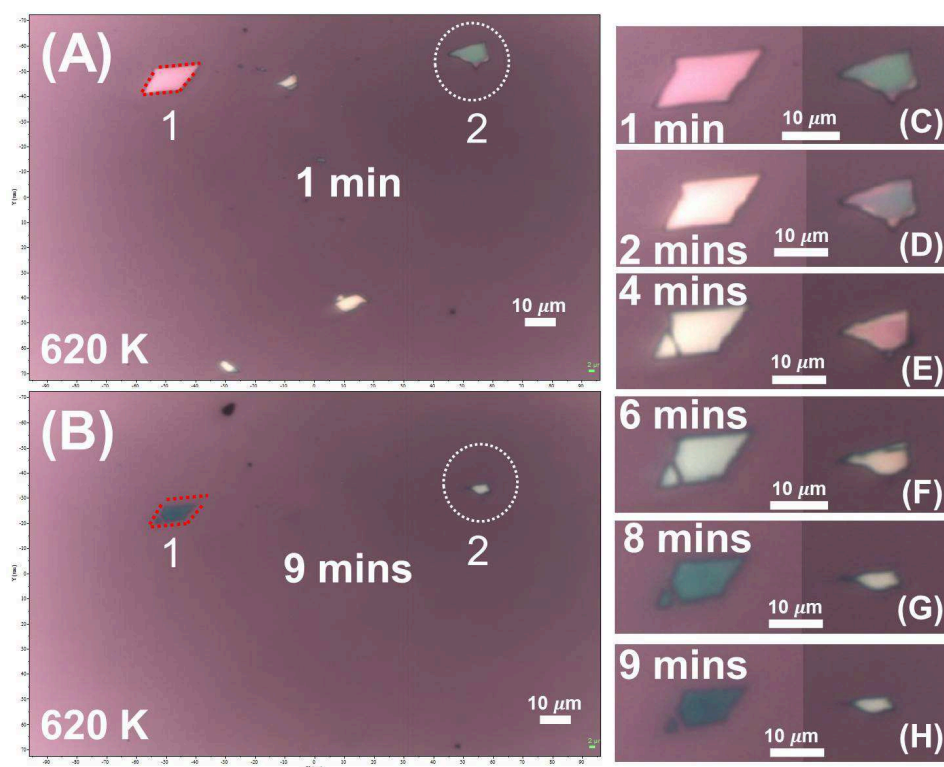
After that, via heating BP samples on another piece of Si wafer at 600 K for 46 minutes, another observation was performed. The comparison between (A) and (B) indicated an eye-shaped hole appeared in the center of the large BP flake; and the optical images of (C) - (K) taken at different time intervals revealed the dynamic formation and expansion of the hole which initiated from relative thinner center region (see (G)), then grew concentrically and eventually generated the large hole (see (K)).



**Figure 2.10:** Sublimation study of BP samples on another piece of Si wafer at 600 K ( $\sim 330$  °C). (A): the BP samples heated at 600 K for 1 minute; (B): the BP samples heated at 600 K for 46 minutes; (C)-(K): the zoom-in optical images of the sample in the center at (A) heated at 600 K for 1, 11, 20, 30, 40, 42, 43, 44 and 46 minutes, respectively.

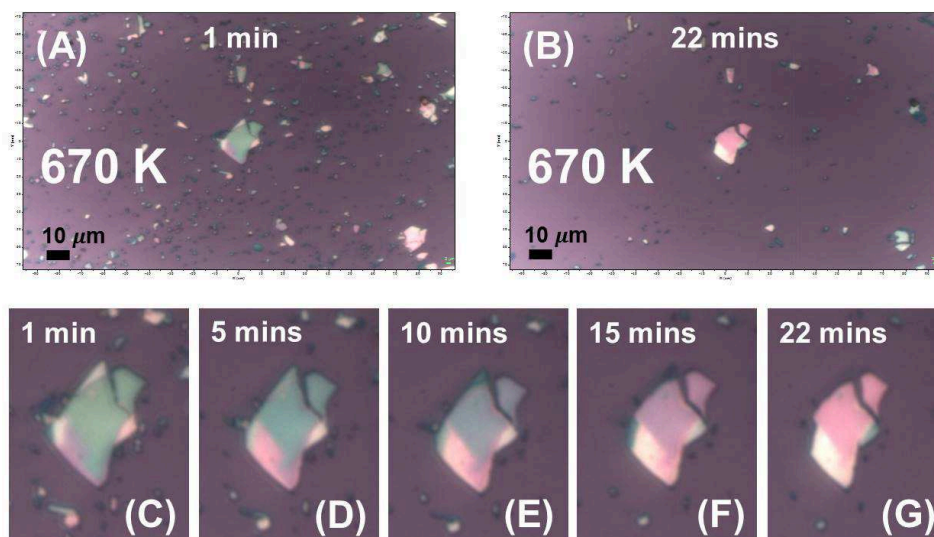


Fifthly, Fig 2.11 shows the comparison of BP flakes before and after heating for 9 minutes at 620 K ( $\sim 350^\circ\text{C}$ ). Notably, the comparison between (A) and (B) indicated that, both the left parallelogram-shape BP flake and right trapezoid-shape one retained their shapes except for shrinkage of area. Moreover, the optical images recorded at different time segments from (C) - (H) revealed the dynamic area shrinkage process. Based on the observation, it could be suggested that the thickness at edges were thinner than that of the center region, and due to the layer-by-layer sublimation, the edge regions were thinned down to 0 layer, in other words, fully sublimated first, which appeared as an area shrinkage.



**Figure 2.11:** Sublimation study of BP at 620 K ( $\sim 350^\circ\text{C}$ ). (A): the BP samples heated at 620 K for 1 minute; (B): the BP samples heated at 620 K for 9 minutes; (C)-(H): the zoom-in optical images of the marked sample in (A) heated at 620 K for 1, 2, 3, 4, 5, 6, 7, 8 and 9 minutes, respectively.

Sixthly, in Fig 2.12, it showed the comparison of BP flakes before and after heating for 22 minutes at 670 K ( $\sim 400^\circ\text{C}$ ). Similar to Fig 2.7, Fig 2.9 - Fig 2.11, in (B), most of the small flakes disappeared after heating for 22 minutes. Then, from (C) to (G), the clear, uniform and regular color changes in separated parts of this large BP flake indicated the dynamic sublimation process to be layer-by-layer. In addition, the well-preserved integrity of this flake during the progress of heating indicates that the surface of the original sample was relatively free of contaminants and defects.



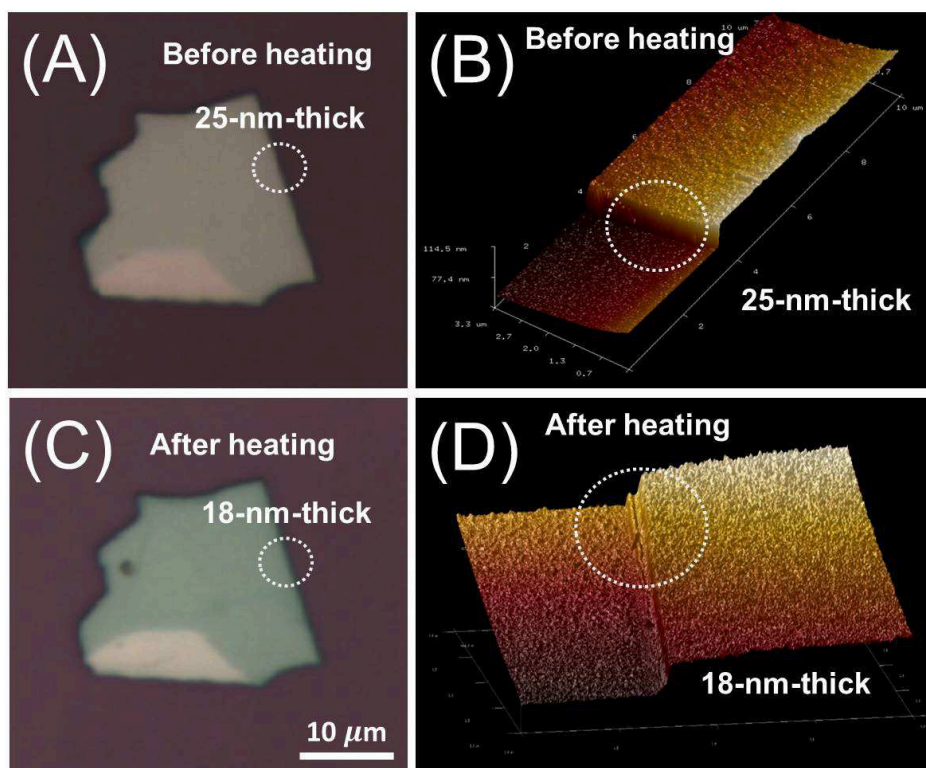
**Figure 2.12:** Sublimation study of BP at 670 K ( $\sim 400^\circ\text{C}$ ). (A): the BP samples heated at 670 K for 1 minute; (B): the BP samples heated at 670 K for 22 minutes; (C)-(G): the zoom-in optical images of the marked sample in (A) heated at 670 K for 1, 5, 10, 15 and 22 minutes, respectively.

### 2.2.1.5 Requirements For Sample Selection

To summarize, during the thermal thinning, both uniform and non-uniform thinning were observed. Some BP samples had crack generated, which in most cases can be related to the quality of the pristine BP flakes. Through optical microscopy, it was observed that large area samples free of micron-scale defects on the surface had more chances to be thinned down uniformly and without visible micron-scale defect generation.

As optical images and 2D Raman mapping are limited to micron-scale, for a BP flake which satisfies this method for sample selection, there are still possibilities that this flake has sub-micron-scale and nanoscale defects not observed by optical microscopy or 2D Raman mapping. Ideally, AFM/TEM should be used for that purpose. As this work was the first study on thermal thinning of BP, and also long-time air-exposure in AFM generate surface defects, thermal thinning was performed immediately after mechanical exfoliation and optical inspection. This empirical method for sample selection worked well. It was estimated that about 70 % of BP flakes selected by optical inspection could be thinned down without observable defect generation.

Let us look at some 3D AFM images of the samples which were thinned down successfully with their integrities kept, which can give more insights to the sample selection. In Fig 2.13 (A), the BP flake was the sample used for the successful layer-by-layer sublimation study for 500 K heating in section 2.2.1.3 (P 52), which had been heated for 2 cycles and showed a thickness of 25 nm, and clearly, this sample had no visible micron-scale defects. In (B), obviously, the 3D image indicated the steep sidewall, and the surface of the sample was flat which indicate the thickness to be uniform. In addition, significantly, despite the lower-left part of this flake, both the optical and the 3D AFM image confirmed the uniform edges of this sample. Moreover, after the third cycle of heating process, in (C), the optical image reflected the uniform color changes of this sample, and essentially the area of the sample remained same as that shown in (A). In (D), the 3D AFM image demonstrated not only the vertical side wall of the sample kept but also the flatness

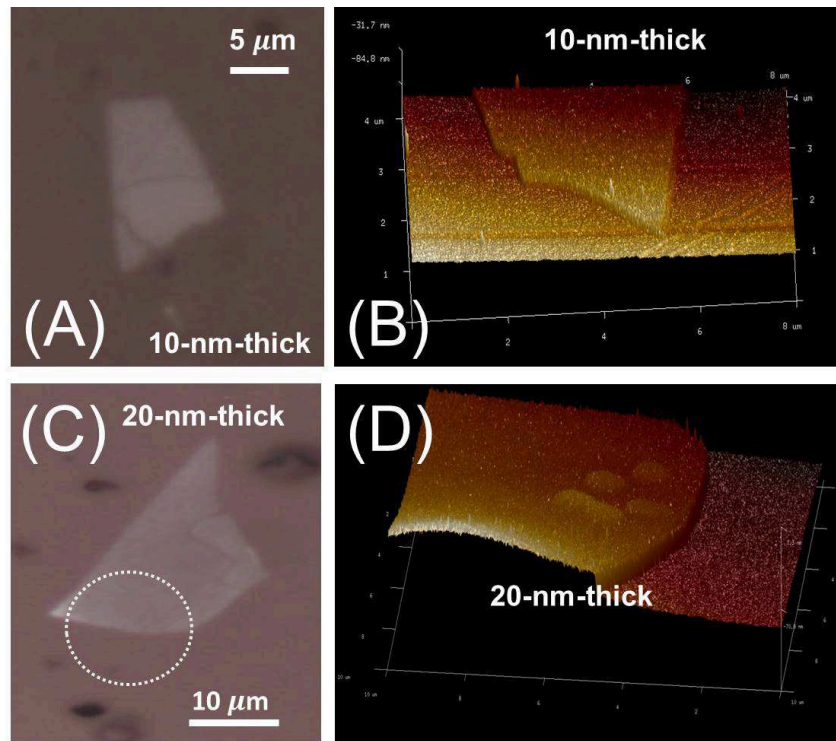


**Figure 2.13:** (A): Optical image of the 36-nm-thick sample used in Section 2.2.1.3 (P 52); (B): 3D AFM images of the 36-nm-thick sample shown in (A); (C): Optical image of this sample after thinning down to 18-nm-thick; (D): 3D AFM images of the 18-nm-thick shown in (C).

of the sample remained.

After that, in Fig 2.14, in (A) and (C), two BP flakes were successfully thinned down to 10-nm-thick and 20-nm-thick with well-kept integrity on polyimide substrate. Their 3D AFM images shown in the (B) and (D) also revealed the sample had uniform vertical side wall and flat surface (despite the minor oxidation) in nanoscale. Therefore, for successful thinning of a thick BP to few-layer, the requirements of selection of pristine sample could be summarized as:

1. The surface of sample should be clean, with no visible cracks and contam-



**Figure 2.14:** (A): Optical image of a prepared 10-nm-thick sample on polyimide substrate; (B): 3D AFM images of the 10-nm-thick sample shown in (A); (C): Optical image of a prepared 20-nm-thick sample on polyimide substrate; (D): 3D AFM images of the 20-nm-thick sample shown in (C).

inants dispersed on the surface of sample.

2. The sample should have uniform edges and vertical side walls. Optical imaging, although not sufficient in resolution, can be used to do a coarse sample selection fast and non-destructively. Future work needs to be conducted to find a better solution to check nm scale defects before thinning.

### **2.2.1.6 Thermal Stability Of BP & Sublimation Mechanism**

After the 6 independent studies of BP sublimation at different temperatures, it could be summarized that:

#### **1. Thermal Stability of BP**

The exfoliated BP flakes have no observable changes after one hour heating with a temperature less than 450 K ( $\sim 180^\circ\text{C}$ ), which is typically lower than the reported temperature of  $350^\circ\text{C}$  [25]; when the temperature is above 500 K ( $\sim 230^\circ\text{C}$ ), the sublimation of BP takes place if given enough time. This was still in agreement with the two previous reports on thermal stability of BP: the annealing time in Liu. et al.'s [25] work was less than 20 minutes and they indicated the decomposition temperature to be  $400^\circ\text{C}$ ; while another work [26] reported the decomposition temperature to be  $375^\circ\text{C} \pm 25^\circ\text{C}$  from a real-time measurement with increasing temperature. Both of the two previous works used far less heating time during the high temperature study of BP than this work. Therefore, not only the heating temperature but also the heating time will affect the thermal stability of BP. On the other side, the sublimation rates increase with increasing temperature. In other words, the sublimation rate is tunable by controlling the temperature.

#### **2. Sublimation mechanism of BP**

From above micron-scale observations by optical microscopy, it can be seen that, the samples (samples for 620 K and 670 K heating) which had relative clean and smooth surfaces as well as uniform edges underwent layer-by-layer attenuation of thickness with their uniformity well maintained, but those samples which had contaminated and rough surfaces as well as nonuniform edges (samples for 550 K and 600 K heating) were destructed by the formation of cracks.

The reported sublimation mechanism [26] can be used to explain the results: since the sublimation is initiated by the detachments of phosphorus dimers at the edges and vacancies, and the detachment rate along [100] direction (armchair) is

faster than that of [001] direction (zigzag), the eye-shaped cracks propagate along the [100] direction, enlarge and cause the full layer to be sublimated.

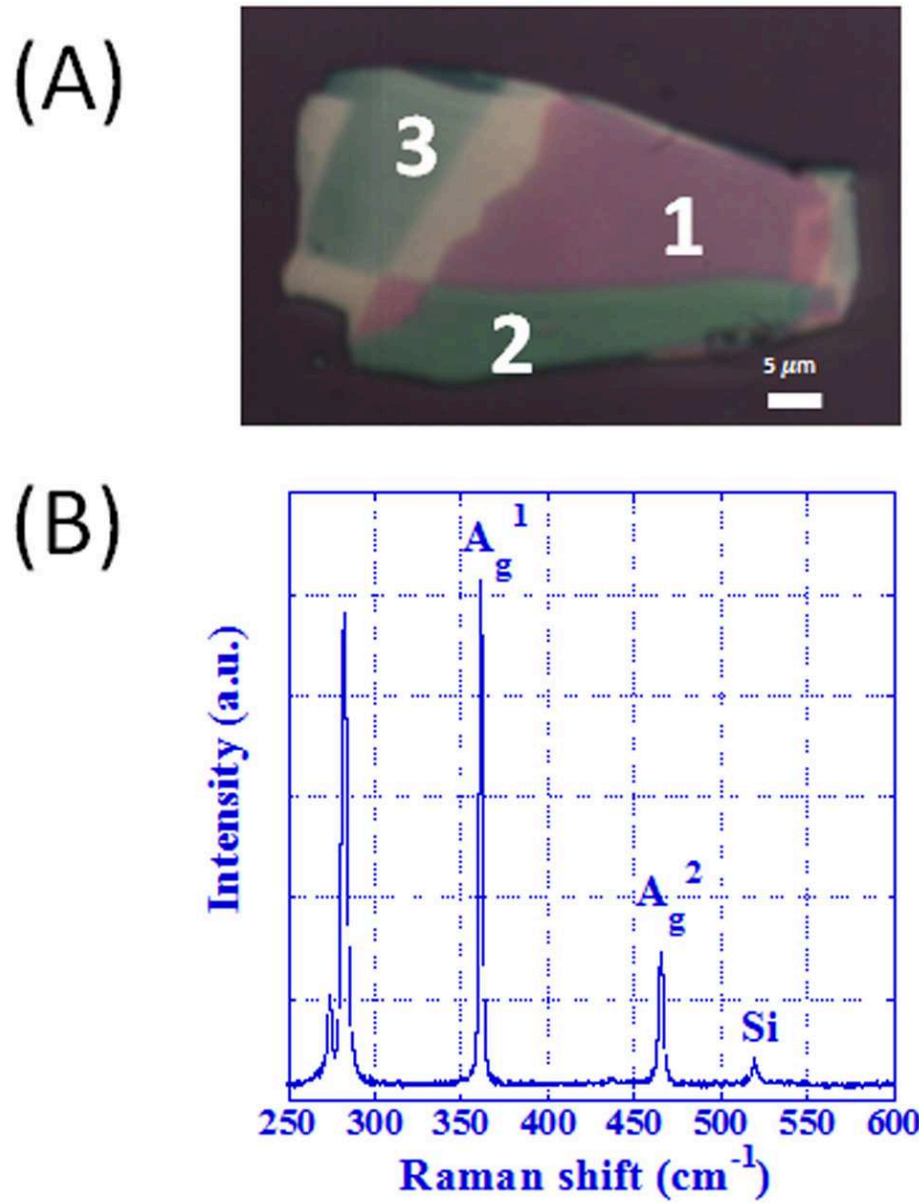
Therefore, the surface impurities and non-uniform edges are the main reasons that cause the decomposition or unsuccessful thinning of BP. The selection of samples then becomes critical for successful thinning.

### 2.2.2 Investigation of The Thinning Rates

After the discussion on the observation and mechanism of sublimation thinning, the thinning rates at different temperatures were investigated by two experiments termed “interrupted heating” and “continuous heating”, respectively.

Due to the anisotropic BP and Si (100) in-plane structures, the Raman peak intensities depend on the crystallographic orientation of the BP samples in respect to the polarization direction of the incident laser. The effectiveness of ARPRS measurements in identification of CO of BP was also a very important part of this work and the details would be discussed in section 3.3.2 (P 118) of Chapter 3. In short, from the ARPRS measurements, the axes of BP could be determined by the orthogonal directions of its maximum  $A_g^1$  (zigzag) and  $A_g^2$  (armchair) Raman intensities appeared [18][98]. Thus, in this work, the CO of samples was first determined by ARPRS and then transferred to the heating stage carefully with their positions unchanged.

In Fig 2.15 (A), a single flake (named “Sample A”) has been rotated to have maximum  $A_g^1$  Raman intensity and the minimum  $A_g^2$  intensity (see the Raman spectrum shown in Fig 2.15 (B)). There were 3 areas in the “Sample A” showing various colors indicating different thicknesses of those 3 areas. A Raman spectrum was taken from area 1. Similarly, in Fig 2.16 (A), another flake (named “sample B”, with two areas in different colors) was prepared by exfoliation. The Raman spectrum taken at area 2 also showed it has maximum  $A_g^1$  Raman intensity and the minimum  $A_g^2$  intensity.



**Figure 2.15:** (A): Optical image of sample A; (B): the Raman spectrum with the maximum intensity of  $A_g^1$  mode and the minimum intensity of  $A_g^2$  mode;

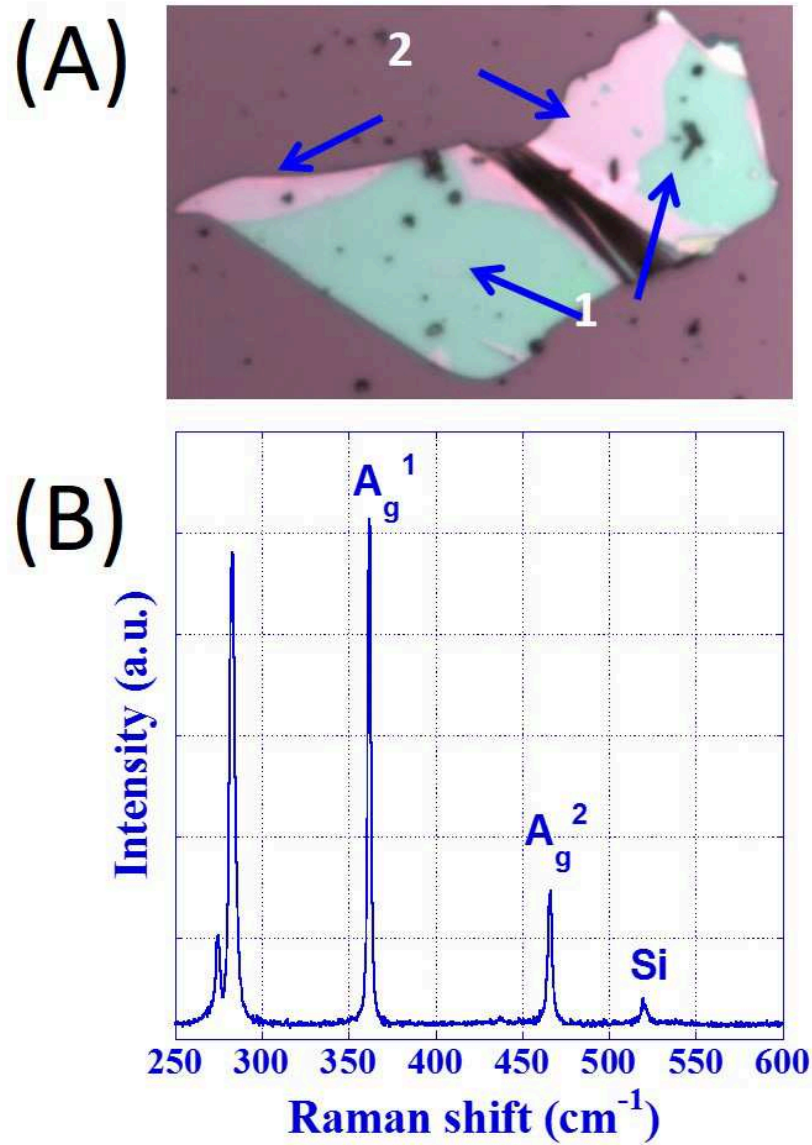


### **“Interrupted Heating” At 500 K And 550 K**

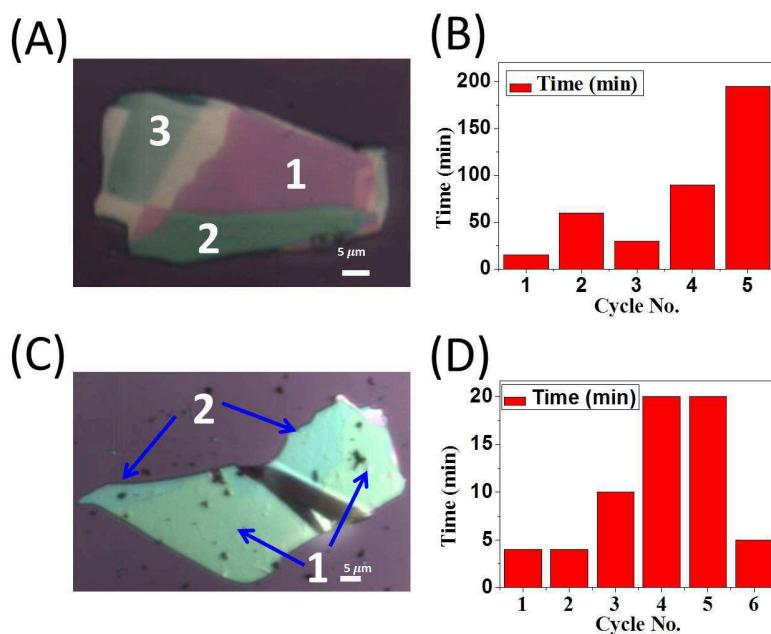
The “interrupted heating” was operated as follows: 5 cycles of the heating process were directed on single BP flake at 500 K (or 550 K). The time of each cycle was illustrated in Fig 2.17 (B). AFM measured the thickness before and after each heating process, and the results were demonstrated in Fig 2.18 (A). The “interrupted heating” can be described as follows: one cycle of heating was performed on single BP flake at 500 K (or 550 K), thicknesses before and after heating were acquired by AFM measurements. For each cycle, 2 Raman spectra were taken before and after heating at room temperature respectively; similarly, 2 Raman spectra were collected at the beginning and ending of the heating process at high temperature, respectively. The Raman results would then be discussed in section 3.3.2 (P 118) of Chapter 3.

In Fig 2.18 (A), it illustrates that, for each heating cycle, each area of sample A was reduced by the same thickness, revealing that different areas underwent identical sublimation rates. Similarly, in Fig 2.17 (C), sample B with 2 different areas was heated at 550 K for 6 cycles and the heating time for each cycle was listed in Fig 2.17 (D), the recorded thickness changes were plotted in Fig 2.18 (B), revealing that, at the heating temperature of 550 K, the sublimation took place isotropically in different areas.

Moreover, in Fig 2.19 (A), after heating for 3 cycles, the thickness of the area 3 of the “sample A” was reduced to  $\sim 5$  nm (see inset AFM profile in (A)). Since the critical thickness of BP from bulk to 2-dimensional was predicted as  $\sim 10$  nm [49] (or 20 layers), area 3 has a thickness of 10 layers. In Fig 2.19, the Raman spectrum indicated the uniformity and crystallinity of area 3. Significantly, this 5-nm-thick flake has a large area of around  $180 \mu\text{m}^2$ . In addition, Raman intensities of  $A_g^1$  and  $A_g^2$  remained strong while the Si Raman peak intensity was enhanced in comparison with the Raman spectrum of the original sample shown in Fig 2.15 (B).

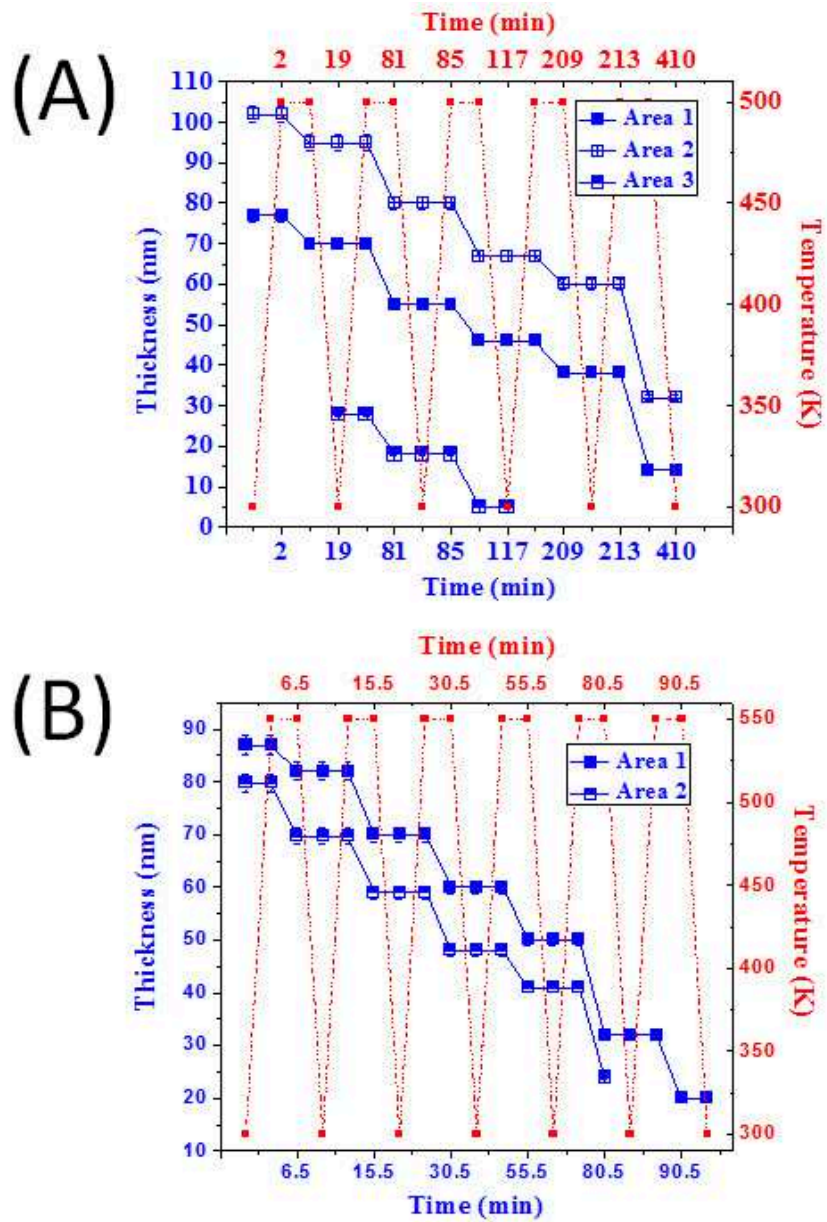


**Figure 2.16:** (A): Optical image of sample B; (B): the Raman spectrum with the maximum intensity of  $A_g^1$  mode and the minimum intensity of  $A_g^2$  mode;

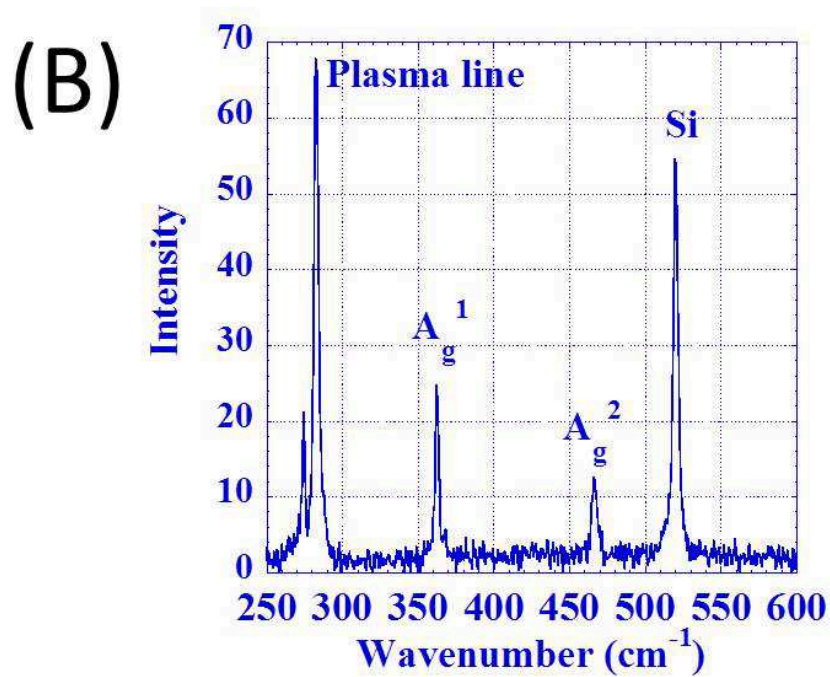
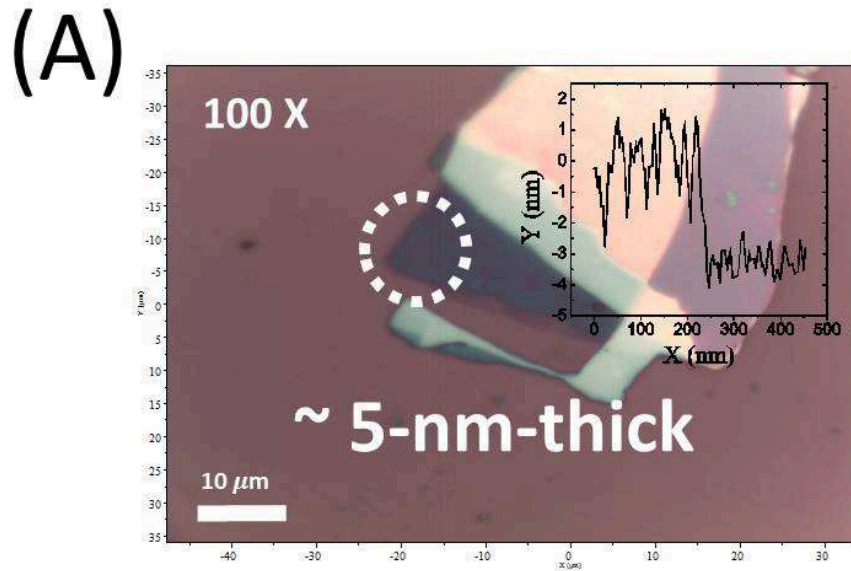


**Figure 2.17:** (A): Optical image of sample A to be heated at 500 K; (B) the illustration of the interrupted heating process (5 cycles) to be performed at sample A; (C): Optical image of sample B to be heated at 500 K. (D): the illustration of periodic heating process (6 cycles) to be performed on sample B.

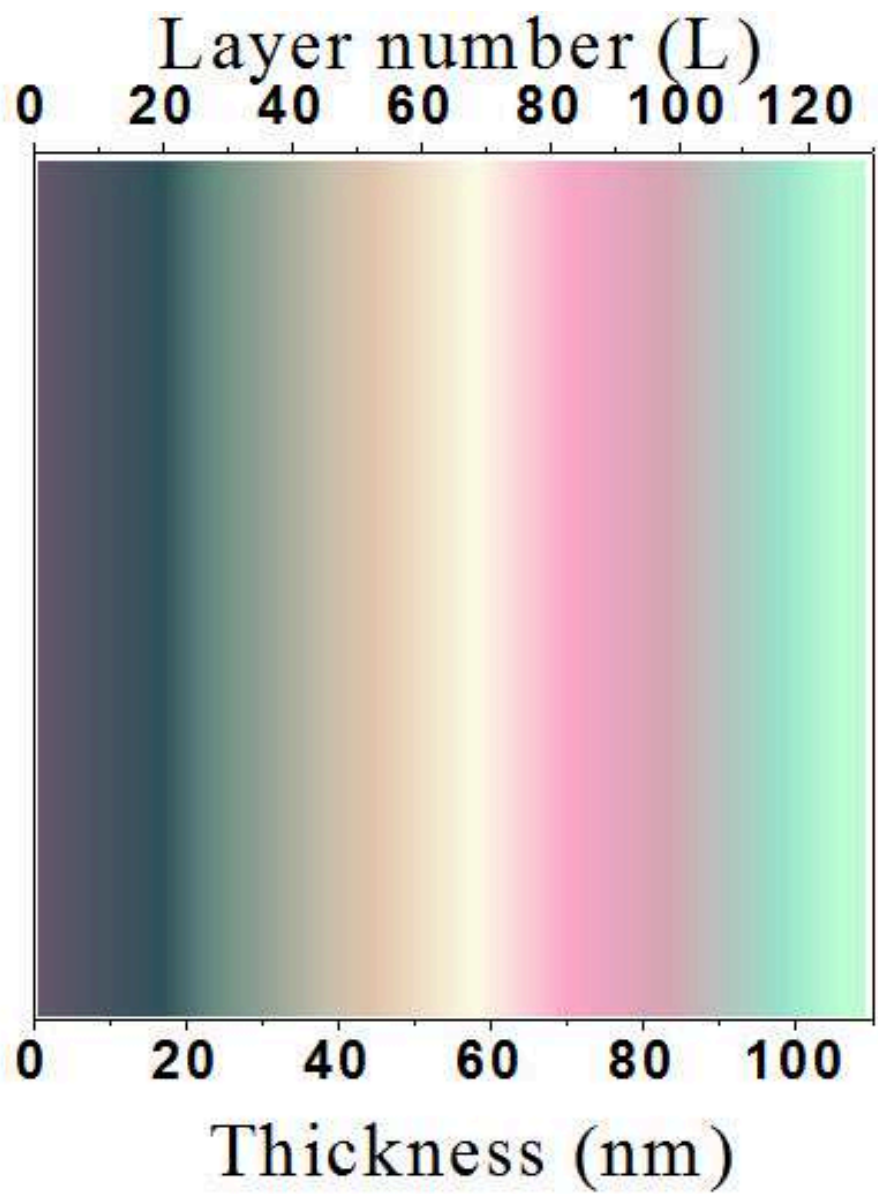
As mentioned in the observations of BP sublimation, the colors of BP changed with decreasing thickness. Therefore, if knowing the characteristic color of BP at each thickness, a thickness-color can be established which would be useful for thickness determination. This was realized after the “interrupted heating experiments. The characteristic colors extracted from those recorded optical images and their related thickness from AFM measurements were plotted as the thickness-color map shown in Fig 2.20.



**Figure 2.18:** (A): Thickness in different areas of sample A as a function of time, and (B): the thickness in different areas of sample B as a function of time. At each red dot, a Raman spectrum was collected (analysis of those collected Raman spectra would be discussed in Section 3.3.2 (P 118) of Chapter 3).



**Figure 2.19:** (A): Optical image of area 3 in Sample A, and the inset AFM profile indicated it was thinned down to 5-nm-thick; (B): Raman spectrum of the 5-nm-thick BP sample showing the 3 characteristic peaks of BP.

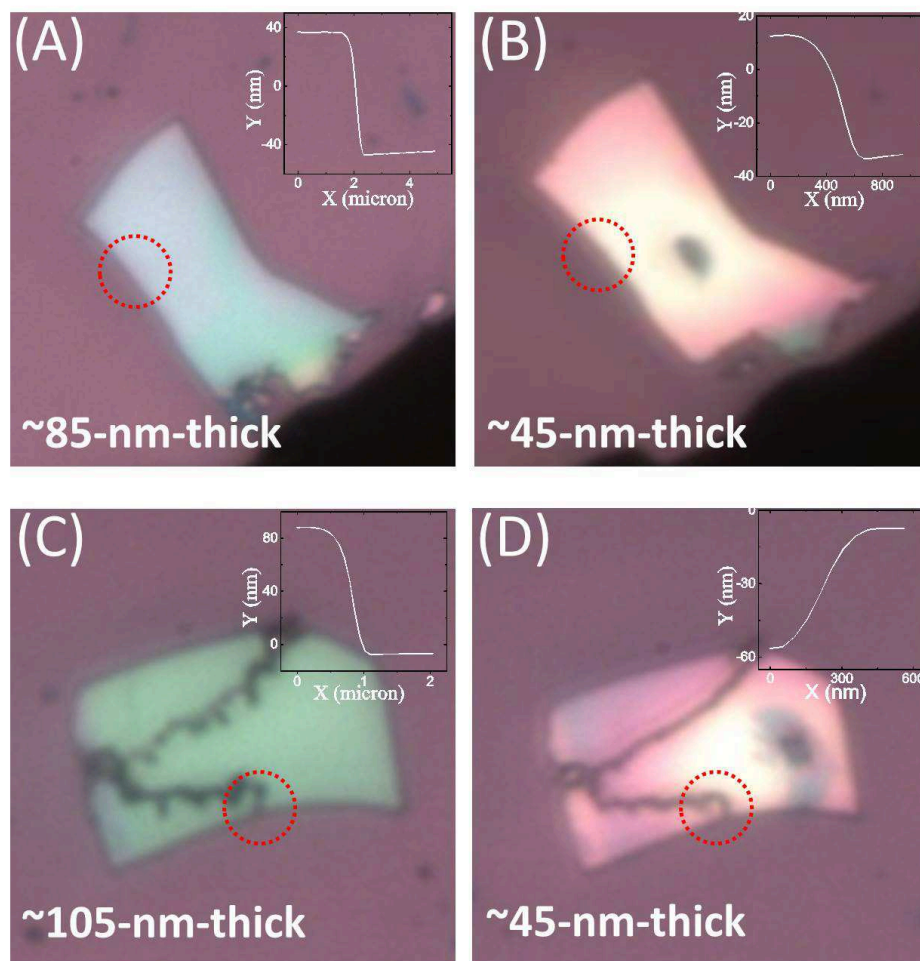


**Figure 2.20:** Thickness-color map: the colors were extracted from those sample of which the thicknesses had been measured by AFM;

### **“Continuous Heating” At 500 K And 550 K**

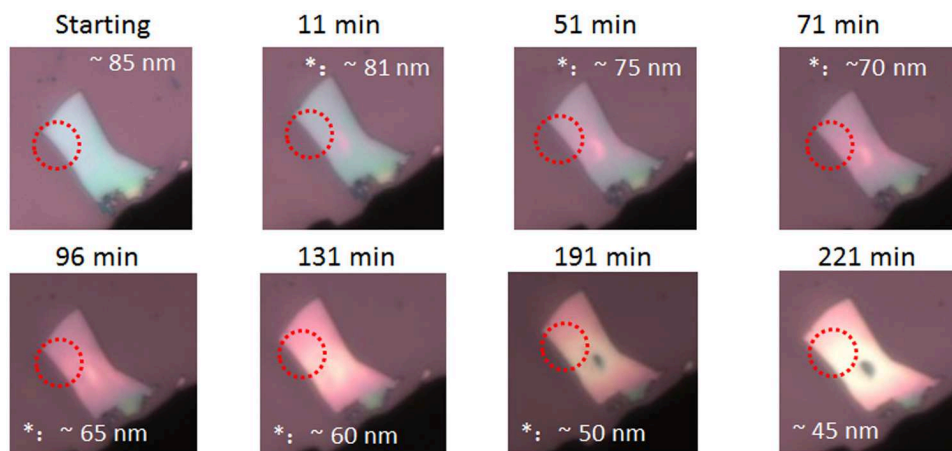
In order to get accurate thinning rates, the “Continuous Heating” was performed on two thick BP flakes labeled as sample C and D at 500 K and 550 K, respectively. In Fig 2.21 (A) and (B), the thickness of sample C was reduced from 85 to 45 nm after heating process at 500 K for 221 minutes; in Fig 2.21 (C) and (D), the thickness of sample D was reduced from 105 to 45 nm after heating process at 550 K for 51 minutes.

At different time intervals, the optical images were taken at the sample in order to record the gradual color changes (see in Fig 2.22 and 2.24). In addition, in-situ Raman spectra at each time interval were collected before taking images, and the frequent laser exposure caused the black spots on sample C and D shown in Fig 2.21 (B) and (D). The in-situ Raman spectra at 500 K and 550 K were shown in Fig 2.23 and Fig 2.25. Obviously, with increasing time during thinning, the Si peak intensity was enhanced while all 3 BP peaks remained unchanged.

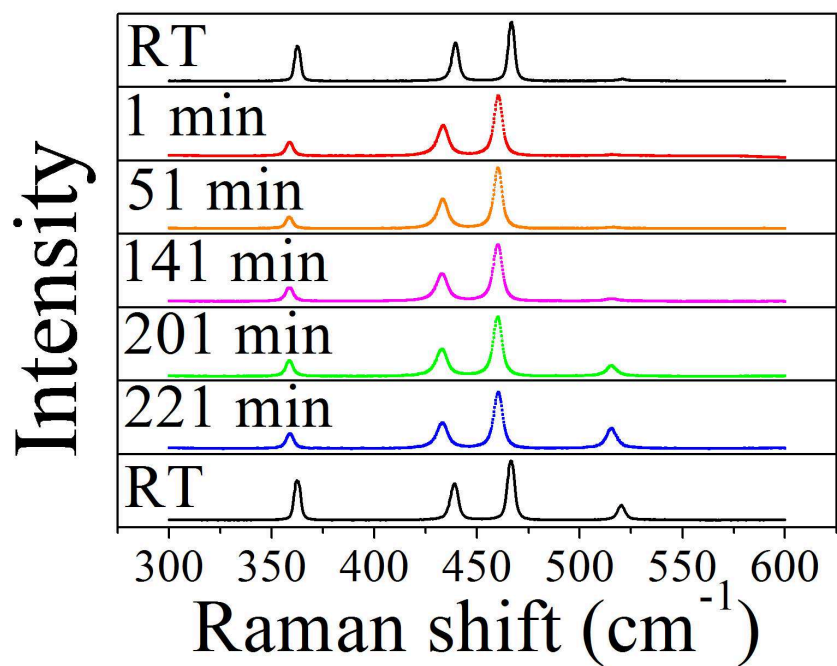


**Figure 2.21:** (A) & (B): Optical images of Sample C before and after continuous heating process at 500 K, the heating time was 221 minutes; (C) & (D): Optical images of Sample D before and after continuous heating process at 550 K, the heating time was 51 minutes. The inset profile in each picture is the line-scan AFM profile indicating the thickness of this sample.

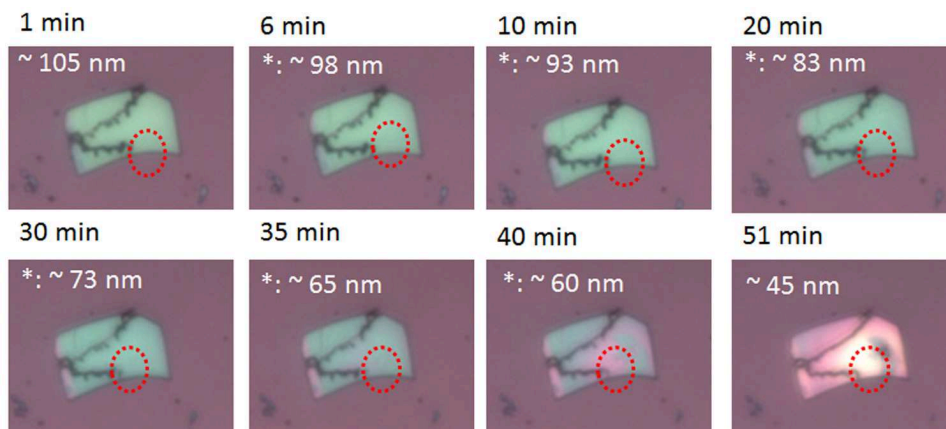




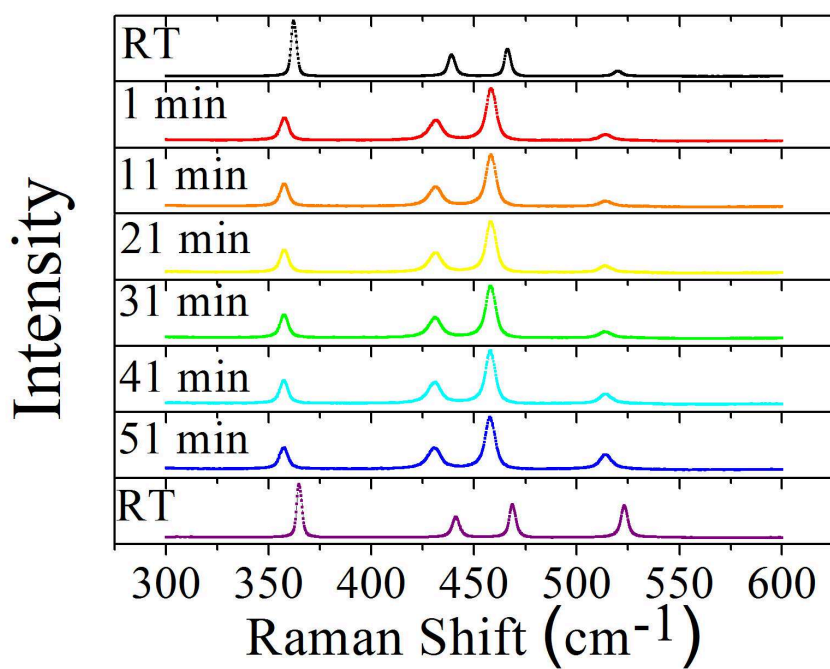
**Figure 2.22:** Sample C was annealed at 500 K for 221 minutes.



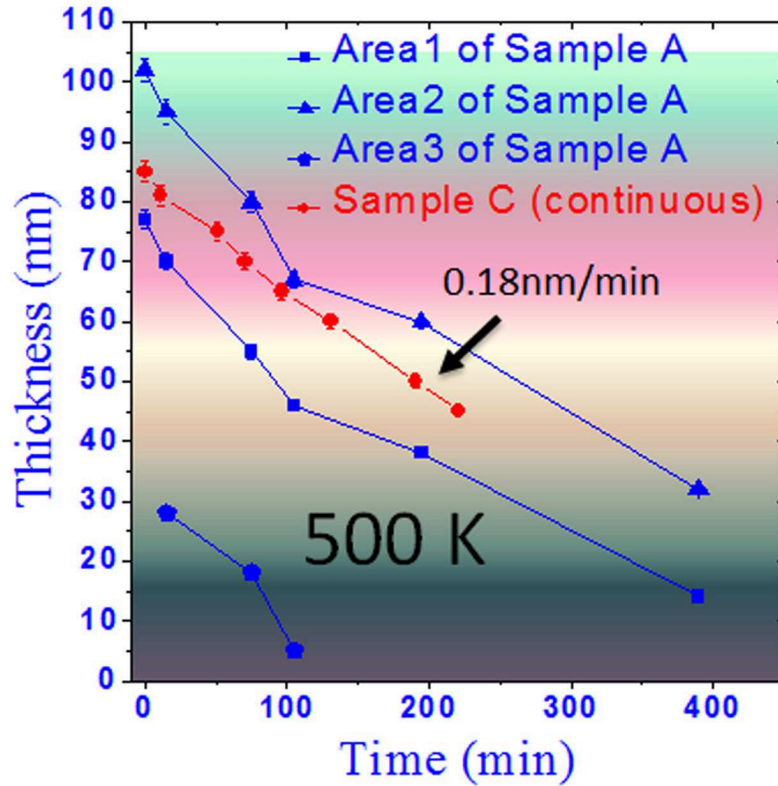
**Figure 2.23:** In-situ Raman spectra of the sample C at 500 K.



**Figure 2.24:** Sample D was annealed at 550 K for 51 minutes.



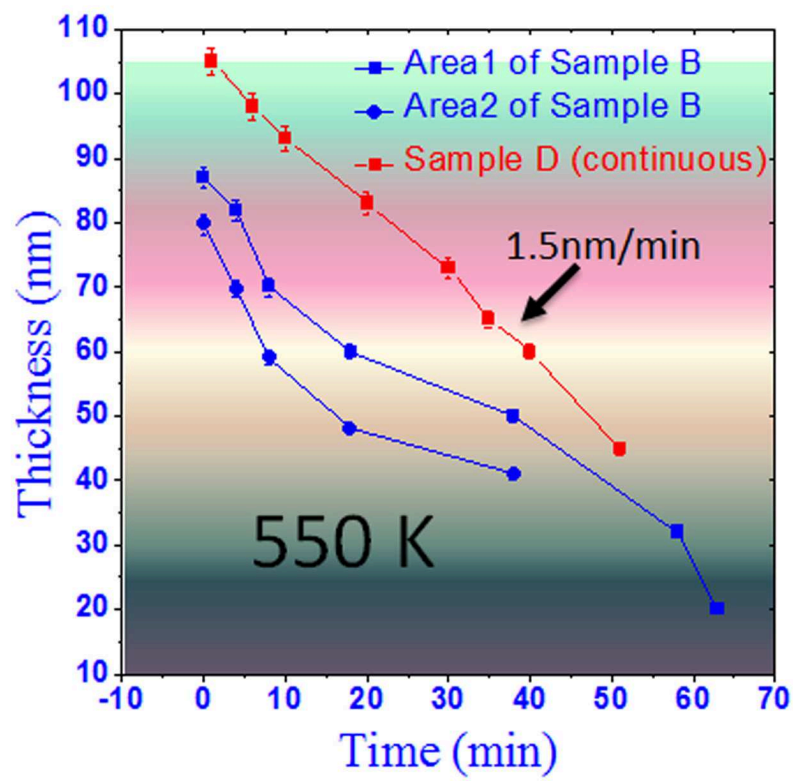
**Figure 2.25:** In-situ Raman spectra of the sample D at 550 K.



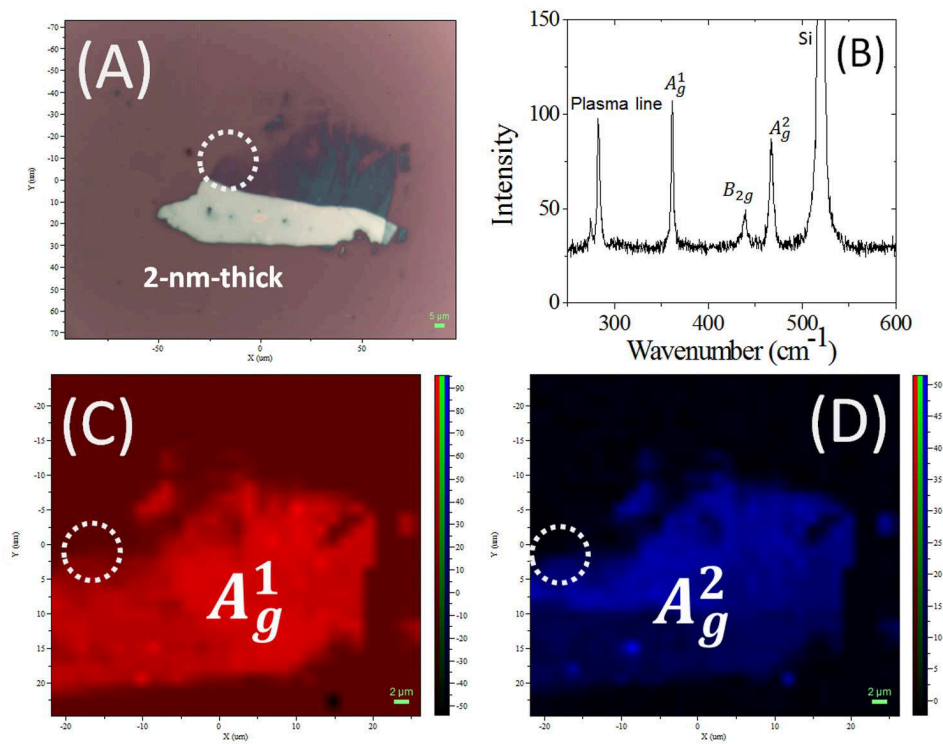
**Figure 2.26:** Comparison of thinning rates of sample A and C.

### Thinning rates

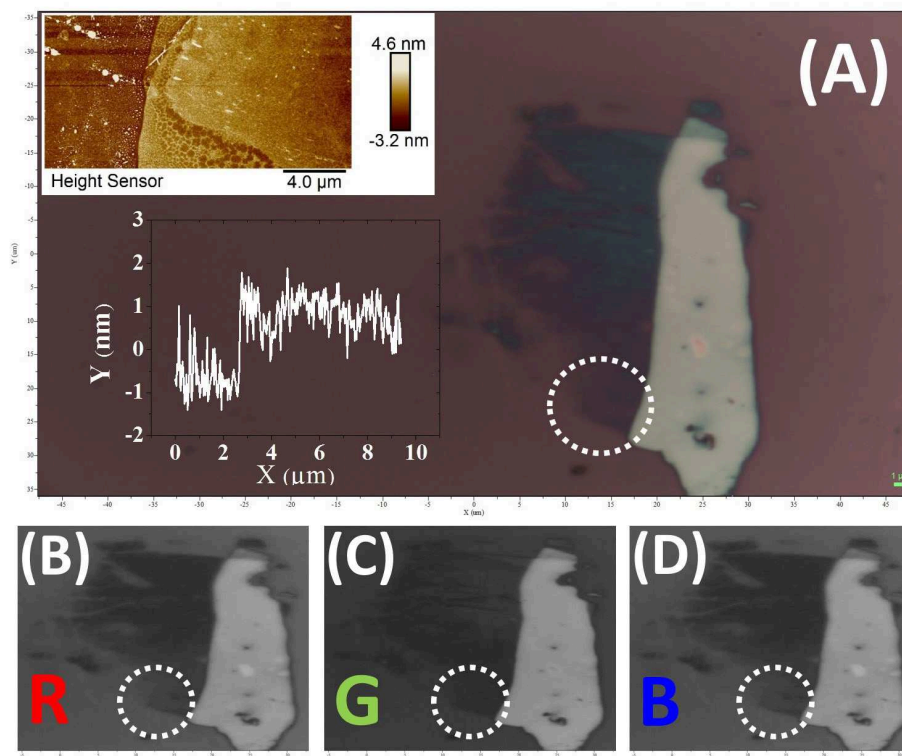
The thicknesses of sample C and D shown in those pictures of Fig 2.22 and 2.23 were read from the color-thickness map in Fig 2.20 and then interpolated into Fig 2.26 and Fig 2.27 ( the red line ). In addition, as shown in Fig 2.26 and Fig 2.27, the thickness-heating time profiles of sample A and C ( the blue lines ) for interrupted heating were also integrated. The thickness-heating time profiles of interrupted and continuous heating at 500 and 550 K matched. The thinning rates were  $\sim 0.18$  nm/min at 500 K and  $\sim 1.5$  nm/min at 550 K.



**Figure 2.27:** Comparison of thinning rates of sample B and D.



**Figure 2.28:** (A): Optical image the BP sample thinned down to 2-nm-thick; (B): Raman spectrum collected at the circled area in (A); (C) & (D): Spatial Raman maps of sample shown in (A).



**Figure 2.29:** (A): Optical image the BP sample thinned down to 2-nm-thick, and the inset figures represent the spatial AFM image and thickness profile of circled area. (B) - (D): Optical contrast analysis of Fig 2.28 (A), which was splitted into R, G and B channels, and the G channel figure in (C) was selected for analysis.

### 2.2.3 Preparation Of The few-layer BP

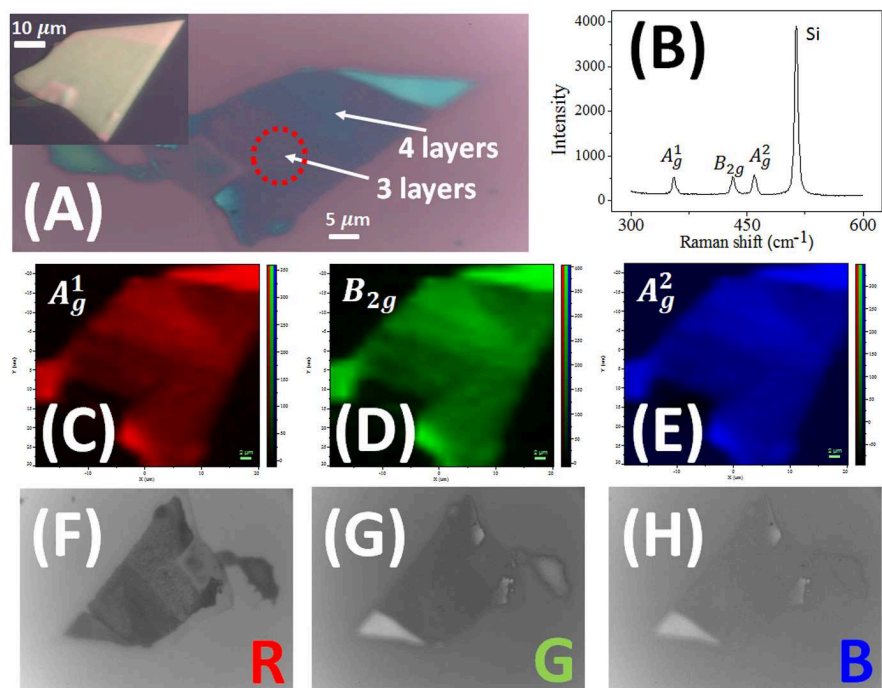
An additional cycle of heating was then performed with sample A. In Fig 2.27 (A), area 3 was entirely sublimated. In Fig 2.27 (B), the Raman spectrum at the circled position of Fig 2.27 (A) showed 3 typical BP peaks of  $A_g^1$ ,  $B_{2g}$  and  $A_g^2$  modes at 361.95, 439.57 and 466.81  $\text{cm}^{-1}$ , respectively. What's more, in Fig 2.27 (C) & (D), the spatial Raman maps of  $A_g^1$  and  $A_g^2$  modes showed strong contrast between the sample and substrate, which indicated the crystallinity of whole BP sample was

still retained. In Fig 2.28 (A), the thickness of the circled area was measured: the inset AFM image and profile were shown in Fig 2.28 (A), which indicated that the thickness of area 1 was reduced to  $\sim 2$ -nm-thick. According to previous report, a single layer BP sample has a theoretical thickness of 0.53 nm [49][63], so that that prepared BP sample has 4 layers.

For thickness measurement of 2D material less than 15 layers, AFM measurements can bear significant errors due to the surface absorption layers (absorption of water and oxygen in air) [100]. For example, Liu. et al. [9] reported that thickness of a single layer was measured to be 0.85 nm by AFM, which was far greater than 0.53 nm. That should be attributed to the fast degradation of BP during measurements. Therefore, it is necessary to find an effective non-contact method to quantify the layer number of BP when it is less than 15 layers.

As the average optical contrast has been demonstrated to be a useful tool in indicating 2D materials with a thickness below a few nanometers [101][100], Fig 2.29 (A) was splitted into monochromic red (R), green (G), and blue (B) channel images via Image J [102] shown in Fig 2.29 (C) - (D). Here the highest-contrast gray-scale image in the G channel was selected and then shown in Fig 2.29 (C). It is important to note that, the average optical contrast between the sample and the substrate in the G channel image increases by the layer number. According to Gomez et al. [46]'s report, monolayer BP showed an optical contrast of 2.8 %, while the bilayer BP flake showed an optical contrast of  $5.5 \pm 0.2$  %. The contrast of the sample in (A) had a mean value of 10.89%. As mentioned above, this sample was measured to be 2-nm-thick, corresponding to  $\sim 4$  layers. Therefore, the optical contrast can be regarded as a linear function of layer number when it is less than 15 layers and it could be used for determination of layer number.

After that, repeatable preparation of large few-layer BP was performed. In Fig 2.30 (A), successful preparation of a thin BP flake with an area over  $\sim 1,000 \mu\text{m}^2$  by continuously heating a thick bulk BP flake (see the inset image of Fig 2.30 (A)) at  $300^\circ \text{C}$  under  $\text{N}_2$  protection was demonstrated. Despite the cracks generated in the circled area, the entire sample retained its integrity after the process. In Fig



**Figure 2.30:** (A): Optical image a BP sample thinned down to 3 and 4 -layers, and the inset figure represents the original BP sample. (B); Raman spectra collected in circled area in (A); (C) - (E): Spatial Raman maps of the BP sample shown in (A); (F) - (H): Optical contrast analysis of (A), which was splitted into R, G and B channels, and the G channel figure in (C) was selected for analysis.

2.30 (B), the point Raman spectrum collected circled area in Fig 2.30 (A) showed 3 typical BP Raman peaks at 355.414, 431.21 and 459.24  $\text{cm}^{-1}$ , respectively. In addition, Raman mapping at this sample was performed. In Fig 2.30 (C) - (E), the 3 BP vibrational modes  $A_g^1$ ,  $B_{2g}$  and  $A_g^2$  showed a strong intensity contrast in comparison with the substrate, which indicated the crystallinity of the prepared sample. Moreover, in Fig 2.30 (F) - (H), the average optical contrast results in Fig 2.30 (A) have 2 mean values of 7.21% and 10.96%, corresponding to 3 and 4 layers.

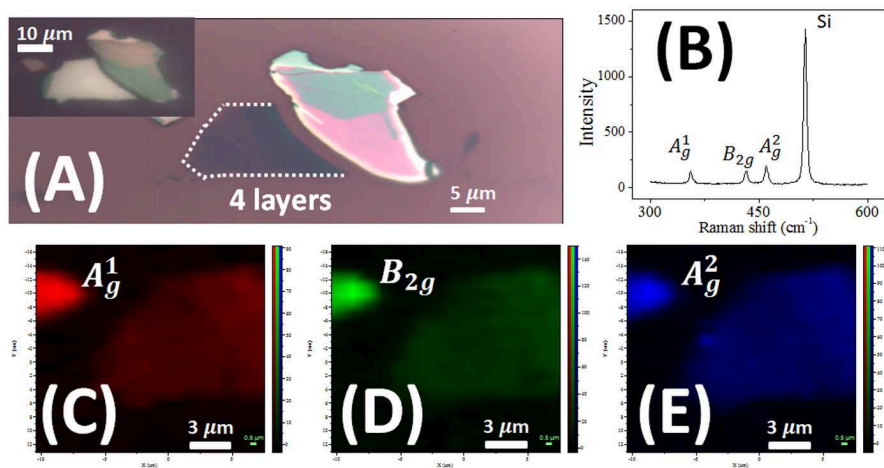


Then, repeatedly, in Fig 2.31 (A) and Fig 2.32 (A), another 2 independent few-layer BP flakes were prepared: the sample in Fig 2.31 (A) has an area of  $\sim 250 \mu\text{m}^2$ , and the average optical contrast shows a mean value of 9.20%, corresponding to 4 layers; the sample in Fig 2.32 (A) has two areas, and the average optical contrast results show two means values of 6.52% and 7.68%, corresponding to bilayer and 3 layers.

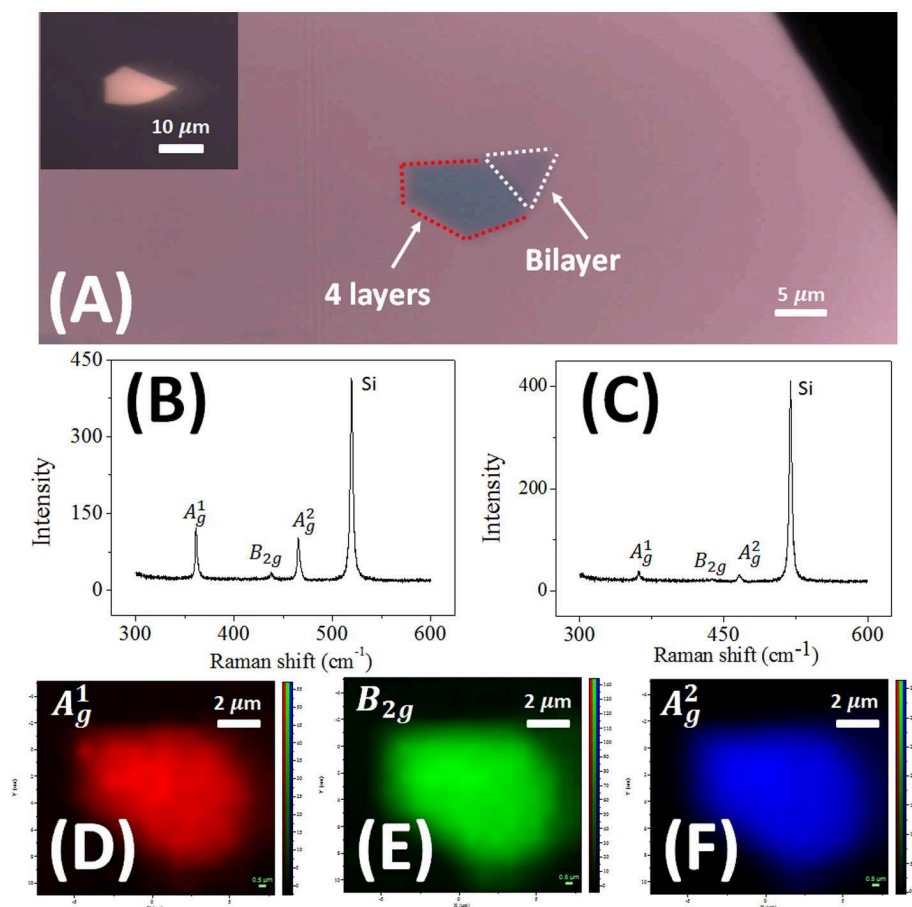
After that, in Fig 2.31 (B), the Raman spectrum collected at the sample shown in Fig 2.31 (A) showed 3 strong BP peaks at 356.05, 432.48 and 459.87, respectively. Moreover, in Fig 2.31 (C) - (E), Raman mapping results also indicated the crystallinity of the entire sample retained after thermal thinning process.

Similarly, in Fig 2.32 (B) & (C), the Raman spectra of the 4-layer / bilayer region showed 3 typical BP peaks at 361.03 / 361.39  $\text{cm}^{-1}$ , 437.75 / 438.19  $\text{cm}^{-1}$  and 465.19 / 465.55  $\text{cm}^{-1}$ , respectively. Additionally, in Fig 2.32 (D) to (E), the spatial Raman maps of the BP sample also confirmed the crystallinity of the whole sample.

Overall, our results showed that the sublimation thinning method was an effective method in preparing large few-layer BP.



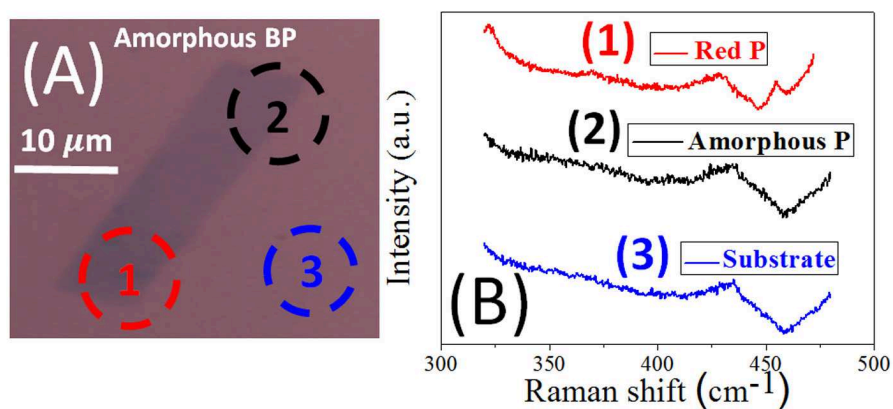
**Figure 2.31:** (A): Optical image of a BP sample thinned down to 4 layers, and the inset figure represents the original BP sample. (B); Raman spectra collected in circled area in (A). (C) - (E): Spatial Raman maps of the BP sample shown in (A). (F) - (H): Optical contrast analysis of (A), which was splitted into R, G and B channels, and the G channel figure in (C) was selected for analysis.



**Figure 2.32:** (A): Optical image of a BP sample thinned down to 4 and double layers, and the inset figure represents the original BP sample. (B); Raman spectra collected in circled area in (A). (C) - (E): Spatial Raman maps of the BP sample shown in (A). (F) - (H): Optical contrast analysis of (A), which was splitted into R, G and B channels, and the G channel figure in (C) was selected for analysis.

Furthermore, in Fig 2.33 (A), in order to prepare monolayer BP, a thick BP flake was carefully thinned down to have an average optical contrast of 4.88%, which corresponds to the layer number of 1 - 2 layers. Then Raman measurements of this flake were performed: in Fig 2.33 (B), the Raman spectrum (the red profile 1) collected at the “area 1” in (A) showed only the  $A_g^2$  mode of BP at  $468\text{ cm}^{-1}$ , and no  $A_g^1$  and  $B_{2g}$  peaks were observed; the Raman spectrum (the black profile 2) collected at the “area 2” in (A) showed the same profile as the amorphous P shown in Fig 1.4 (A) of Chapter 1, which indicated this area to be amorphous and the Raman signals were from the Si substrate; the blue profile 3 was the Raman spectrum of the Si substrate (the “area 3”).

Overall, the preparation of single-layer BP wasn't successful in this work. The reason lies in: when the BP flake is thinned down to single-layer, if the heating continuous, the crystallinity of BP will degrade, in other words, the phase transformation will take place from crystalline BP to amorphous phosphorus. Therefore, in order to prepare crystalline single-layer BP, more works should be conducted on the thermodynamics of phase change, which can be used for optimizing the heating time at specific temperatures.



**Figure 2.33:** (A): Optical image of a BP sample thinned down to single layer. (B): Raman spectra of this sample collected at 3 regions.

## 2.2.4 Comparison Of BP Products With Previous Techniques

In comparison with the final BP products prepared by previous techniques, the thermal thinning method has several advantages:

1. **Thinning limit:** The thinning limit in this work is double layers, corresponding to 1 nm, which is close to the mechanical exfoliation and plasma thinning methods, identical to liquid exfoliation method, and better than the anodic oxidation thinning, PLD and CVD methods.

2. **Scalability of products:** The BP products prepared in this work have areas all greater than  $250 \mu\text{m}^2$ , which are 10 to 100 times larger than the BP products prepared by the previous 6 techniques.

3. **Uniformity** 2D Raman mapping results indicate the uniformity of the BP products prepared in this work kept well after thinning process, which is far better than the BP products prepared by previous 6 techniques. The uniformity of the final products is only decided by that of the pristine sample.

4. **Crystallinity** The crystallinity of the prepared products remains after thinning process, which is identical to those prepared by the mechanical exfoliation method, and better than the other methods.

5. **Controllability of thickness:** In next chapter, the controllability of thickness by Raman intensity ratios of  $\frac{I_{Si}}{I_{A_g^2}}$  will be discussed. However, there are no discussions on thickness control in the 6 previous techniques.

## 2.3 Conclusions

In summary, the observation of the layer-by-layer sublimation of black phosphorus at 500 - 600 K was first reported. The thinning rates for “continuous heating” were  $\sim 0.18 \text{ nm/min}$  and  $1.5 \text{ nm/min}$  at 500 and 550 K, respectively. Large (with areas  $> 200 \mu\text{m}^2$ ) and few-layer (2 to 4 layers) BP flakes with good integrity, uniformity and crystallinity were prepared successfully and repeatedly. No micron

scale defects were observed. Overall, the sublimation thinning method provides a new approach to reduce BP thickness to few layers while keeping its crystallinity and integrity and with a good thickness controllability. This method is also expected to work for deposited BP besides exfoliated BP. The sublimation thinning method is promising in further fabrication of high quality few-layer BP in large scale.

## **Chapter 3**

# **Determination of Crystallographic Orientations For BP Thickness Determination And Control By Raman Spectroscopy With 442 nm Excitation**

*“Have not the small Particles of Bodies certain Powers, Virtues or Forces, by which they act at a distance, not only upon the Rays of Light for reflecting, refracting and reflecting them, but also upon one another for producing a great part of the Phenomena of Nature?”*

— Sir Isaac Newton

### **3.1 Determination Of BP CO By ARPRS**

The objective of this chapter is to investigate the thickness-dependent Raman intensity ratios between the characteristic peak of BP and that of the underlying Si

(100) substrate, which can then be used as a universal reference for further thickness determination.

However, since the anisotropic in-plane structure of BP will result in the orientation-dependent Raman response, the crystallographic orientations of the BP sample needs to be known first before measuring the Raman intensity ratios.

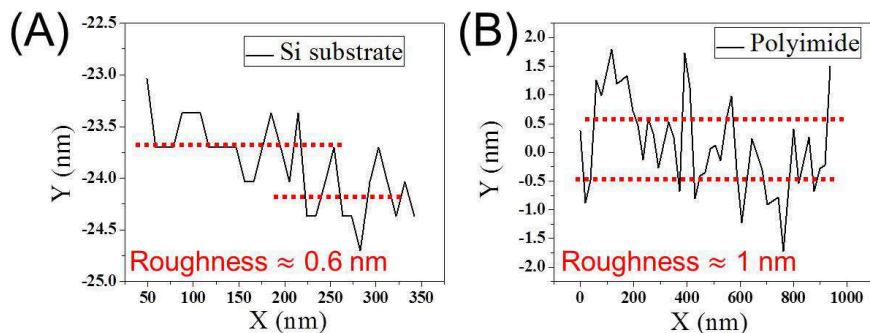
For the identifications of the crystallographic orientation (CO) of BP, angle-resolved conductance of BP sheet [16][59][62], diffraction pattern by high-resolution transmission electron microscope [19][46], optical absorption [59][19] and Angle-resolved Polarized Raman Spectroscopy (ARPRS) have been used to determine the in-plane CO of BP [16][18][62].

In consideration of the in-plane anisotropy and fast degradation of BP in air, developing a fast, convenient and non-contact method to determine the CO and thickness of BP has become necessary. ARPRS can serve as a solution to solve these two important problems. In addition, it has been widely used for studying the crystallography of many materials such as GaN [103], carbon nanotube [104], strained-graphene [105], etc.

## 3.2 Experiment Methods

In this work, first, the ARPRS results of a BP sample on Si (100) substrate by using the excitation wavelengths of 442 nm and 633 nm were compared; then by using the excitation wavelength of 442 nm under “parallel” configuration, the ARPRS measurements of 27 BP samples on 300-nm-thick SiO<sub>2</sub> / Si substrates and on 100- $\mu$ m-thick polyimide substrates prepared by sublimation thinning and mechanical exfoliation were performed, with the thickness range of 15 - 195 nm ( 10 to 200 nm ) for samples on SiO<sub>2</sub> / Si (polyimide) substrate.

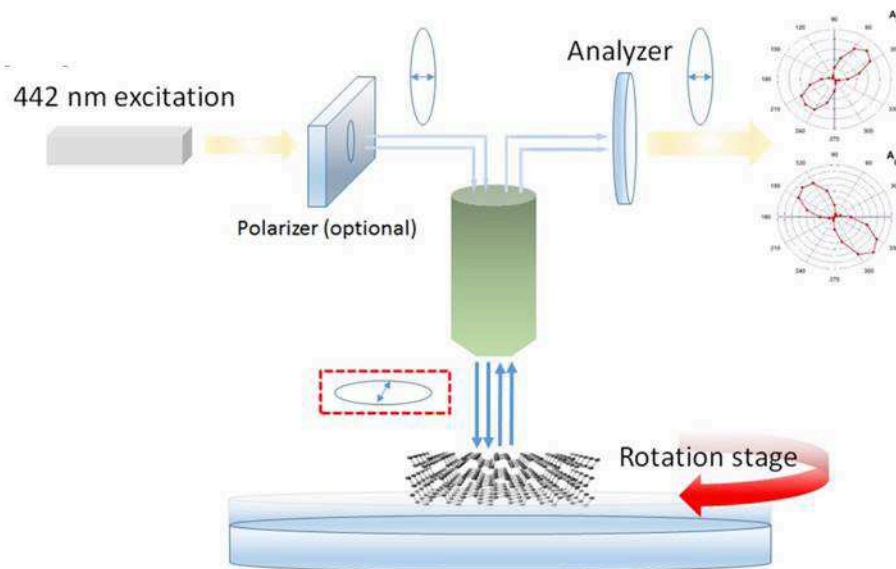




**Figure 3.1:** (A): AFM profile of a blank Si wafer, which indicates its roughness to be  $\sim 0.6$  nm; (B): AFM profile of a blank polyimide wafer, which indicates its roughness to be  $\sim 1$  nm;

### 3.2.1 Sample Preparation

BP flakes were first mechanically exfoliated from bulk BP crystals (99.998 %, Smart Elements, Vienna, Austria) in a glove box and transferred to a pre-cleaned Si (100) wafer (4 inch, 0.56 mm thick) with a 300-nm-thick  $\text{SiO}_2$  layer and a piece of 100- $\mu\text{m}$ -thick polyimide film (DuPont<sup>TM</sup> Kapton HN general-purpose film. In Fig 3.1 (A) and (B), the surface roughness of  $\text{SiO}_2$  / Si (polyimide) from the line-scan AFM results was around 0.3 nm (1 nm). The wafer and polyimide were then cut into small pieces (3 mm  $\times$  3 mm). In order to prepare thin BP flakes with various thickness less than 50 nm, thermal thinning (the samples would be heated at 230  $^\circ\text{C}$ , see the methods in Chapter 2) were performed on some exfoliated BP flakes. In this study, those BP samples on  $\text{SiO}_2$  / Si with thickness less than 45 nm were prepared by thermal sublimation. The BP samples on polyimide substrate with the thickness of: 10 - 40 nm, 58 - 70 nm and 85 nm were prepared by the thermal sublimation method.



**Figure 3.2:** Illustration of ARPRS experiment setup: the optical path of the Raman system under “parallel” configuration.

### 3.2.2 Angle-resolved Polarized Raman Spectroscopy (ARPRS)

In Fig 3.3 (A) & (B), the experimental setup was illustrated: typically, the BP was placed in the center of a rotation stage mounted on the motorized stage under the objective lens; the Raman spectra were collected by using a backscattered Horiba Jobin Yvon HR800 Raman system with the excitation wavelength of 442 / 633 nm (2.81 eV / 1.95 eV ) from the He - Cd / He - Ne laser. The 442 / 633 nm incident laser beam was polarized, and a polarization analyzer was placed in parallel “configuration” (incidence and scattering light are parallel) between the notch filter and the entrance of the CCD detector [16]. In this work, all ARPRS experiments were conducted under the “parallel” configuration following previous works [18][16][106]. BP samples were rotated clockwise for  $360^\circ$  in 24 steps ( $15^\circ$ /step). The angle values of the polar diagrams were angle readings of the rotation stage. During every step, Raman measurement was performed at the same point on each sample to ensure the consistency of results. The grating number of

detector was set as 2400 and the spectral range from 250 / 300 to 600 / 600  $\text{cm}^{-1}$  for the excitation wavelength of 442 / 633 nm. The spectral resolution before fitting was  $\approx 0.27 / 0.09 \text{ cm}^{-1}$  for the excitation wavelength of 442 / 633 nm. Hereafter, considering that polyimide substrate was damaged by 442 laser without reducing its power (around  $2 \text{ mW} / \mu\text{m}^2$ ), filter  $D = 1$  was then chosen in all ARPRS experiments in this work. This lowered the laser power by 10 times (around  $0.2 \text{ mW} / \mu\text{m}^2$ ) in order to avoid damage on both the samples and polyimide substrate. For excitation wavelength of 633 nm, filter  $D = 0.3$  was selected. The acquisition time and accumulation times were optimized at 3 sec and  $\times 2$  for both 442 and 633 nm lasers in order to enhance the Raman signals of BP samples as well as minimize laser damage to BP samples.

### 3.2.3 Atomic Force Microscopy (AFM)

AFM measurements were performed using the contact mode by an Asylum Research Molecular Force Probe 3D atomic force microscope and a Bruker Atomic Force Microscopy System.

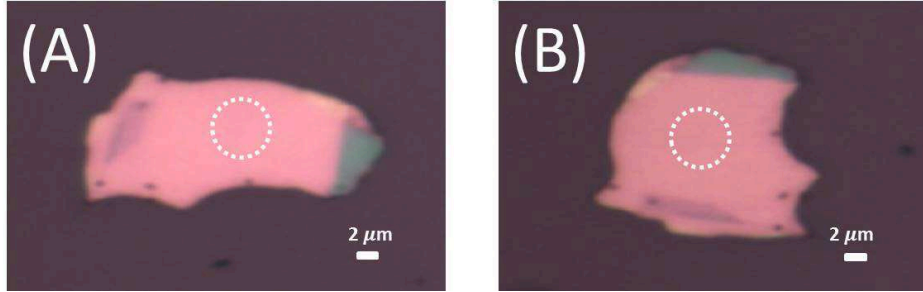
## 3.3 Results And Discussion

### 3.3.1 ARPRS Study In The Determination Of Crystallographic Orientation (CO) Of BP

#### Intensity Diagrams Of $A_g^1$ And $A_g^2$ Modes

First, ARPRS measurements with excitation wavelengths of 442 nm and 633 nm were performed on a thick BP flake on  $\text{SiO}_2 / \text{Si}$  substrate. In Fig 3.3, optical images showed the positions of the BP sample where  $A_g^1$  mode has maximum (Fig 3.3 (A)) and  $A_g^2$  (Fig 3.3 (B)) Raman intensities.

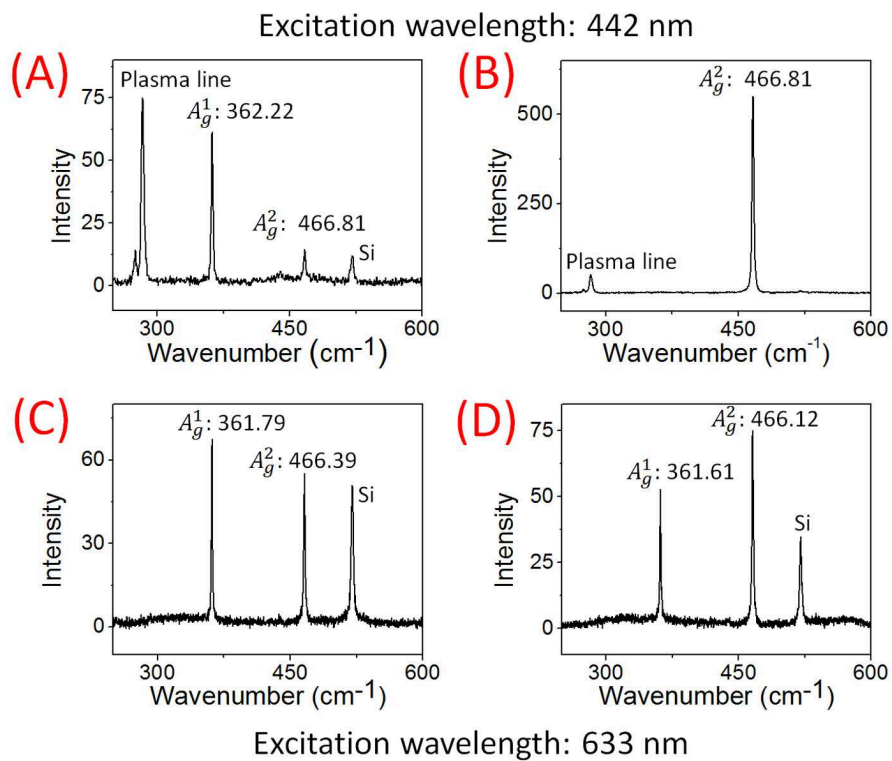
Let us look at the Raman spectra of the BP sample shown in Fig 3.4. In Fig 3.4, (A) / (C) and (B) / (D) are the Raman spectra of the sample shown in Fig 3.3



**Figure 3.3:** (A): Optical image of the BP sample on SiO<sub>2</sub> / Si substrate rotated at the position with maximum Raman intensity of A<sub>g</sub><sup>1</sup> mode and (B): at the position with the maximum Raman intensity of A<sub>g</sub><sup>2</sup> mode. The circled area indicates where the Raman spectra were collected;

(A) and (B), respectively, which were measured by using 442 / 633 nm excitation. In addition, (A) / (C) and (B) / (D) have maximum A<sub>g</sub><sup>1</sup> and A<sub>g</sub><sup>2</sup> Raman intensities.

In Fig 3.4 (A), the peak positions of the A<sub>g</sub><sup>1</sup> and the A<sub>g</sub><sup>2</sup> showed at 362.22 cm<sup>-1</sup> and 466.81 cm<sup>-1</sup>, respectively; A<sub>g</sub><sup>1</sup> reached its maximum Raman intensity while A<sub>g</sub><sup>2</sup> got a minimum Raman intensity; B<sub>2g</sub> disappeared and A<sub>g</sub><sup>2</sup> reached its minimum Raman intensity. The intensity counts of the A<sub>g</sub><sup>1</sup> and A<sub>g</sub><sup>2</sup> mode were ~ 130 and ~ 50, respectively. In Fig 3.4 (B), A<sub>g</sub><sup>2</sup> mode showed at 466.81 cm<sup>-1</sup> while A<sub>g</sub><sup>1</sup> became invisible, and notably, the intensity counts of the A<sub>g</sub><sup>2</sup> mode was increased to ~ 1100, which was more than 20 times of that shown in Fig 3.4 (A). However, for the excitation wavelength of 633 nm, in Fig 3.4 (C) and (D), maximum and minimum Raman intensities of A<sub>g</sub><sup>1</sup> (A<sub>g</sub><sup>2</sup>) modes were ~ 70 (~ 75) and ~ 55 (~ 50), which showed no apparent differences in comparison with those from Raman spectra acquired by the 442 nm laser.



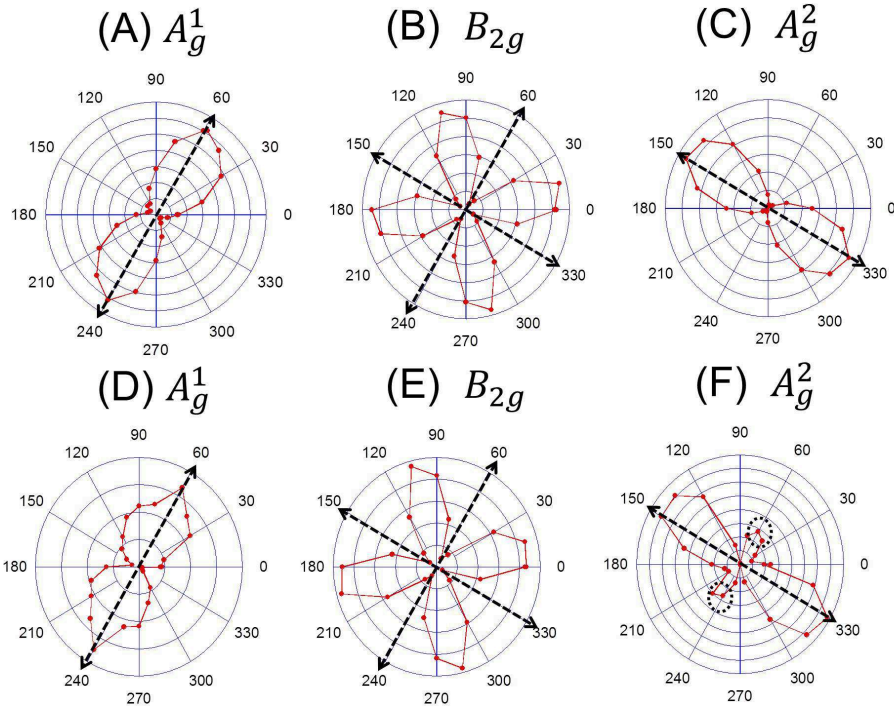
**Figure 3.4:** (A) & (C): Raman spectra of the BP sample on SiO<sub>2</sub> / Si substrate shown in Fig 3.3 (A), in which the A<sub>g</sub><sup>1</sup> mode showed maximum Raman intensity; (B) & (D): Raman spectra of the BP sample shown in Fig 3.3 (B), in which the A<sub>g</sub><sup>1</sup> mode showed maximum Raman intensity. Raman measurements shown in (A) & (B) were performed using the excitation wavelength of 442 nm while those in (C) & (D) were by 633 nm.

Then in Fig 3.5 (A) to (C) / (D) to (F), the intensity polar diagrams were used to demonstrate the ARPRS results acquired by using 442 / 633 nm laser. For the excitation wavelength of 442 nm, in Fig 3.5 (A), the Raman intensity polar diagram of  $A_g^1$  mode showed its maximum Raman intensity at  $165^\circ$  and  $345^\circ$  of sample rotation angle (labelled by double-head arrows); in Fig 3.5 (C), maximum Raman intensities of  $A_g^2$  appeared at  $75^\circ$  and  $255^\circ$  of the rotation angle. For the excitation wavelength of 633 nm, though the variation of  $A_g^1$  mode was similar to that from the results of 442 nm excitation, but the change of  $A_g^2$  mode was different from that measured by 442 nm laser, in that when  $A_g^1$  reached its maximum Raman intensity,  $A_g^2$  mode reached a relative smaller maximum Raman intensity instead of a minimum shown in Fig 3.5 (C). In addition, for both 442 and 633 nm excitation, the  $B_{2g}$  mode was invisible when the  $A_g^1$  or  $A_g^2$  mode reached its maximum Raman intensity.

As discussed above in section 1.3.3 (Page 35), under parallel configuration,  $B_{2g}$  mode was always forbidden when the incident laser was parallel to either zigzag or armchair direction. Therefore, according to Fig 3.5, the rotation angles  $\alpha$  showing at  $60^\circ / 240^\circ$  and  $150^\circ / 330^\circ$  indicated the two axes of BP (the zigzag and armchair directions, and in our work, the definition of zigzag direction as the “main axis” [19]) was followed.

It is suggested that the ARPRS results acquired by 633 nm laser could not provide simple and fast distinguishment of the zigzag and armchair directions from these two axes. The reason could be explained that according to the ARPRS of this work shown in Fig 3.5 (D) - (F), and previous works [18][19], the relative larger / smaller local maximum Raman intensity of  $A_g^2$  mode could appear at the angle either perpendicular or parallel to the angle of the maximum  $A_g^1$  Raman intensity, which made it infeasible for the determination of the CO of BP simply from at which angle the  $A_g^1$  and  $A_g^2$  modes had maximum and minimum Raman intensities.

Excitation wavelength: 442 nm



Excitation wavelength: 633 nm

**Figure 3.5:** ARPRS results with 442 nm excitation: (A): the polar diagram of  $A_g^1$  mode; (B): the polar diagram of  $B_{2g}$  mode; (C): the polar diagram of  $A_g^2$  mode. ARPRS results with 633 nm excitation: (D): the polar diagram of  $A_g^1$  mode; (E): the polar diagram of  $B_{2g}$  mode; (F): the polar diagrams of  $A_g^2$  mode. The arrows in figures indicate the two axes of BP (zigzag and armchair).

But for 442 nm excitation, according to the ARPRS results shown in Fig 3.4 (A) & (B) and Fig 3.5 (A) - (C) of this work and previous work [18], ARPRS with 442 nm excitation could be able to tell the CO of BP in that: 1. both intensity polar diagrams of  $A_g^1$  and  $A_g^2$  modes showed clear bow - tie shapes instead of elliptical / circular / peanut shapes, which made the angles of maximum and minimum Raman intensities more readable; 2. the maximum and minimum Raman intensities of  $A_g^1$  and  $A_g^2$  modes always appeared in orthogonal directions explicitly; 3. when incident polarization was parallel to armchair direction, the Raman intensity of  $A_g^2$  mode was dozens of times of that measured when incident polarization was parallel to zigzag direction.

Though Kim et al. [18] proposed the effectiveness of ARPRS with 442 nm excitation in CO determination of BP, the data were limited for only 4 samples; in addition, though Ling et al. [19] systematically studied the thickness-dependent ARPRS of BP by using 532, 633 and 785 nm excitation and pointed out their ARPRS results couldn't well indicate the CO of BP, they didn't investigate the thickness-dependent ARPRS of BP using 442 nm excitation. Overall, using ARPRS with 442 nm excitation for CO determination of BP has not been widely accepted.

In order to reveal this effectiveness of CO determination of BP by ARPRS with excitation wavelength of 442 nm, investigations of BP in a wide range of thickness were conducted: 11 and 16 BP samples with thickness ranging from 10 to 200 nm on  $\text{SiO}_2$  / Si and polyimide substrates were prepared. ARPRS studies by 442 nm laser were performed on those samples. All the results (See Table 3.2 to Table 3.5) were consistent with the Raman spectra shown in Fig 3.4 and the polar diagrams shown in Fig 3.5.

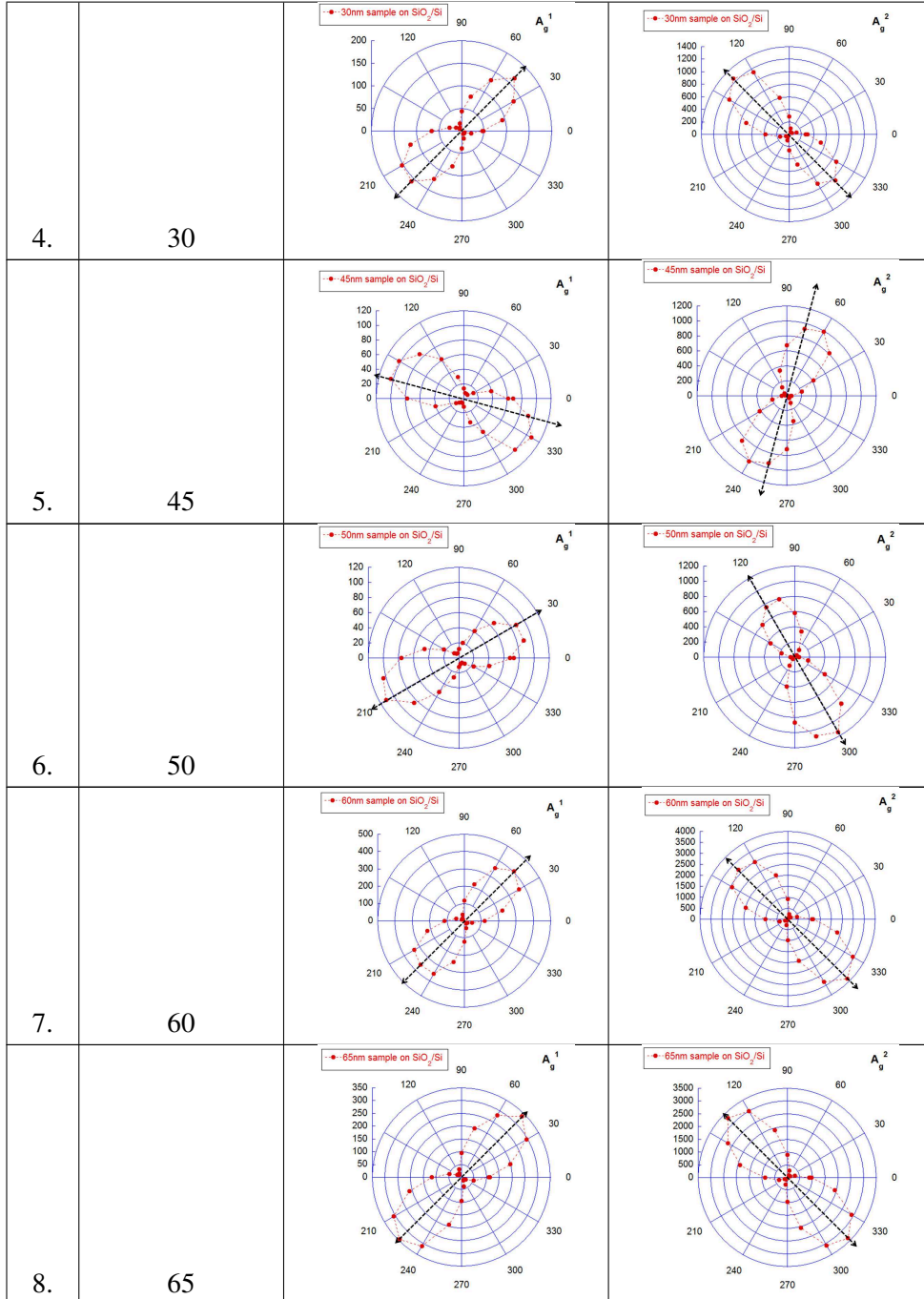
Therefore, with expanded thickness ranges and the addition of polyimide substrates, it could be concluded that, with the excitation wavelength of 442 nm, the CO identification (zigzag and armchair directions) agrees with previous work [16][18][62]: in a polar diagram, the direction along which the maximum Raman peak intensity of  $A_g^1$  was obtained is always perpendicular to the direction for the maximum  $A_g^2$  peak intensity. No thickness dependence was obtained, which meant

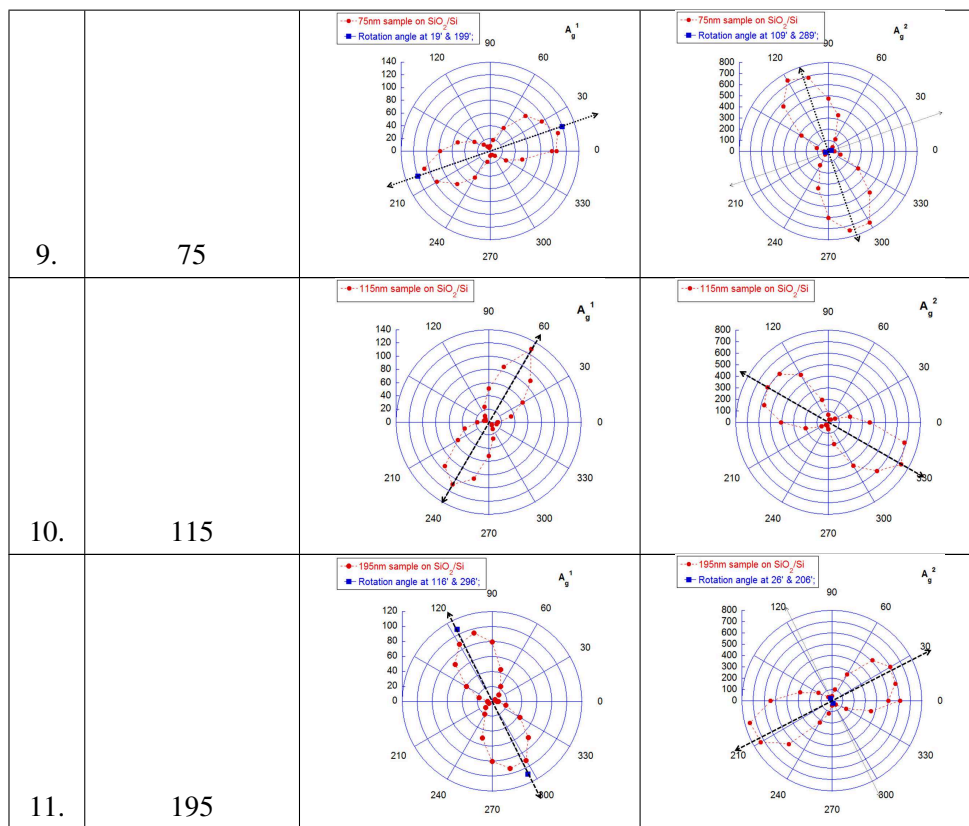


that the CO determination by ARPRS using 442 nm excitation could be conducted regardless of the BP thickness. Additionally, the fact that  $A_g^2$  Raman intensity measured at armchair direction are enhanced to be 10 - 100 times of that measured at zigzag direction, could be attributed to the resonance Raman effect. Therefore, more investigations should be conducted to study the conditions of this orientation-dependent resonance Raman effect of BP in the future.

• 1. Polar diagrams of ARPRS results: 11 samples on  $SiO_2 / Si$  substrates

No.	Thickness (nm)	Polar diagram of $A_g^1$ mode	Polar diagram of $A_g^2$ mode
1.	15		
2.	20		
3.	25		

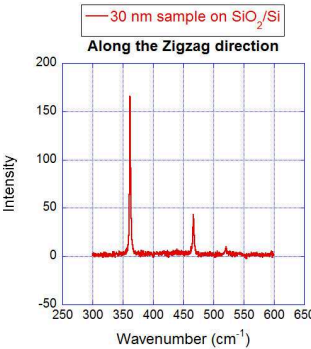
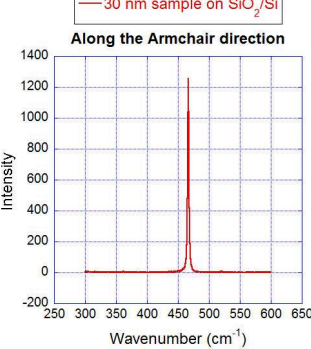
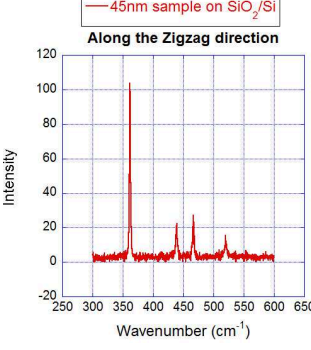
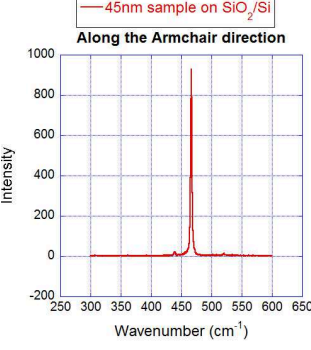
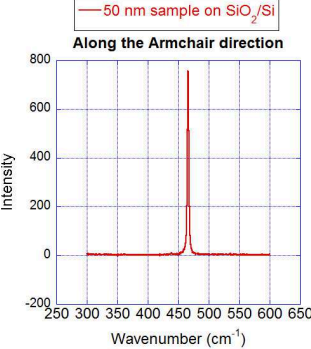


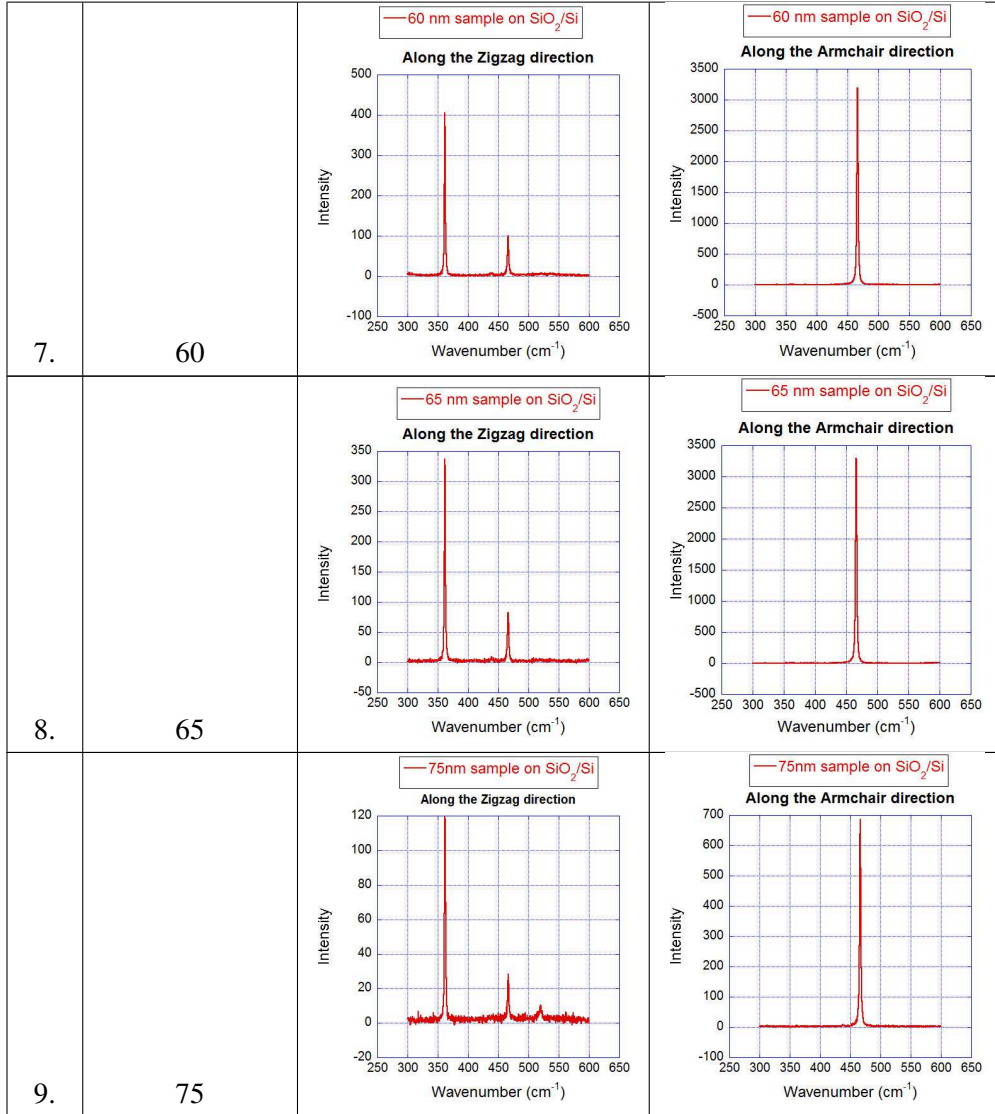


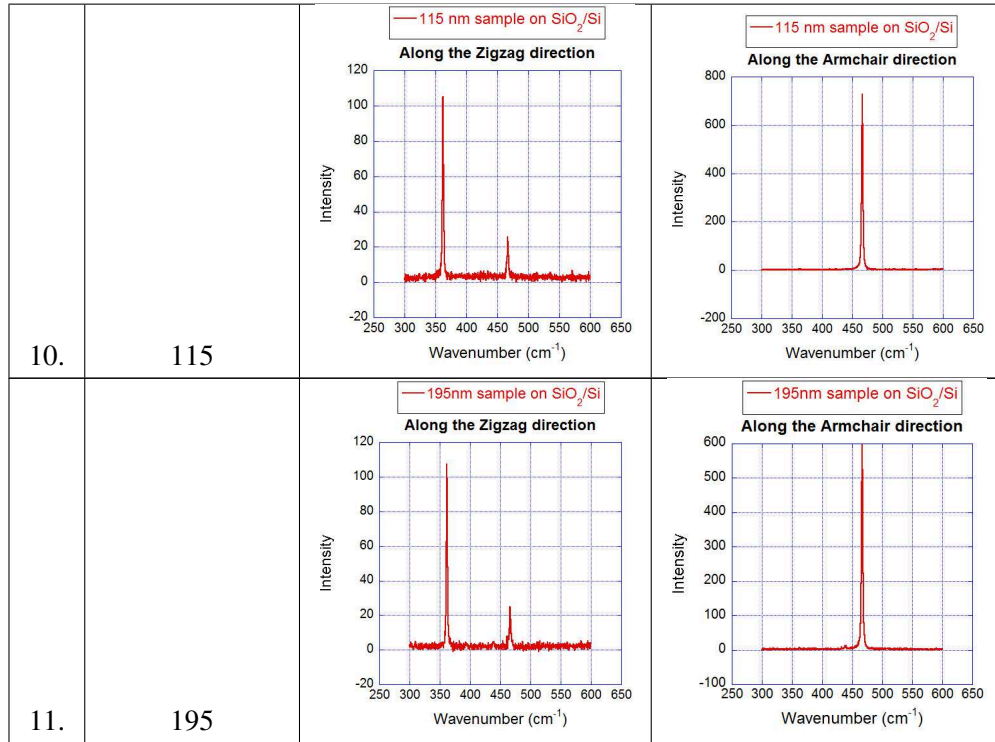
**Table 3.1:** Polar diagrams of peak intensity ratios of  $A_g^1$  over  $A_g^2$  of 11 BP samples on  $\text{SiO}_2 / \text{Si}$  substrates acquired by Angle-resolved Polarized Raman Spectroscopy (ARPRS).

• 2. Raman spectra of ARPRS results: 11 samples on SiO<sub>2</sub> / Si substrates

No.	Thickness (nm)	Raman profile: maximum A <sub>g</sub> <sup>1</sup> mode intensity	Raman profile: maximum A <sub>g</sub> <sup>2</sup> mode intensity
1.	15	<p>— 15 nm sample on SiO<sub>2</sub>/Si Along the Zigzag direction</p>	<p>— 15 nm sample on SiO<sub>2</sub>/Si Along the Armchair direction</p>
2.	20	<p>— 20nm sample on SiO<sub>2</sub>/Si Along the Zigzag direction</p>	<p>— 20 nm sample on SiO<sub>2</sub>/Si Along the Armchair direction</p>
3.	25	<p>— 25 nm sample on SiO<sub>2</sub>/Si Along the Zigzag direction</p>	<p>— 25 nm sample on SiO<sub>2</sub>/Si Along the Armchair direction</p>

4.	30	 <p>— 30 nm sample on SiO<sub>2</sub>/Si Along the Zigzag direction</p>	 <p>— 30 nm sample on SiO<sub>2</sub>/Si Along the Armchair direction</p>
5.	45	 <p>— 45nm sample on SiO<sub>2</sub>/Si Along the Zigzag direction</p>	 <p>— 45nm sample on SiO<sub>2</sub>/Si Along the Armchair direction</p>
6.	50		 <p>— 50 nm sample on SiO<sub>2</sub>/Si Along the Armchair direction</p>



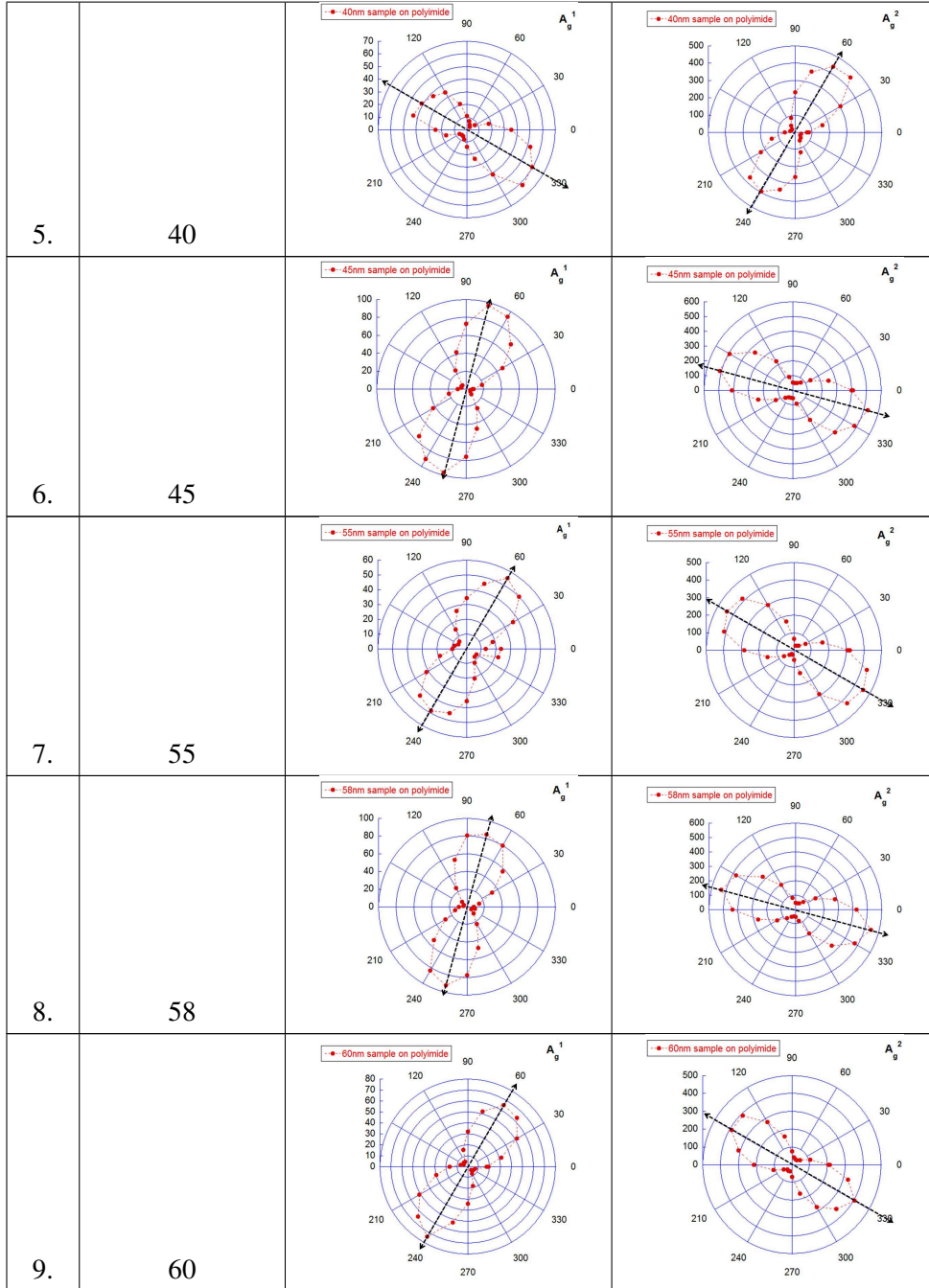


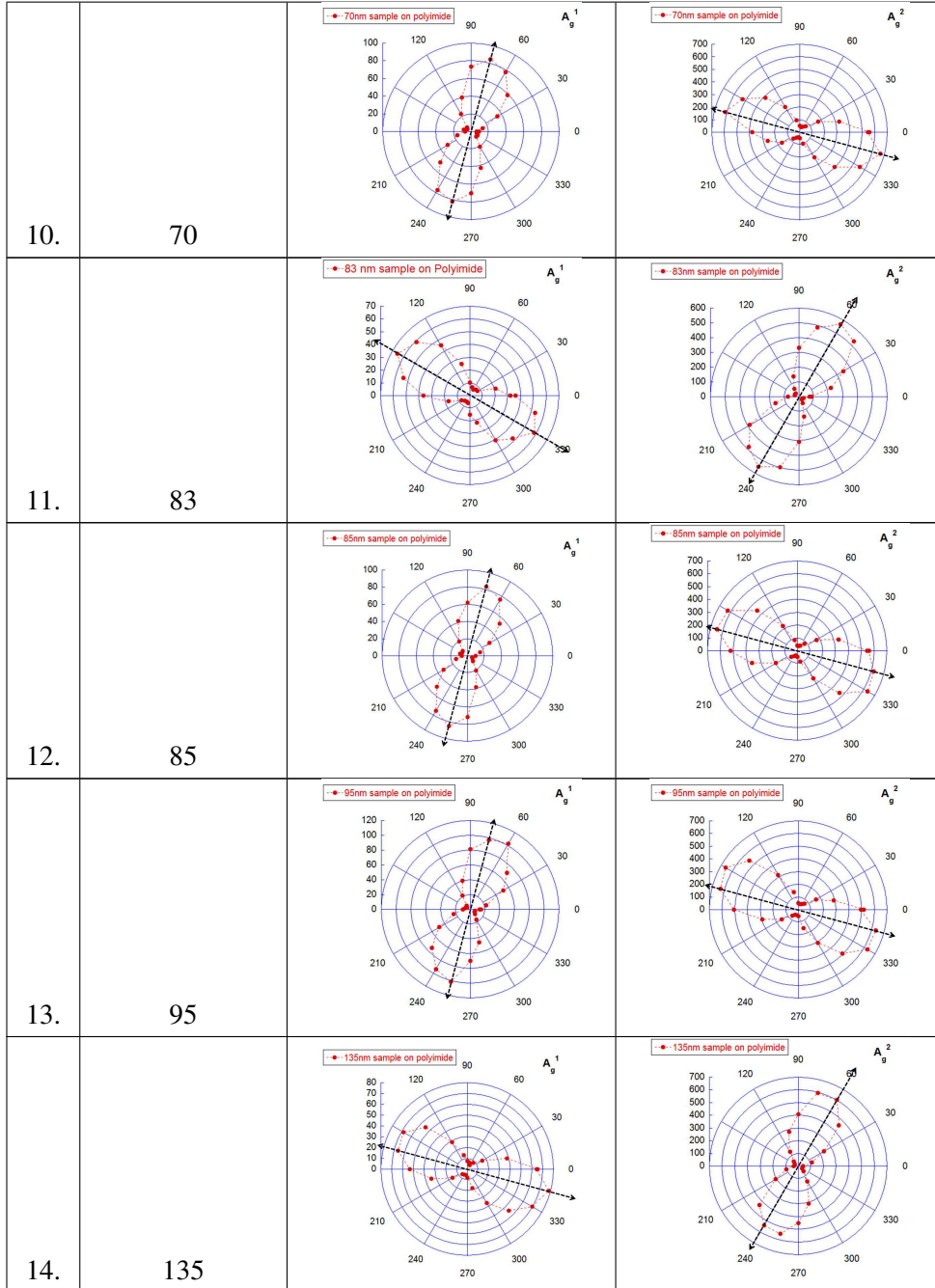
**Table 3.2:** Raman spectra: with maximum  $A_g^1 / A_g^2$  Raman intensities.

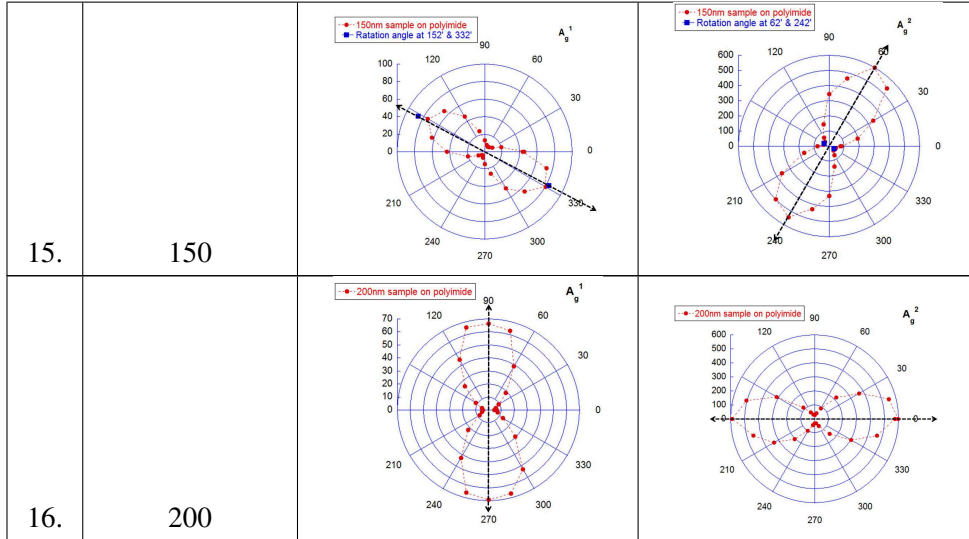
• 3. Polar diagrams of ARPRS results: 16 samples on polyimide substrates

No.	Thickness (nm)	Polar diagram of $A_g^1$ mode	Polar diagram of $A_g^2$ mode
1.	10		
2.	20		
3.	25		
4.	30		



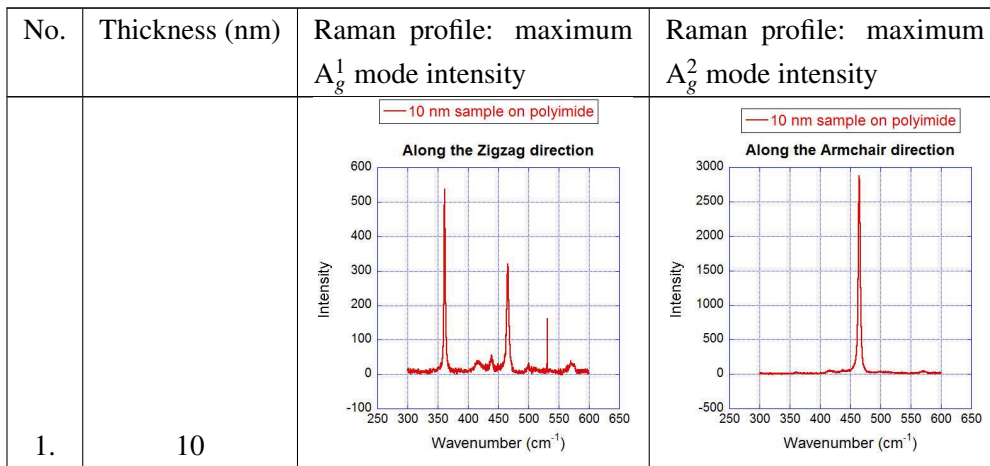


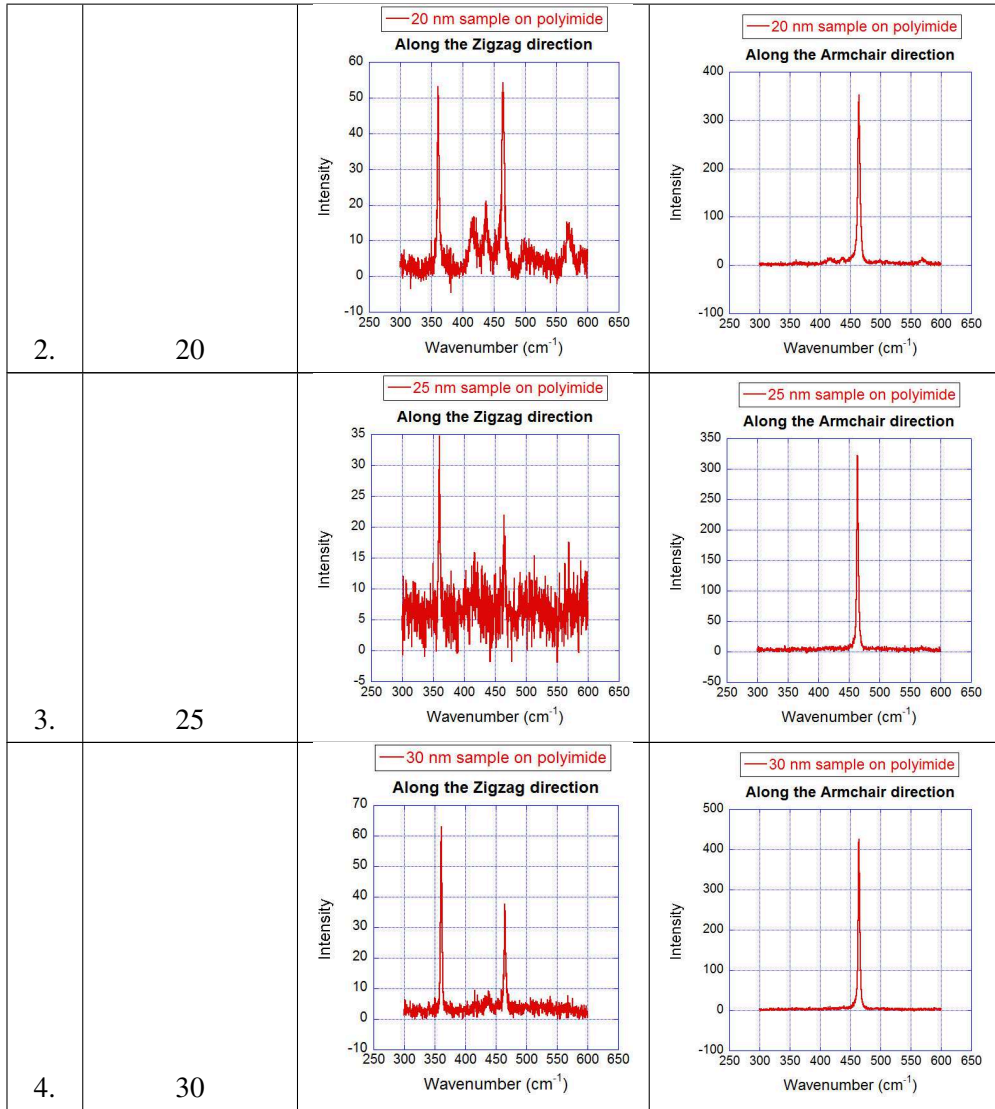


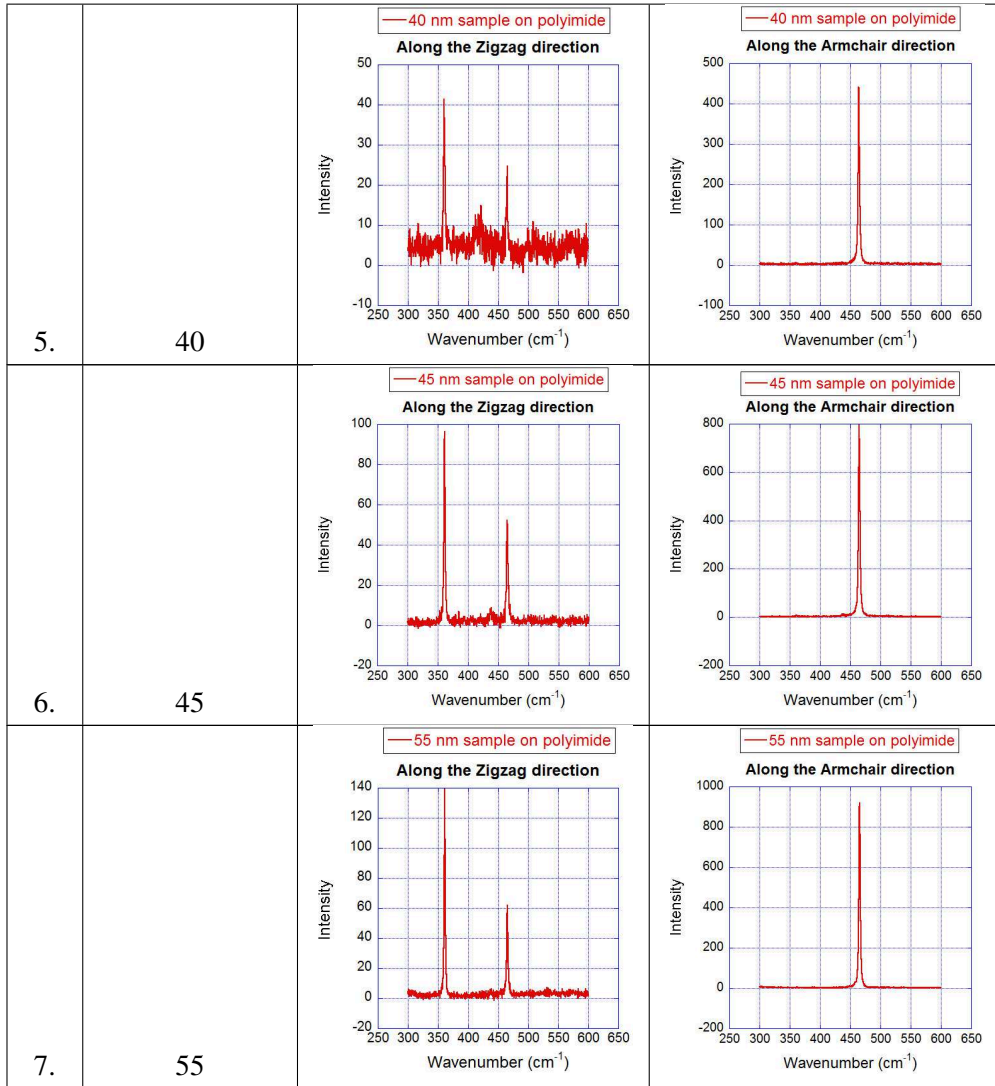


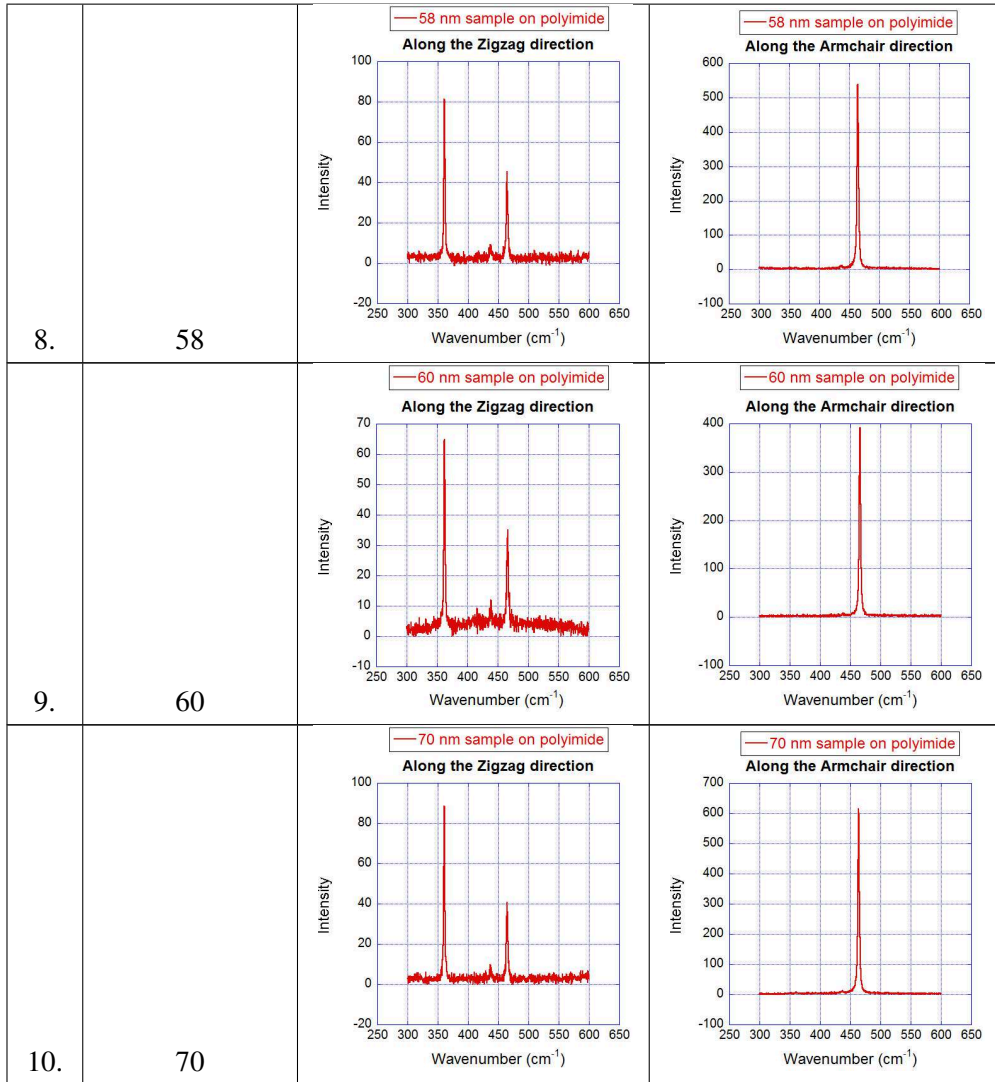
**Table 3.3:** Polar diagrams of 16 BP samples on polyimide substrates acquired by Angle-resolved Polarized Raman Spectroscopy (ARPRS).

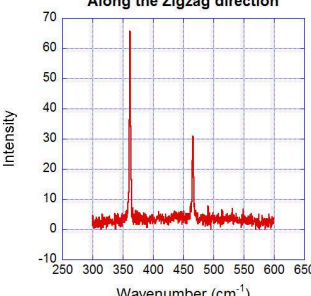
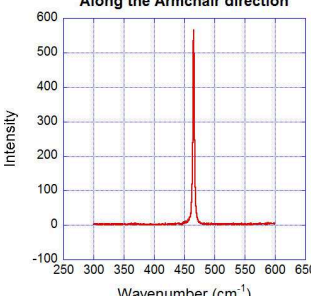
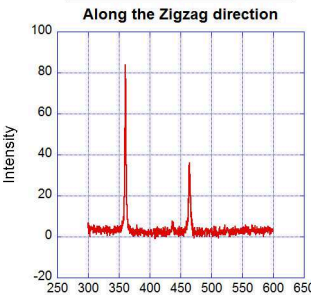
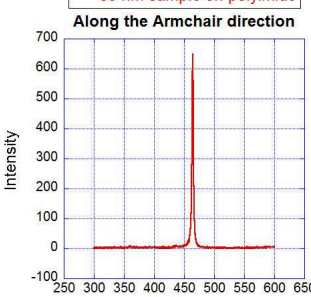
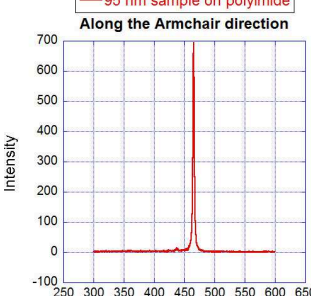
• **4. Raman spectra of ARPRS results: 16 samples on polyimide substrates**

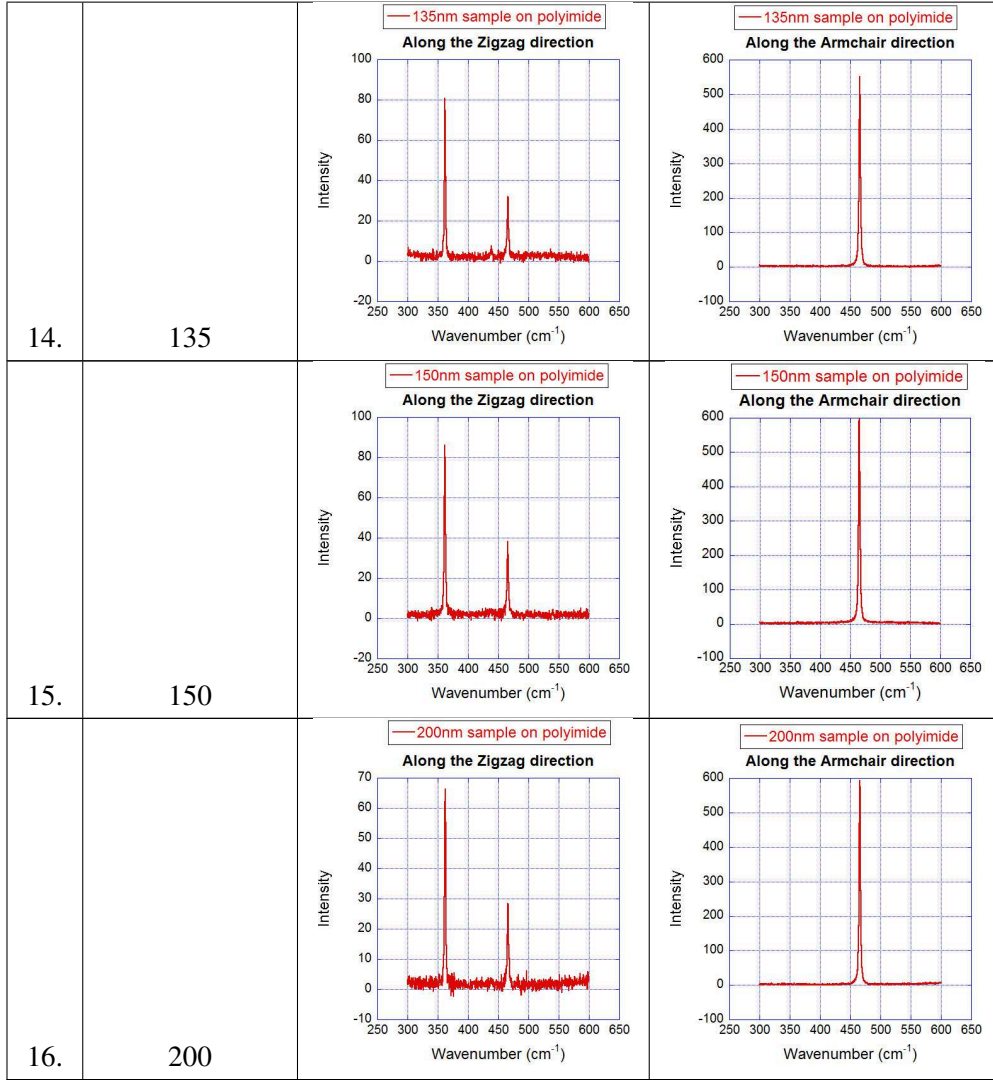








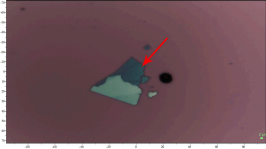
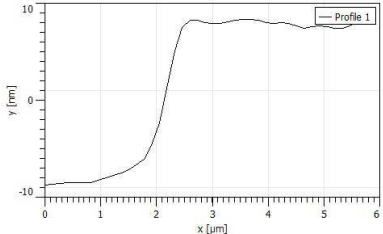
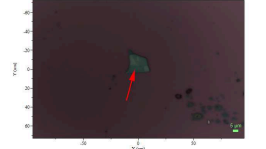
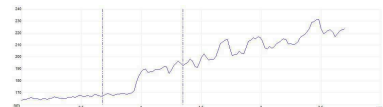
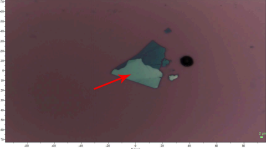
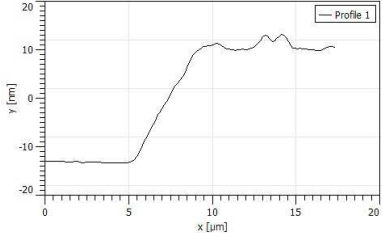
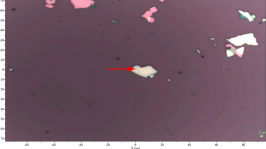

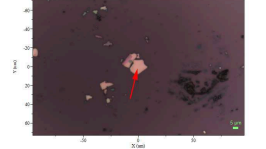
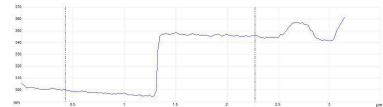
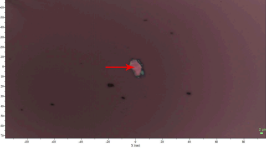

11.	83	<p>— 83nm sample on polyimide</p> <p><b>Along the Zigzag direction</b></p> 	<p>— 83nm sample on polyimide</p> <p><b>Along the Armchair direction</b></p> 
12.	85	<p>— 85 nm sample on polyimide</p> <p><b>Along the Zigzag direction</b></p> 	<p>— 85 nm sample on polyimide</p> <p><b>Along the Armchair direction</b></p> 
13.	95		<p>— 95 nm sample on polyimide</p> <p><b>Along the Armchair direction</b></p> 

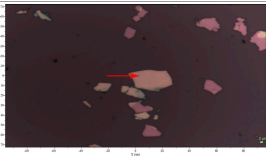
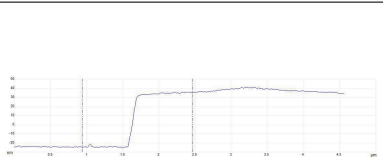
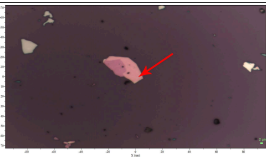
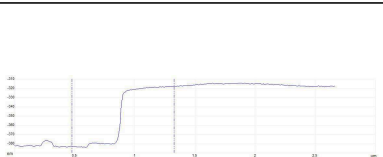
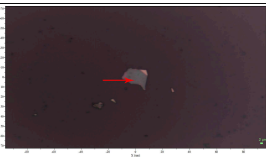

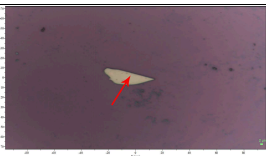
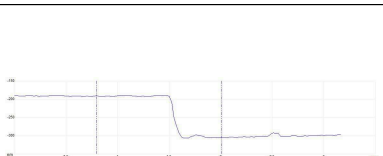

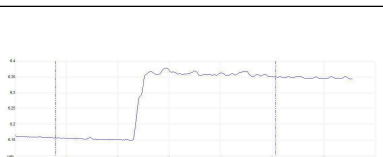


**Table 3.4:** Raman spectra: with maximum  $A_g^1 / A_g^2$  Raman intensities.



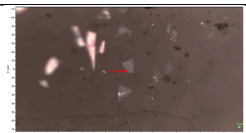
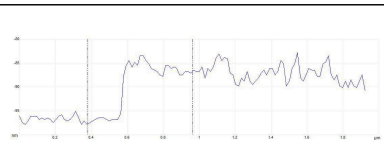

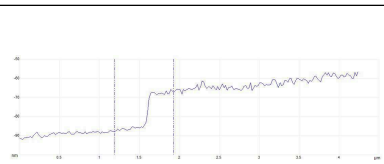

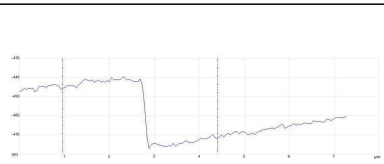

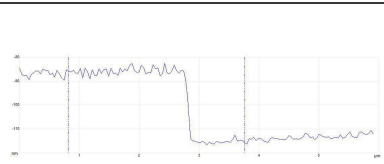

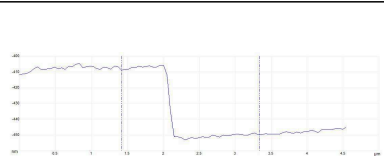
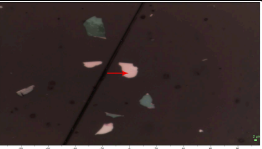


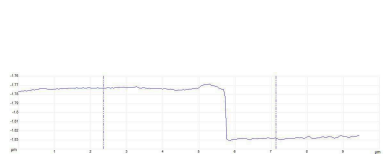
• 5. AFM data of BP samples on Si (100) wafer

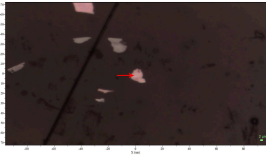
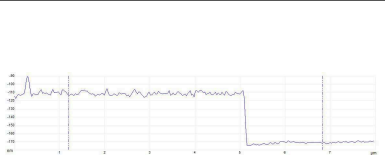
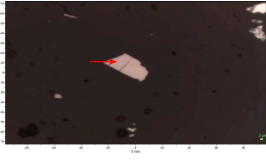
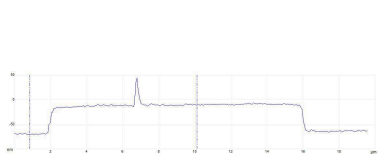
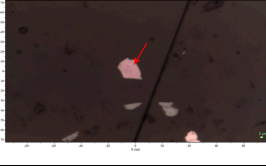

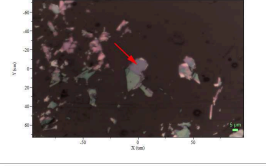
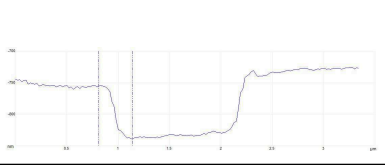
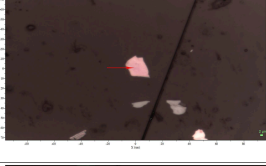
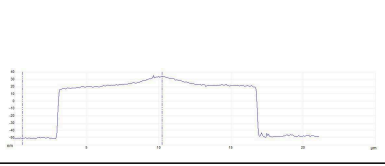
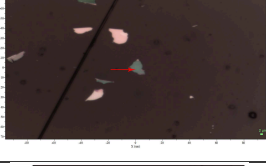
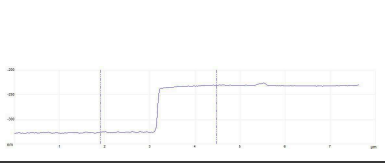
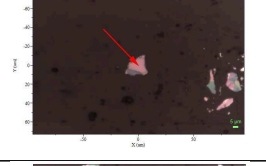
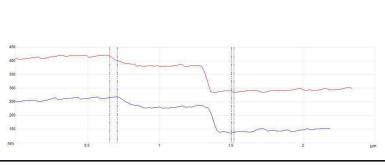
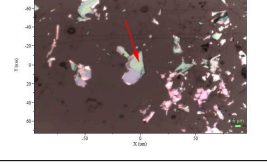
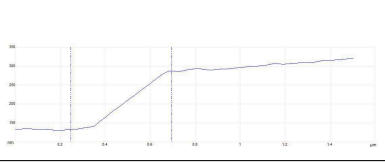
No.	Thickness	Optical image	AFM profile
1.	15 nm		
2.	20 nm		
3.	25 nm		
4.	30 nm		
5.	45 nm		
6.	50 nm		



7.	60 nm		
8.	65 nm		
9.	75 nm		
10.	115 nm		
11.	195 nm		

**Table 3.5:** Optical images, AFM thickness profiles of 11 BP Samples on SiO<sub>2</sub>/Si substrate. No.1-5 were samples prepared by sublimation thinning; No.6-12 were samples prepared by exfoliation.

• 6. AFM data of BP samples on polyimide substrate

No.	Thickness	Optical image	AFM profile
1.	10 nm		
2.	20 nm		
3.	25 nm		
4.	30 nm		
5.	40 nm		
6.	45 nm		
7.	55 nm		

8.	58 nm		
9.	60 nm		
10.	70 nm		
11.	83 nm		
12.	85 nm		
13.	95 nm		
14.	135 nm		
15.	150 nm		

16.	200 nm		
-----	--------	---	--

**Table 3.6:** Optical images, AFM images and thickness profiles of 16 BP Samples on polyimide substrate. No.1-5, 8, 10 and 12 were samples prepared by sublimation thinning; No.6-7, 9, 11 and 13-16 were samples prepared by exfoliation.

### 3.3.2 Raman Peak Intensity Ratios: $\frac{I_{Si}}{I_{A_g^2}}$ As A Function Of BP Thickness

#### 3.3.2.1 Definitions Of “Off-axis” And “On-axis” Raman Intensity Ratios $\frac{I_{Si}}{I_{A_g^2}}$

After confirming the effectiveness of CO determination of BP by ARPRS with 442 nm excitation, let us focus on the Raman intensity ratios of  $\frac{I_{Si}}{I_{A_g^2}}$  as a universal method for BP thickness determination.

The ARPRS results in the last section revealed the fact that if the incident polarization is parallel to the “zigzag direction”,  $A_g^1$  mode can reach its maximum, and both  $A_g^1$  and Si peak can be seen, and if the incident polarization is parallel to the “armchair” direction,  $A_g^2$  mode can reach its maximum but the Si peak cannot be seen because of the enhancement of  $A_g^2$  Raman intensity.

Therefore, for investigations of thickness-dependent Raman intensity ratios, the Raman intensity ratio of  $\frac{I_{Si}}{I_{A_g^2}}$  was selected. Therefore, the samples should be rotated to have their “zigzag” directions to be parallel to the incident polarization.

Furthermore, for more accurate determination of the layer number N by using the Raman intensity ratio of  $\frac{I_{Si}}{I_{A_g^2}}$ , it is expected to have as large Raman intensity of underlying Si (100) substrate as possible. Thus, it is always expected to rotate the Si (100) wafer to make the (100) plane also be parallel to the incident polarization

to have maximum Si Raman intensity  $I_{Si}$ . This situation is termed as “on-axis” which is very seldom.

It will be more often that the “zigzag” direction of BP and (100) plane of the underlying Si substrate are not both parallel to the incident polarization at the same time. This situation is termed as “off-axis” in this work.

When meeting the case of “off-axis”, the first step is to let the “zigzag” direction of BP be parallel to the incident polarization; then the measured Raman peak intensity from the underlying Si substrate and the rotation angle “ $\alpha$ ” at this moment are also recorded.

In the other side, the orientations of that Si substrate can be also measured by ARPRS directly at the blank area of this wafer. Therefore, the smallest angle difference between the rotation angle “ $\beta$ ” where the maximum blank Si Raman intensity appears and the zigzag direction of BP can be known. After that, because the orientation-dependent Raman intensity of Si (100) wafer is a sinusoidal function with a periodicity of  $90^\circ$  [91][92], the measured underlying Si Raman intensity can be then converted to that at the angle where the maximum blank Si Raman intensity appears according that known smallest angle difference.

Through this method, the “off-axis” underlying Si Raman intensity can be then converted to “on-axis” underlying Si peak intensities. The conversion will help to realize the expected “on-axis” situation.

According to the in-situ high temperature Raman spectra in Fig 2.23 and Fig 2.25 of Chapter 2, the Si Raman intensity increased monotonically with decreasing BP thickness. Therefore, after the BP sample being rotated at the angle ( $\theta = 0^\circ$ ) where the incident polarization was parallel to its main axis of zigzag direction, for each BP thickness, there could be always a corresponding Raman intensity ratio  $\frac{I_{Si}}{I_{A_g^2}}$  between the  $A_g^2$  mode and underlying Si (100) substrate.

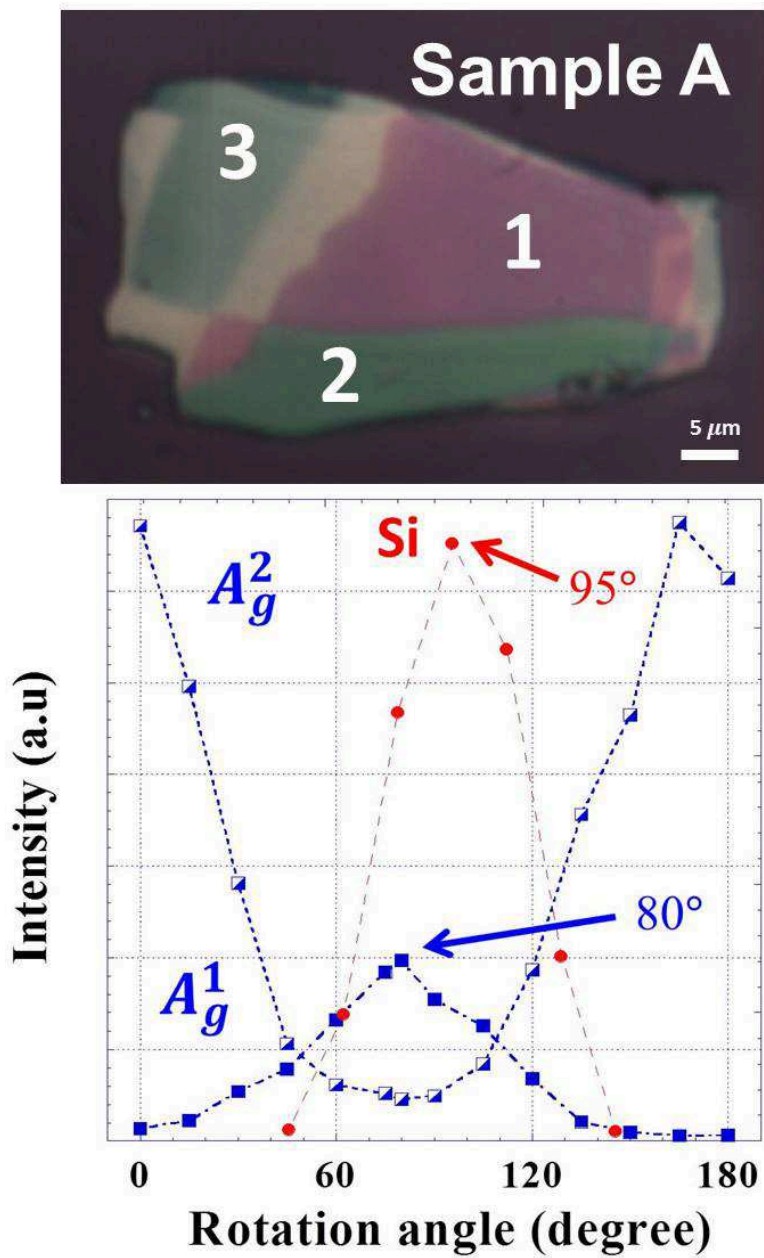
What's more, meeting the case of "off-axis" between the BP and underlying Si substrate, the ratio of  $\frac{I_{Si,\theta' \neq 0}}{I_{A_g^2}}$  could then be converted to the "on-axis"  $\frac{I_{Si,\theta' = 0}}{I_{A_g^2}}$  according to the smallest angle difference  $\theta'$ . As mentioned in Section 2.2.2 (P 68) of Chapter 2, Raman spectra were collected for each cycle of the periodic heating process on the sample A and B, and both "sample A" and "sample B" were measured to have a difference of  $15^\circ$  between the rotation angles of maximum  $A_g^1$  and Si intensity (Page 45). Therefore, the "on-axis" underlying Si Raman intensity should be twice of the measured underlying Si Raman intensity.

### 3.3.2.1 Results Of "Off-axis" And "On-axis" Raman Intensity Ratios $\frac{I_{Si}}{I_{A_g^2}}$

In this thesis work, the ARPRS measurements were performed on "Sample A" and "Sample B" before used for the interrupted heating experiments in Section 2.2.2 (P 65) of Chapter 2.

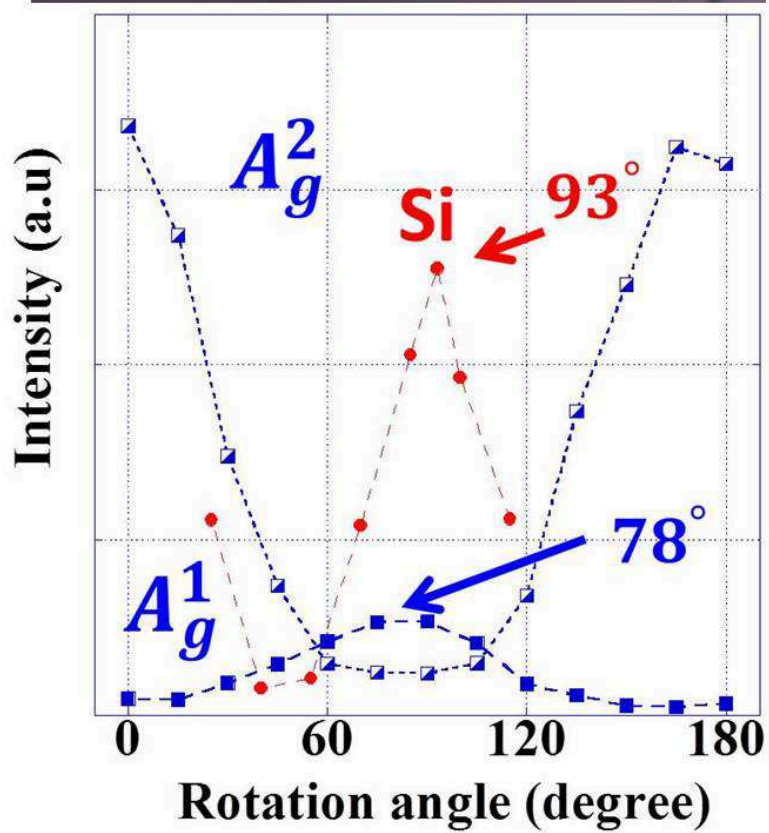
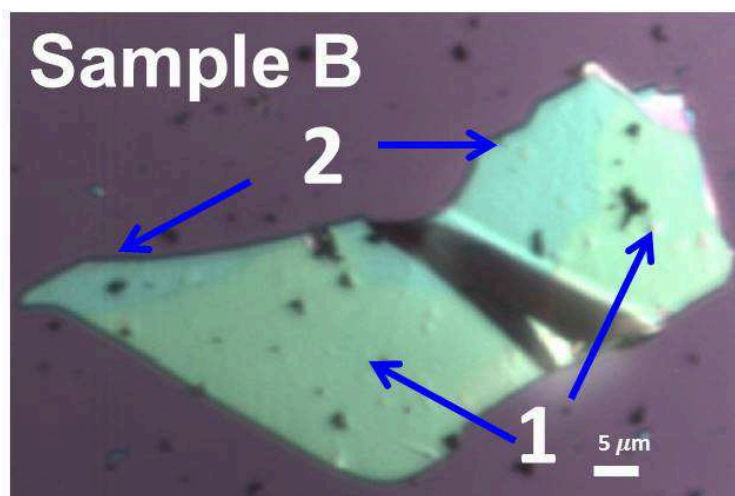
In Fig 3.6, the intensities of BP  $A_g^1$  and  $A_g^2$  modes as well as underlying Si (100) substrate of "Sample A" were plotted as functions of rotation angles. The rotation angles of maximum  $A_g^1$  and Si peak intensity showed that the smallest angle difference between the maximum Raman intensity of Si and that of BP  $A_g^2$  mode was  $15^\circ$ . Similarly, in Fig 3.7, those of "sample B" also showed a smallest angle difference of  $15^\circ$ . Thus, the two samples "Sample A" and "Sample B" met the "off-axis" case.

Since the smallest angle differences of "Sample A" and "Sample B" were both  $15^\circ$ , if converting this "off-axis" case to the "on-axis" case, the measured underlying Si Raman intensity should be 50% of the maximum underlying Si Raman intensity because of the sinusoidal function with a periodicity of  $90^\circ$  mentioned before.



**Figure 3.6:** “Sample A”. Raman intensities of  $A_g^1$  and  $A_g^2$  modes and underlying (100) Si wafer as functions of the rotation angle.





**Figure 3.7:** “Sample B”. Raman intensities of BP  $A_g^1$  and  $A_g^2$  modes and underlying Si(100) as functions of the rotation angle.

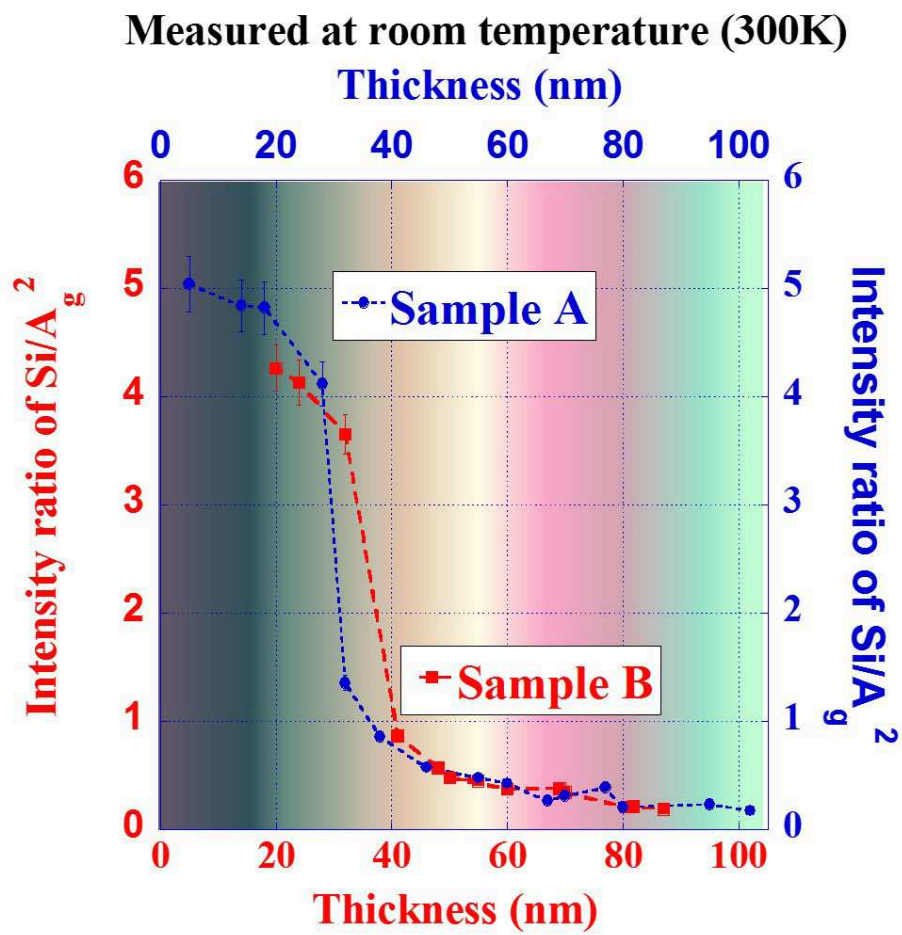
As mentioned before at the beginning of the “Interrupted Heating” experiments of Section 2.2.2 (P 65) in Chapter 2: for each heating cycle, 2 Raman spectra were taken before and after heating at room temperature respectively and 2 Raman spectra were collected at the beginning and ending of the heating process at high temperature; in the other side, the thicknesses of BP before and after each cycle were measured by AFM. Then the thickness-dependent Raman intensity ratios of  $\frac{I_{Si}}{I_{A_g^2}}$  from those measurements were plotted in Fig 3.9 and Fig 3.10.

In Fig 3.9, overall, the Raman intensity ratio of ( $\frac{I_{Si}}{I_{A_g^2}}$ ) increased monotonically with decreasing thickness, and the results from measurements at room temperature show that the two Raman intensity ratio -thickness curves of “Sample A” and “Sample B” agreed well, despite a minor disagreement at the data points between the 32-nm-sample of “Sample A” (blue solid circle) and the 32-nm-sample of “Sample B” (red solid cubic). This can be explained by 2 reasons:

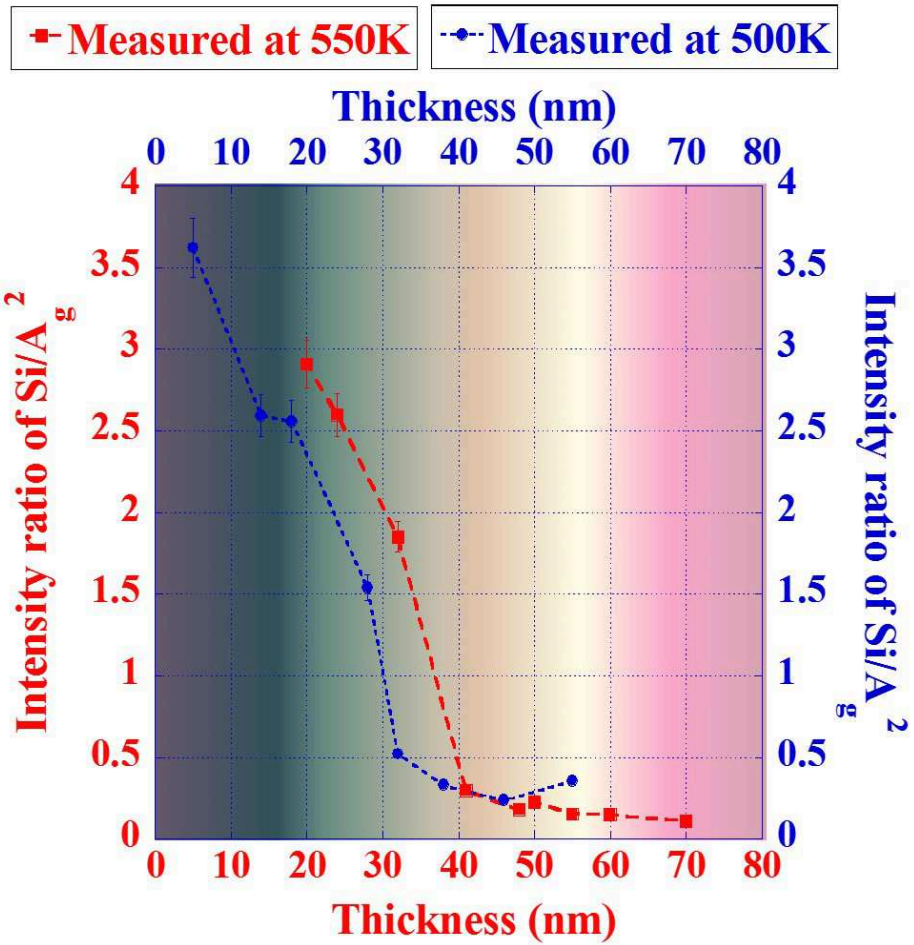
1. The experimental errors might be introduced by AFM measurements. In other words, the surface oxidation took place because of the frequent exposure in air ambient during AFM measurements, and with decreasing thickness, the oxidation proceeded faster [63], and then the measured thickness might be greater than the real thickness of prepared fresh sample. Therefore, the thickness of that 32-nm-thick data point of “Sample B” (red solid cubic) should be less than 32 nm.

2. Before this cycle of heating, the experimental errors might be caused by that the minor vibrations during the placement of “Sample A”, and then make the BP sample be a bit off the angle where its  $A_g^1$  mode have the maximum Raman intensity.

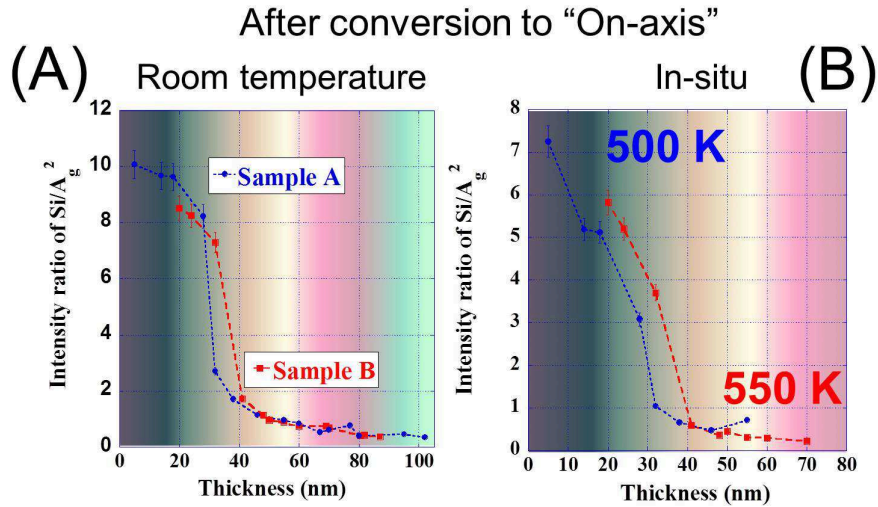
So far, the general agreement of those two profiles indicates that, for “off-axis” case between the BP sample and underlying Si substrate, with each definite smallest angle difference, there is always only one Raman intensity ratio of  $\frac{I_{Si}}{I_{A_g^2}}$  for each thickness.



**Figure 3.8:** Room temperature Raman intensity ratios of  $\frac{Si}{A_g^2}$  as a function of thickness measured by AFM, here the blue line represents the sample A and the red line represents sample B.



**Figure 3.9:** High temperature Raman intensity ratios of  $\frac{Si}{A_g^2}$  as a function of measured thickness, here the blue line represents sample A treated at 500 K and the red line represents sample B at 550 K.



**Figure 3.10:** High temperature Raman intensity ratios of  $\frac{I_{Si}}{I_{A_g^2}}$  as a function of measured thickness, here the blue line represents sample A treated at 500 K and the red line represents sample B at 550 K.

In addition, the high temperature thickness-dependent Raman intensity ratios  $\frac{I_{Si}}{I_{A_g^2}}$  of “Sample A” (measured at 500 K) and “Sample B” (measured at 550 K) were plotted in Fig 3.9. It is important to note that the thicknesses were from the AFM measurements at room temperature and the consideration of no thickness attenuation during the ramping-up and cooling-down process. These two profiles provide the capability of in-situ determining BP thickness at 500 K and 550 K respectively. After that, the “off-axis” Raman intensity ratios  $\frac{I_{Si}}{I_{A_g^2}}$  were then converted to the “on-axis” ones according to the smallest angle differences of  $15^\circ$  which were shown in Fig 3.10. Therefore, with known smallest angle difference between the maximum Raman intensity of  $A_g^1$  and that of the underlying Si substrate. The “on-axis” Raman intensity ratios of  $\frac{I_{Si}}{I_{A_g^2}}$  can always be achieved.

In general, for future purpose of non-contact, in and ex -situ, instant determination of the thickness during fabrication, the thickness-dependent Raman intensity ratios ( $\frac{I_{Si}}{I_{A_g^2}}$ ) can be served as a solution as long as enough references have been pro-

vided. That is to say, if the thickness-dependent Raman intensity ratios of  $(\frac{I_{Si}}{I_{A_g^2}})$  at many smallest angle differences are provided, this method can satisfy the purpose.

### 3.3.3 Conclusion:

To summarize, ARPRS measurements of 10 to 200 nm thick black phosphorus flakes on SiO<sub>2</sub> / Si and polyimide substrates by angle-resolved polarized Raman Spectroscopy were performed. The results revealed that ARPRS with 442 nm excitation and under parallel configuration can provide unambiguous, convenient, non-destructive and fast determination of the crystallographic orientation of BP. In addition, the Raman intensity ratio  $\frac{I_{Si}}{I_{A_g^2}}$  increases monotonically with decreasing thickness, which can serve as a non-contact optical method for determining thickness of BP both in-situ and ex-situ.

## Chapter 4

# Conclusion and outlook

### 4.1 Conclusion

As stated in Chapter 1, BP is promising for wide applications including thermal imaging, thermoelectronics, fibre-optic communications, photo-voltaics and digital / high frequency electronics. The controllable isolation of BP to atomically thin layers remains as one of the key challenges in current research. To develop a method for economic controllable growth of large scale, uniform and crystalline few-layer BP film is the main goal of this thesis.

This thesis present the experimental study in preparation and characterization of few-layer BP: 1. we achieved the successful and repeatable isolation of large few-layer crystalline BP by thermal thinning of thick BP flakes; 2. We revealed that Raman spectroscopy could be used as a powerful and versatile tool for: 1. clearly indentifying the CO of BP; 2. determining the instant thickness of BP in and ex-situ; 3. providing the crystallinity and uniformity information non-destructively.

We observed micro-scale thickness attenuation of BP at the high temperature by the color changes under the optical microscope. After the heating process, Raman mapping results demonstrate the size, uniformity and crystallinity of the BP samples retained, and indicate the thinning process of BP to be isotropic within the plane. Interrupted and continuous heating processes at 500 K and 550 K were per-

formed at BP samples. The AFM and Raman spectra results measured the thickness of BP before and after the heating process. The results indicate the thinning rates of BP at 500 K and 550 K were measured to be 0.15 nm / min and 2 nm / min from AFM results of BP samples before and after heating process. After that, AFM, Raman mapping and optical contrast demonstrated the successful and repeatable preparation of the large area ( $> 200 \mu\text{m}^2$ ), few-layer ( $< 5$  layers), crystalline BP by the thermal thinning method.

The Angle-resolved Polarized Raman Spectroscopy with the excitation wavelength of 442 nm measured the CO of BP: 1. both intensity polar diagrams of  $A_g^1$  and  $A_g^2$  modes showed clear bow - tie shapes instead of elliptical / circular / peanut shapes, which made the angles of maximum and minimum Raman intensities more readable; 2. the maximum and minimum Raman intensities of  $A_g^1$  and  $A_g^2$  modes always appeared in orthogonal directions explicitly; 3. when incident polarization was parallel to armchair direction, the Raman intensity of  $A_g^2$  mode was dozens of times of that measured when incident polarization was parallel to zigzag direction. After finishing CO identification, the sample was aligned to have maximum  $A_g^1$  Raman intensity, and then the Raman intensity ratio  $\frac{A_g^2}{A_g^1}$  and thickness of BP showed one-to-one correspondence, which indicated that, Raman spectroscopy can be used as a non-contact tool for in and ex -situ thickness measurement.

Overall, this work present the effectiveness of the thermal thinning method in preparing large, uniform, crystalline few-layer BP. This work also contributed to the development of the all-Raman method in controllable sublimation thinning of BP. This all-Raman method integrated the 3 major functions: 1. identification of CO of BP; 2. determination of the thickness of BP; 3. confirmation of the crystallinity and uniformity, which are the 3 critical steps of controllable thinning of BP.

## 4.2 Outlook

As an outlook for future studies, and by taking advantage of this work, 3 potential directions are suggested here in order to improve the fabrication technique,



study the basic properties like the electronic and optical properties of prepared few-layer BP, and explore its wide applications: 1. controllable preparation of large, uniform, crystalline few-layer BP on other substrates; 2. measurements of the angle or layer dependent transport properties such as the carrier mobility, the on-off ratio, resistivity and etc of BP-based devices; 3. by stacking with other 2D materials to form 2D van der Waals heterostructure, IR absorption then might gain significant enhancement, which might be promising for making wearable electronics and solar cells. In addition, more investigations also need to be conducted to: 1. the control of sublimation and the critical temperature of phase change and 2: study the conditions of resonance Raman effect of BP in the future.

# Bibliography

- [1] Lewis, E. A., Brent, J. R., Derby, B., Haigh, S. J. & Lewis, D. J. Solution processing of two-dimensional black phosphorus. *Chemical Communications* (2017). → pages ix, 16
- [2] Long, D. The raman effect: a unified treatment of the theory of raman scattering by molecules. 2002. *West Sussex, England: John Wiley & Sons Ltd* . → pages ix, xii, 28, 29, 30
- [3] Li, L., Yu, Y., Ye, G. J., Ge, Q., Ou, X., Wu, H., Feng, D., Chen, X. H. & Zhang, Y. Black phosphorus field-effect transistors. *Nature nanotechnology* **9**, 372–377 (2014). → pages x, xi, 1, 3, 4, 13, 14
- [4] Castellanos-Gomez, A. Black phosphorus: narrow gap, wide applications. *The journal of physical chemistry letters* **6**, 4280–4291 (2015). → pages x, 5, 6, 13
- [5] Lam, K.-T., Dong, Z. & Guo, J. Performance limits projection of black phosphorous field-effect transistors. *IEEE Electron Device Letters* **35**, 963–965 (2014). → pages x, 7, 8
- [6] Qiao, J., Kong, X., Hu, Z.-X., Yang, F. & Ji, W. High-mobility transport anisotropy and linear dichroism in few-layer black phosphorus. *Nature communications* **5** (2014). → pages x, 9, 10
- [7] Yuan, H., Liu, X., Afshinmanesh, F., Li, W., Xu, G., Sun, J., Lian, B., Curto, A. G., Ye, G., Hikita, Y. *et al.* Polarization-sensitive broadband photodetector using a black phosphorus vertical p–n junction. *Nature nanotechnology* **10**, 707–713 (2015). → pages x, 9, 10
- [8] Li, Y., Hu, Z., Lin, S., Lai, S. K., Ji, W. & Lau, S. P. Giant anisotropic raman response of encapsulated ultrathin black phosphorus by uniaxial strain. *Advanced Functional Materials* (2016). → pages xi, 11, 12

- [9] Liu, H., Neal, A. T., Zhu, Z., Luo, Z., Xu, X., Tománek, D. & Ye, P. D. Phosphorene: an unexplored 2d semiconductor with a high hole mobility. *ACS nano* **8**, 4033–4041 (2014). → pages xi, 14, 82
- [10] Sresht, V., Pádua, A. A. & Blankschtein, D. Liquid-phase exfoliation of phosphorene: design rules from molecular dynamics simulations. *ACS nano* **9**, 8255–8268 (2015). → pages xi, 15
- [11] Yasaei, P., Kumar, B., Foroozan, T., Wang, C., Asadi, M., Tuschel, D., Indacochea, J. E., Klie, R. F. & Salehi-Khojin, A. High-quality black phosphorus atomic layers by liquid-phase exfoliation. *Advanced Materials* **27**, 1887–1892 (2015). → pages xi, 15, 16
- [12] Lu, W., Nan, H., Hong, J., Chen, Y., Zhu, C., Liang, Z., Ma, X., Ni, Z., Jin, C. & Zhang, Z. Plasma-assisted fabrication of monolayer phosphorene and its raman characterization. *Nano Research* **7**, 853–859 (2014). → pages xi, 13, 17, 39, 50
- [13] Liu, X., Chen, K.-S., Wells, S. A., Balla, I., Zhu, J., Wood, J. D. & Hersam, M. C. Scanning probe nanopatterning and layer-by-layer thinning of black phosphorus. *Advanced Materials* (2016). → pages xi, 13, 18
- [14] Smith, J. B., Hagaman, D. & Ji, H.-F. Growth of 2d black phosphorus film from chemical vapor deposition. *Nanotechnology* **27**, 215602 (2016). → pages xi, 13, 19
- [15] Yang, Z., Hao, J., Yuan, S., Lin, S., Yau, H. M., Dai, J. & Lau, S. P. Field-effect transistors based on amorphous black phosphorus ultrathin films by pulsed laser deposition. *Advanced Materials* **27**, 3748–3754 (2015). → pages xi, 13, 20, 21, 22, 23
- [16] Wu, J., Mao, N., Xie, L., Xu, H. & Zhang, J. Identifying the crystalline orientation of black phosphorus using angle-resolved polarized raman spectroscopy. *Angewandte Chemie* **127**, 2396–2399 (2015). → pages xii, 24, 25, 34, 91, 93, 99
- [17] Ribeiro, H. B., Pimenta, M. A., de Matos, C. J., Moreira, R. L., Rodin, A. S., Zapata, J. D., de Souza, E. A. & Castro Neto, A. H. Unusual angular dependence of the raman response in black phosphorus. *ACS nano* **9**, 4270–4276 (2015). → pages xii, 24, 25
- [18] Kim, J., Lee, J.-U., Lee, J., Park, H. J., Lee, Z., Lee, C. & Cheong, H. Anomalous polarization dependence of raman scattering and

- crystallographic orientation of black phosphorus. *Nanoscale* **7**, 18708–18715 (2015). → pages xii, 24, 25, 26, 48, 66, 91, 93, 97, 99
- [19] Ling, X., Huang, S., Hasdeo, E. H., Liang, L., Parkin, W. M., Tatsumi, Y., Nugraha, A. R., Poretzky, A. A., Das, P. M., Sumpter, B. G. *et al.* Anisotropic electron-photon and electron-phonon interactions in black phosphorus. *Nano letters* **16**, 2260–2267 (2016). → pages xii, 24, 25, 27, 34, 48, 91, 97, 99
- [20] Tanaka, M. & Young, R. Review polarised raman spectroscopy for the study of molecular orientation distributions in polymers. *Journal of Materials Science* **41**, 963–991 (2006). → pages xii, 31
- [21] Graves, P., Gardiner, D. & Graves, P. Practical raman spectroscopy (1989). → pages xii, 31, 33, 34
- [22] Wu, J., Li, H., Yin, Z., Li, H., Liu, J., Cao, X., Zhang, Q. & Zhang, H. Layer thinning and etching of mechanically exfoliated mos2 nanosheets by thermal annealing in air. *Small* **9**, 3314–3319 (2013). → pages xiii, 39, 40
- [23] Huang, Y.-K., Cain, J. D., Peng, L., Hao, S., Chasapis, T., Kanatzidis, M. G., Wolverton, C., Grayson, M. & Dravid, V. P. Evaporative thinning: A facile synthesis method for high quality ultrathin layers of 2d crystals. *ACS nano* **8**, 10851–10857 (2014). → pages xiii, 39, 40
- [24] Lu, W., Zhang, Y., Zhu, Z., Lai, J., Zhao, C., Liu, X., Liu, J. & Sun, D. Thin tungsten telluride layer preparation by thermal annealing. *Nanotechnology* **27**, 414006 (2016). → pages xiii, 39, 40
- [25] Liu, X., Wood, J. D., Chen, K.-S., Cho, E. & Hersam, M. C. In situ thermal decomposition of exfoliated two-dimensional black phosphorus. *The Journal of Physical Chemistry Letters* **6**, 773–778 (2015). → pages xiii, 41, 53, 65
- [26] Fortin-Descheenes, M., Levesque, P. L., Martel, R. & Moutanabbir, O. Dynamics and mechanisms of exfoliated black phosphorus sublimation. *The journal of physical chemistry letters* **7**, 1667–1674 (2016). → pages xiii, 41, 53, 65
- [27] Rosso, D. 2015 international technology roadmap for semiconductors (itrs). [www.semiconductors.org](http://www.semiconductors.org) 3 (2017). → pages 1
- [28] Ornes, S. News feature: Beyond graphene. *Proceedings of the National Academy of Sciences* **112**, 13128–13130 (2015). → pages 1

- [29] Schwierz, F., Pezoldt, J. & Granzner, R. Two-dimensional materials and their prospects in transistor electronics. *Nanoscale* **7**, 8261–8283 (2015). → pages 1
- [30] Novoselov, K. S., Geim, A. K., Morozov, S. V., Jiang, D., Zhang, Y., Dubonos, S. V., Grigorieva, I. V. & Firsov, A. A. Electric field effect in atomically thin carbon films. *science* **306**, 666–669 (2004). → pages 1, 14
- [31] Zhu, W., Yogeesh, M. N., Yang, S., Aldave, S. H., Kim, J.-S., Sonde, S., Tao, L., Lu, N. & Akinwande, D. Flexible black phosphorus ambipolar transistors, circuits and an demodulator. *Nano letters* **15**, 1883–1890 (2015). → pages 2
- [32] Zhu, W., Park, S., Yogeesh, M. N., McNicholas, K. M., Bank, S. R. & Akinwande, D. Black phosphorus flexible thin film transistors at gighertz frequencies. *Nano letters* **16**, 2301–2306 (2016). → pages 2
- [33] Kang, J., Jariwala, D., Ryder, C. R., Wells, S. A., Choi, Y., Hwang, E., Cho, J. H., Marks, T. J. & Hersam, M. C. Probing out-of-plane charge transport in black phosphorus with graphene-contacted vertical field-effect transistors. *Nano letters* **16**, 2580–2585 (2016). → pages 2
- [34] Jeon, P. J., Lee, Y. T., Lim, J. Y., Kim, J. S., Hwang, D. K. & Im, S. Black phosphorus–zinc oxide nanomaterial heterojunction for p–n diode and junction field-effect transistor. *Nano letters* **16**, 1293–1298 (2016). → pages 2
- [35] Youngblood, N., Chen, C., Koester, S. J. & Li, M. Waveguide-integrated black phosphorus photodetector with high responsivity and low dark current. *Nature Photonics*; doi:10.1038/nphoton.2015.23 (2015). → pages 2, 4
- [36] Chen, C., Youngblood, N., Peng, R., Yoo, D., Mohr, D. A., Johnson, T. W., Oh, S.-H. & Li, M. Three-dimensional integration of black phosphorus photodetector with silicon photonics and nanoplasmonics. *Nano Letters* (2017). → pages 2
- [37] Lin, C., Grassi, R., Low, T. & Helmy, A. S. Multilayer black phosphorus as a versatile mid-infrared electro-optic material. *Nano letters* **16**, 1683–1689 (2016). → pages 2
- [38] Zhao, R., Li, J., Zhang, B., Li, X., Su, X., Wang, Y., Lou, F., Zhang, H. & He, J. Triwavelength synchronously mode-locked fiber laser based on

few-layered black phosphorus. *Applied Physics Express* **9**, 092701 (2016).  
→ pages 2

- [39] Yang, Y., Gao, J., Zhang, Z., Xiao, S., Xie, H.-H., Sun, Z.-B., Wang, J.-H., Zhou, C.-H., Wang, Y.-W., Guo, X.-Y. *et al.* Photocathodes: Black phosphorus based photocathodes in wideband bifacial dye-sensitized solar cells (adv. mater. 40/2016). *Advanced Materials* **28**, 8787–8787 (2016). → pages 2
- [40] Wang, T., Hu, S., Chamlagain, B., Hong, T., Zhou, Z., Weiss, S. M. & Xu, Y.-Q. Visualizing light scattering in silicon waveguides with black phosphorus photodetectors. *Advanced Materials* **28**, 7162–7166 (2016). → pages 2
- [41] Ling, X., Wang, H., Huang, S., Xia, F. & Dresselhaus, M. S. The renaissance of black phosphorus. *Proceedings of the National Academy of Sciences* **112**, 4523–4530 (2015). → pages 2
- [42] Bridgman, P. Two new modifications of phosphorus. *Journal of the American Chemical Society* **36**, 1344–1363 (1914). → pages 2
- [43] Splendiani, A., Sun, L., Zhang, Y., Li, T., Kim, J., Chim, C.-Y., Galli, G. & Wang, F. Emerging photoluminescence in monolayer mos<sub>2</sub>. *Nano letters* **10**, 1271–1275 (2010). → pages 4
- [44] Mak, K. F., Lee, C., Hone, J., Shan, J. & Heinz, T. F. Atomically thin mos<sub>2</sub>: a new direct-gap semiconductor. *Physical Review Letters* **105**, 136805 (2010). → pages 4
- [45] Zhao, W., Ghorannevis, Z., Chu, L., Toh, M., Kloc, C., Tan, P.-H. & Eda, G. Evolution of electronic structure in atomically thin sheets of ws<sub>2</sub> and wse<sub>2</sub>. *ACS nano* **7**, 791–797 (2012). → pages 4
- [46] Castellanos-Gomez, A., Vicarelli, L., Prada, E., Island, J. O., Narasimha-Acharya, K., Blanter, S. I., Groenendijk, D. J., Buscema, M., Steele, G. A., Alvarez, J. *et al.* Isolation and characterization of few-layer black phosphorus. *2D Materials* **1**, 025001 (2014). → pages 4, 24, 39, 50, 82, 91
- [47] Liang, L., Wang, J., Lin, W., Sumpter, B. G., Meunier, V. & Pan, M. Electronic bandgap and edge reconstruction in phosphorene materials. *Nano letters* **14**, 6400–6406 (2014). → pages 4

- [48] Takao, Y., Asahina, H. & Morita, A. Electronic structure of black phosphorus in tight binding approach. *Journal of the Physical Society of Japan* **50**, 3362–3369 (1981). → pages 4
- [49] Tran, V., Soklaski, R., Liang, Y. & Yang, L. Layer-controlled band gap and anisotropic excitons in few-layer black phosphorus. *Physical Review B* **89**, 235319 (2014). → pages 4, 15, 18, 68, 82
- [50] Qin, G., Yan, Q.-B., Qin, Z., Yue, S.-Y., Cui, H.-J., Zheng, Q.-R. & Su, G. Hinge-like structure induced unusual properties of black phosphorus and new strategies to improve the thermoelectric performance. *Scientific reports* **4**, 6496 (2014). → pages 4
- [51] Lv, H., Lu, W., Shao, D. & Sun, Y. Large thermoelectric power factors in black phosphorus and phosphorene. *arXiv preprint arXiv:1404.5171* (2014). → pages 4
- [52] Lu, S., Miao, L., Guo, Z., Qi, X., Zhao, C., Zhang, H., Wen, S., Tang, D. & Fan, D. Broadband nonlinear optical response in multi-layer black phosphorus: an emerging infrared and mid-infrared optical material. *Optics express* **23**, 11183–11194 (2015). → pages 4
- [53] Hong, T., Chamlagain, B., Lin, W., Chuang, H.-J., Pan, M., Zhou, Z. & Xu, Y.-Q. Polarized photocurrent response in black phosphorus field-effect transistors. *Nanoscale* **6**, 8978–8983 (2014). → pages 4
- [54] Koenig, S. P., Doganov, R. A., Schmidt, H., Neto, A. C. & Oezylmaz, B. Electric field effect in ultrathin black phosphorus. *Applied Physics Letters* **104**, 103106 (2014). → pages 4
- [55] Das, S., Demarteau, M. & Roelofs, A. Ambipolar phosphorene field effect transistor. *ACS nano* **8**, 11730–11738 (2014). → pages 4
- [56] Du, Y., Liu, H., Deng, Y. & Ye, P. D. Device perspective for black phosphorus field-effect transistors: Contact resistance, ambipolar behavior, and scaling. *ACS nano* **8**, 10035–10042 (2014). → pages 4
- [57] Kim, J. S., Jeon, P. J., Lee, J., Choi, K., Lee, H. S., Cho, Y., Lee, Y. T., Hwang, D. K. & Im, S. Dual gate black phosphorus field effect transistors on glass for nor logic and organic light emitting diode switching. *Nano letters* **15**, 5778–5783 (2015). → pages 4

- [58] Yin, D. & Yoon, Y. Design strategy of two-dimensional material field-effect transistors: Engineering the number of layers in phosphorene fets. *Journal of Applied Physics* **119**, 214312 (2016). → pages 4
- [59] Xia, F., Wang, H. & Jia, Y. Rediscovering black phosphorus as an anisotropic layered material for optoelectronics and electronics. *Nature communications* **5** (2014). → pages 4, 9, 13, 24, 91
- [60] Chen, H., Liu, H., Zhang, Z., Hu, K. & Fang, X. Nanostructured photodetectors: From ultraviolet to terahertz. *Advanced Materials* **28**, 403–433 (2016). → pages 4
- [61] Doganov, R. A., O'Farrell, E. C., Koenig, S. P., Yeo, Y., Ziletti, A., Carvalho, A., Campbell, D. K., Coker, D. F., Watanabe, K., Taniguchi, T. *et al.* Transport properties of pristine few-layer black phosphorus by van der waals passivation in an inert atmosphere. *Nature communications* **6** (2015). → pages 9
- [62] Luo, Z., Maassen, J., Deng, Y., Du, Y., Garrelts, R. P., Lundstrom, M. S., Peide, D. Y. & Xu, X. Anisotropic in-plane thermal conductivity observed in few-layer black phosphorus. *Nature communications* **6** (2015). → pages 11, 24, 91, 99
- [63] Favron, A., Gaufrès, E., Fossard, F., Phaneuf-LHeureux, A.-L., Tang, N. Y., Lévesque, P. L., Loiseau, A., Leonelli, R., Francoeur, S. & Martel, R. Photooxidation and quantum confinement effects in exfoliated black phosphorus. *Nature materials* **14**, 826–832 (2015). → pages 13, 15, 82, 125
- [64] Luo, W., Zemlyanov, D. Y., Milligan, C. A., Du, Y., Yang, L., Wu, Y. & Peide, D. Y. Surface chemistry of black phosphorus under a controlled oxidative environment. *Nanotechnology* **27**, 434002 (2016). → pages 13
- [65] Wang, Y., Yang, B., Wan, B., Xi, X., Zeng, Z., Liu, E., Wu, G., Liu, Z. & Wang, W. Degradation of black phosphorus: a real-time <sup>31</sup>p nmr study. *2D Materials* **3**, 035025 (2016). → pages 13
- [66] Li, Q., Chen, J., Feng, Z., Feng, L., Yao, D. & Wang, S. The role of air adsorption in inverted ultrathin black phosphorus field-effect transistors. *Nanoscale Research Letters* **11**, 521 (2016). → pages 13
- [67] Ryder, C. R., Wood, J. D., Wells, S. A., Yang, Y., Jariwala, D., Marks, T. J., Schatz, G. C. & Hersam, M. C. Covalent functionalization and passivation



of exfoliated black phosphorus via aryl diazonium chemistry. *Nature chemistry* (2016). → pages 13

- [68] Wood, J. D., Wells, S. A., Jariwala, D., Chen, K.-S., Cho, E., Sangwan, V. K., Liu, X., Lauhon, L. J., Marks, T. J. & Hersam, M. C. Effective passivation of exfoliated black phosphorus transistors against ambient degradation. *Nano letters* **14**, 6964–6970 (2014). → pages 13
- [69] Brent, J. R., Savjani, N., Lewis, E. A., Haigh, S. J., Lewis, D. J. & O'Brien, P. Production of few-layer phosphorene by liquid exfoliation of black phosphorus. *Chemical Communications* **50**, 13338–13341 (2014). → pages 13, 15, 16
- [70] Hanlon, D., Backes, C., Doherty, E., Cucinotta, C. S., Berner, N. C., Boland, C., Lee, K., Harvey, A., Lynch, P., Gholamvand, Z. *et al.* Liquid exfoliation of solvent-stabilized few-layer black phosphorus for applications beyond electronics. *Nature communications* **6** (2015). → pages 13, 16
- [71] Seo, S., Lee, H. U., Lee, S. C., Kim, Y., Kim, H., Bang, J., Won, J., Kim, Y., Park, B. & Lee, J. Triangular black phosphorus atomic layers by liquid exfoliation. *Scientific reports* **6** (2016). → pages 13
- [72] Lee, G., Lee, J.-Y., Lee, G.-H. & Kim, J. Tuning the thickness of black phosphorus via ion bombardment-free plasma etching for device performance improvement. *Journal of Materials Chemistry C* (2016). → pages 13
- [73] Pei, J., Gai, X., Yang, J., Wang, X., Yu, Z., Choi, D.-Y., Luther-Davies, B. & Lu, Y. Producing air-stable monolayers of phosphorene and their defect engineering. *Nature communications* **7** (2016). → pages 13
- [74] Kang, J., Wood, J. D., Wells, S. A., Lee, J.-H., Liu, X., Chen, K.-S. & Hersam, M. C. Solvent exfoliation of electronic-grade, two-dimensional black phosphorus. *ACS nano* **9**, 3596–3604 (2015). → pages 15, 16
- [75] Guo, Z., Zhang, H., Lu, S., Wang, Z., Tang, S., Shao, J., Sun, Z., Xie, H., Wang, H., Yu, X.-F. *et al.* From black phosphorus to phosphorene: basic solvent exfoliation, evolution of raman scattering, and applications to ultrafast photonics. *Advanced Functional Materials* **25**, 6996–7002 (2015). → pages 15, 16

- [76] Kang, J., Wells, S. A., Wood, J. D., Lee, J.-H., Liu, X., Ryder, C. R., Zhu, J., Guest, J. R., Husko, C. A. & Hersam, M. C. Stable aqueous dispersions of optically and electronically active phosphorene. *Proceedings of the National Academy of Sciences* 201602215 (2016). → pages 16
- [77] Wang, H., Yang, X., Shao, W., Chen, S., Xie, J., Zhang, X., Wang, J. & Xie, Y. Ultrathin black phosphorus nanosheets for efficient singlet oxygen generation. *Journal of the American Chemical Society* **137**, 11376–11382 (2015). → pages 16
- [78] Kumar, V., Brent, J. R., Shorie, M., Kaur, H., Chadha, G., Thomas, A. G., Lewis, E. A., Rooney, A. P., Nguyen, L., Zhong, X. L. *et al.* Nanostructured aptamer-functionalized black phosphorus sensing platform for label-free detection of myoglobin, a cardiovascular disease biomarker. *ACS Applied Materials & Interfaces* **8**, 22860–22868 (2016). → pages 16
- [79] Brent, J. R., Ganguli, A. K., Kumar, V., Lewis, D. J., McNaughter, P. D., O'Brien, P., Sabherwal, P. & Tedstone, A. A. On the stability of surfactant-stabilised few-layer black phosphorus in aqueous media. *RSC Advances* **6**, 86955–86958 (2016). → pages 16
- [80] Zhao, W., Xue, Z., Wang, J., Jiang, J., Zhao, X. & Mu, T. Large-scale, highly efficient, and green liquid-exfoliation of black phosphorus in ionic liquids. *ACS applied materials & interfaces* **7**, 27608–27612 (2015). → pages 16
- [81] Jia, J., Jang, S. K., Lai, S., Xu, J., Choi, Y. J., Park, J.-H. & Lee, S. Plasma-treated thickness-controlled two-dimensional black phosphorus and its electronic transport properties. *ACS nano* **9**, 8729–8736 (2015). → pages 17
- [82] Bachhuber, F., von Appen, J., Dronskowski, R., Schmidt, P., Nilges, T., Pfitzner, A. & Wehrich, R. The extended stability range of phosphorus allotropes. *Angewandte Chemie International Edition* **53**, 11629–11633 (2014). → pages 19
- [83] Sugai, S., Ueda, T. & Murase, K. Pressure dependence of the lattice vibration in the orthorhombic and rhombohedral structures of black phosphorus. *Journal of the Physical Society of Japan* **50**, 3356–3361 (1981). → pages 20

- [84] Kawamura, H., Shirotni, I. & Tachikawa, K. Anomalous superconductivity in black phosphorus under high pressures. *Solid state communications* **49**, 879–881 (1984). → pages 20
- [85] Rissi, E. N., Soignard, E., McKiernan, K. A., Benmore, C. J. & Yarger, J. L. Pressure-induced crystallization of amorphous red phosphorus. *Solid State Communications* **152**, 390–394 (2012). → pages 20
- [86] Tuschel, D. Why are the raman spectra of crystalline and amorphous solids different? (2017). → pages 22
- [87] Raman, C. V. & Krishnan, K. S. A new type of secondary radiation. *Nature* **121**, 501–502 (1928). → pages 28
- [88] Venkateswarlu, K. Relative intensities of stokes and anti-stokes raman lines in crystals. *Proceedings Mathematical Sciences* **13**, 64–67 (1941). → pages 28
- [89] Bowley, H. J., Gerrard, D. L., Loudon, J. D., Turrell, G., Gardiner, D. J. & Graves, P. R. *Practical raman spectroscopy* (Springer Science & Business Media, 2012). → pages 34
- [90] Lu, W., Ma, X., Fei, Z., Zhou, J., Zhang, Z., Jin, C. & Zhang, Z. Probing the anisotropic behaviors of black phosphorus by transmission electron microscopy, angular-dependent raman spectra, and electronic transport measurements. *Applied Physics Letters* **107**, 021906 (2015). → pages 35
- [91] Tuschel, D. Raman crystallography in theory and in practice. *Spectroscopy* **27**, 22–27 (2012). → pages 37, 121
- [92] Yoo, W. S., Harima, H. & Yoshimoto, M. Polarized raman signals from si wafers: Dependence of in-plane incident orientation of probing light. *ECS Journal of Solid State Science and Technology* **4**, P356–P363 (2015). → pages 37, 121
- [93] Li, X.-L., Han, W.-P., Wu, J.-B., Qiao, X.-F., Zhang, J. & Tan, P.-H. Layer-number dependent optical properties of 2d materials and their application for thickness determination. *Advanced Functional Materials* (2017). → pages 38
- [94] Li, X.-L., Qiao, X.-F., Han, W.-P., Lu, Y., Tan, Q.-H., Liu, X.-L. & Tan, P.-H. Layer number identification of intrinsic and defective multilayered graphenes up to 100 layers by the raman mode intensity from substrates. *Nanoscale* **7**, 8135–8141 (2015). → pages 38

- [95] Li, X.-L., Qiao, X.-F., Han, W.-P., Zhang, X., Tan, Q.-H., Chen, T. & Tan, P.-H. Determining layer number of two-dimensional flakes of transition-metal dichalcogenides by the raman intensity from substrates. *Nanotechnology* **27**, 145704 (2016). → pages 38
- [96] Lu, X., Utama, M. I. B., Zhang, J., Zhao, Y. & Xiong, Q. Layer-by-layer thinning of mos 2 by thermal annealing. *Nanoscale* **5**, 8904–8908 (2013). → pages 39
- [97] Su, L. & Zhang, Y. Temperature coefficients of phonon frequencies and thermal conductivity in thin black phosphorus layers. *Applied Physics Letters* **107**, 071905 (2015). → pages 41, 53
- [98] Luo, W., Song, Q., Zhou, G., Tuschel, D. & Xia, G. Study of black phosphorus using angle-resolved polarized raman spectroscopy with 442 nm excitation. *arXiv preprint arXiv:1610.03382* (2016). → pages 48, 66
- [99] Vierimaa, V., Krasheninnikov, A. V. & Komsa, H.-P. Phosphorene under electron beam: from monolayer to one-dimensional chains. *Nanoscale* **8**, 7949–7957 (2016). → pages 54
- [100] Li, H., Wu, J., Huang, X., Lu, G., Yang, J., Lu, X., Xiong, Q. & Zhang, H. Rapid and reliable thickness identification of two-dimensional nanosheets using optical microscopy. *ACS nano* **7**, 10344–10353 (2013). → pages 82
- [101] Li, H., Lu, G., Yin, Z., He, Q., Li, H., Zhang, Q. & Zhang, H. Optical identification of single-and few-layer mos2 sheets. *Small* **8**, 682–686 (2012). → pages 82
- [102] Schneider, C. A., Rasband, W. S. & Eliceiri, K. W. Nih image to imagej: 25 years of image analysis. *Nature methods* **9**, 671 (2012). → pages 82
- [103] Azuhata, T., Sota, T., Suzuki, K. & Nakamura, S. Polarized raman spectra in gan. *Journal of Physics: Condensed Matter* **7**, L129 (1995). → pages 91
- [104] Duesberg, G., Loa, I., Burghard, M., Syassen, K. & Roth, S. Polarized raman spectroscopy on isolated single-wall carbon nanotubes. *Physical review letters* **85**, 5436 (2000). → pages 91
- [105] Huang, M., Yan, H., Chen, C., Song, D., Heinz, T. F. & Hone, J. Phonon softening and crystallographic orientation of strained graphene studied by raman spectroscopy. *Proceedings of the National Academy of Sciences* **106**, 7304–7308 (2009). → pages 91

- [106] Ribeiro-Soares, J., Almeida, R., Cancado, L., Dresselhaus, M. & Jorio, A. Group theory for structural analysis and lattice vibrations in phosphorene systems. *Physical Review B* **91**, 205421 (2015). → pages 93